Příloha I:

KUBÍKOVÁ, T., KOCHOVÁ, P., BRÁZDIL, J., ŠPATENKA, J., BURKERT, J., KRÁLÍČKOVÁ, M., TONAR, Z. The composition and biomechanical properties of human cryopreserved aortas, pulmonary trunks, and aortic and pulmonary cusps. Ann Anat. 2017; 212:(17-26). DOI: 10.1016/j.aanat.2017.03.004. IF=1.308.

Contents lists available at ScienceDirect

Annals of Anatomy

RESEARCH ARTICLE

The composition and biomechanical properties of human cryopreserved aortas, pulmonary trunks, and aortic and pulmonary cusps

Tereza Kubíková [a,*], Petra Kochová [b], Jan Brázdil [c], Jaroslav Špatenka [c,d], Jan Burkert [c,d], Milena Králíčková [a], Zbyněk Tonar [a]

[a] Department of Histology and Embryology and Biomedical Centre, Faculty of Medicine in Pilsen, Charles University, Pilsen, Czech Republic
[b] European Centre of Excellence NTIS, Faculty of Applied Sciences, University of West Bohemia in Pilsen, Pilsen, Czech Republic
[c] Department of Transplantation and Tissue Banking, University Hospital Motol, Prague, Czech Republic
[d] Department of Cardiovascular Surgery, 2nd Faculty of Medicine, Charles University, Prague, Czech Republic

ARTICLE INFO

ABSTRACT

Human cryopreserved allografts of pulmonary and aortic heart valves, aortas and pulmonary trunks are used for valve replacement. However, it is unknown how the composition of these allografts relate to their mechanical properties. Our aims were to correlate the histological compositions and passive mechanical properties of aortic and pulmonary valves and to observe the microcracks of aortas and pulmonary trunks. The following parameters were quantified: ultimate stress; ultimate strain; Young's modulus of elasticity; valve cusp wall thickness; pulmonary and aortic intima-media thickness; area fraction of elastin, collagen and calcification; and length density of elastic fibres. The propagation of experimentally induced microcracks avoided elastic fibres. Ultimate strain was negatively correlated with the area fraction of calcification ($r = -0.4$) in aortas. Ultimate stress ($r = 0.27$) and Young's modulus in small deformation ($r = 0.29$) and in large deformation ($r = 0.32$) correlated with wall thickness in valve cusps. Young's modulus ($r = 0.34$) and ultimate strain ($r = 0.31$) correlated with intima-media thickness. Ultimate strain correlated with the area fraction of elastin ($r = -0.40$) and collagen in the arteries ($r = 0.31$). As conventional histology does not fully explain the mechanical properties of cryopreserved grafts, both morphological and biomechanical tests should be used complementarily when characterizing the ageing of the grafts.

© 2017 Elsevier GmbH. All rights reserved.

1. Introduction

Human cryopreserved allografts of pulmonary and aortic heart valves, as well as the roots of these major elastic arteries, are routinely used for aortic and pulmonary root and valve replacement in a selected group of patients. This operation is needed mostly because of valvular aortic stenosis (Huygens et al., 2016), but the allograft heart valves are used for other aortic and pulmonary valve pathologies when valve surgical repair is not feasible. Together with surgical techniques, the biomechanical sufficiency and preservation of the histological structures of the grafts are con-

sidered necessary for proper outcomes of reconstructive surgery (Arabkhani et al., 2015).

1.1. Histological structure and aortic and pulmonary valve mechanics

Aortic and pulmonary valves prevent the reversal of blood flow to the cardiac ventricles in diastole. Valve function normally relies on 3 cusps located on the supravalvular bridge and within the geometry of the pulmonary trunk or ascending aorta. The cusps have semilunar shapes. The valves are primarily composed of endothelium, connective tissue cells (fibroblasts and fibrocytes) and extracellular matrix components of connective tissue. The main constituents of the connective tissue are collagen fibrils, elastic fibres and proteoglycans (Hopkins, 2005).

Valve cusps are normally thinner than 1 mm in humans (Hinton and Yutzey, 2011). They are stratified into three layers as follows:

* Corresponding author at: Department of Histology and Embryology, Faculty of Medicine in Pilsen, Charles University, Karlovarská 48, 301 66 Pilsen, Czech Republic.
E-mail address: tereza.kubikova@lfp.cuni.cz (T. Kubíková).

the endocardial endothelial layer, the subendothelial layer, and the myoelastic layer. The myoelastic layer is stratified into a fibrous layer and a spongiosa layer. The fibrous layer is formed by multidirectional, parallel-ordered, dense connective tissue, whereas the spongiosa is made of loose connective tissue. Collagen is the major extracellular matrix (ECM) component of the valves, forming approximately 50% of the total valve by dry weight; elastin comprises 13% of the valve ECM (Bashey et al., 1967). The characteristic distribution of the elastic fibre system is not sex dependent (Otto et al., 2006).

The heart valve cusps are passive elements that open and close rapidly in response to blood flow. Collagen fibres are crimped when the tissue is relaxed and flattened when the tissue is under stress due to the pressurization of the valve. Collagen and elastin are curved fibres that can straighten in response to small amounts of force, allowing great extension of the tissue under low stress (Weinberg et al., 2010). Buchanan's study suggests that the single layers of aortic valves are bonded by transverse collagen fibres and work as one unit (Buchanan and Sacks, 2014). The microstructure and mechanics of the aortic and pulmonary valves were observed by Stradins (2004), but similar results for cryopreserved aortic and pulmonary valves do not exist.

1.2. Histological structure of the ascending aorta and pulmonary trunk

Elastic arteries, such as the ascending aorta and pulmonary trunk, receive blood flow directly from the heart ventricles in systole and are consequently the most compliant type of arteries.

Elastic arteries consist of three concentric layers as follows:

- The tunica intima, which is composed of the vascular endothelium and a subendothelial layer.
- The tunica media, which is the thickest layer and contains concentrically elastic fenestrated membranes and smooth muscle cells.
- The tunica adventitia, which is the most abluminal layer of the elastic arteries. It is composed of elastic and collagenous fibres that are interspersed with connective tissue cells, blood vessels (the vasa vasorum) and nerve fibres (the nervi vasorum).

These three wall layers must to be preserved during allograft valve harvesting, processing and cryopreservation.

Previous studies have shown that the thickness of the pulmonary trunk is 1.5 ± 0.3 mm and that the thickness of the ascending aorta is 2.1 ± 0.4 mm (Azadani et al., 2012).

The cryopreserved allograft heart valve expiration limit has been arbitrarily fixed to 5 years in most allograft heart banks around the world. However, cryopreservation may lead to changes in these allografts. We can use histological and mechanical methods to evaluate the allografts. It is unknown how the histological compositions are related to the mechanical properties of cryopreserved human aortic and pulmonary valves.

1.3. Study aims

The aims of the study are as follows.

- to correlate the histological and mechanical properties of the elastic arteries;
- to correlate the histological and mechanical properties of the cusps; and
- to determine the role of elastin in experimental ruptures.

The null hypotheses tested in the study were formulated as follows:

$H_0(A)$. There is no correlation between the histological and mechanical properties of the aortas and pulmonary trunks; there is no correlation between the histological and mechanical properties of the aortic and pulmonary cusps.

$H_0(B)$. Experimentally induced ruptures propagate randomly across the walls of the ascending aortas or pulmonary trunks.

2. Materials and methods

2.1. Specimens

Samples for our study were obtained from the Heart Valve Bank of the Department of Transplantation and Tissue Banking, University Hospital Motol, Czech Republic. Czech cadaveric, heart beating, multiorgan donor for heart valve allograft processing were harvested from the pool of Czech donors when it was not possible (for any reason) to use the donor heart for transplantation as an organ. The allograft heart valves were processed (dissected and decontaminated by an antibiotic cocktail), programme-cooled and cryopreserved at $-196\,^{\circ}$C according to the established protocol (Špatenka et al., 1997) in compliance with the Czech legislation (Czech Law on Quality and Safety of Human Tissue and Cells for Application in Humans 296/2008 of Czech Legal Code). Twelve aortic valve allografts and eighteen pulmonary valve allografts were used for this study. From each aortic and pulmonary allograft, we cut a ring of the aorta or pulmonary trunk and prepared (Fig. 1A) two cusp specimens from each pulmonary allograft and two cusp specimens—the right and left coronary cusps—from each aortic allograft.

2.2. Mechanical loading

Tensile tests of the specimens were measured at room temperature using a Zwick/Roell Z50 traction machine equipped with a 1-kN load cell to obtain the mechanical parameters, namely Young's modulus of elasticity, ultimate stress and ultimate strain. The thicknesses of the individual specimens were measured using digital calipers. The width was determined by cutting using two parallel razors as follows: the valve cusps were 5-mm wide, and the rings of aortas and pulmonary trunks were 10-mm wide. The uniaxial ring test was used to measure the mechanical properties of the elastic arteries. The Young's moduli of elasticity were determined in the linear regions of the stress–strain curve, namely in the small deformation region ($E0$) and in the large deformation region ($E1$), using linear regression. The strains were approximately 0–20% and 40–60% for elastic arteries (0–10% and 8–60% for cusps) for the two regions, respectively, depending on the shape of the curve. The ultimate stresses and ultimate strains were determined at the start of the rupture. The stress was defined as the force divided by the initial area. The strain was defined as the actual circumference change divided by its initial circumference for elastic arteries and as the elongation of the specimen divided by its initial length for cusps. Our own software, Elfpy (Prosecká et al., 2011), was used for the evaluation.

2.3. Histological processing and quantification

The tissue samples were fixed in 4% buffered formalin, dehydrated and embedded in paraffin blocks. At least ten 5-μm-thick histological sections were obtained from each paraffin-embedded tissue block. Two sections were stained with haematoxylin–eosin and two sections were stained with Verhoeff's haematoxylin and green trichrome (Kočová, 1970) to visualise the connective tissue (Fig. 1B). Two sections were stained with orcein to visualise the elastic fibres (Fig. 1C–D), two sections were stained with picrosirius
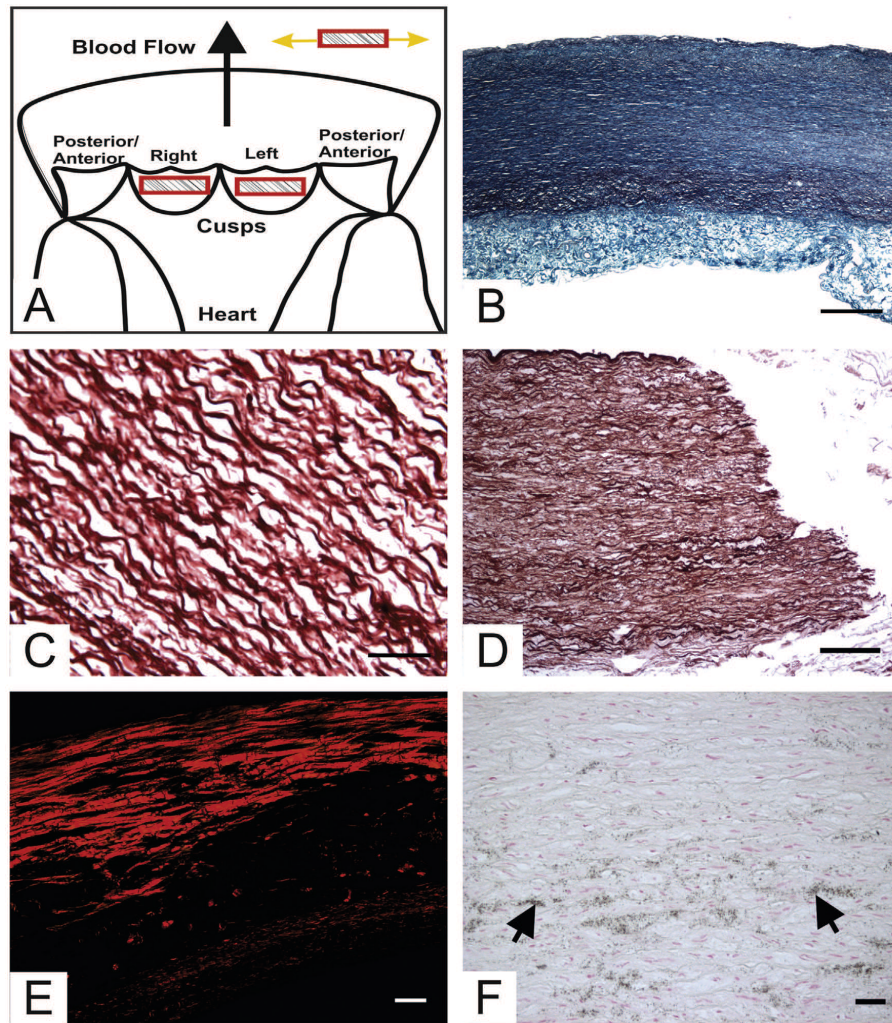
Fig. 1. Sampling and histological staining methods for the evaluation of histological compositions. (A) Scheme for the preparation of specimens from the allografts. Each heart valve allograft was cut longitudinally to create two cusp specimens, right semilunar (right-facing) and left semilunar (left-facing) cusps (red rectangles). Anterior or posterior semilunar (non-facing) cusps were not measured. The direction of the mechanical loading of these specimens is depicted (yellow arrows). (B) Wall of the aorta, Verhoeff's haematoxylin and green trichrome stained the collagen green and elastin black. Scale bar, 500 μm. (C) Visualization of the red–brown elastic fibres with orcein in the media. Scale bar, 100 μm. (D) A rupture of the aorta after mechanical loading stained with orcein. Scale bar, 100 μm. (E) Visualization of red type I collagen in an aortic valve stained with picrosirius red and viewed with polarized light. Scale bar, 50 μm. (F) Calcification (black arrows) in the aortic wall was stained using the von Kossa method. Scale bar, 50 μm. (For interpretation of the references to colour in this figure legend, the reader is referred to the web version of this article.)

red to visualise the type I collagen using circularly polarized light (Fig. 1E), and another two sections were stained using the von Kossa method (Merck Millipore, Darmstadt, Germany) to visualise calcification (Fig. 1F). In total, 780 slides and 2040 micrographs were examined histologically.

The evaluated histological parameters, numbers of micrographs and objectives used are shown in Table 1. The area fraction of each major tissue component was evaluated using a stereological grid point (Mouton, 2002; Kochová et al., 2012; Tonar et al., 2015).

Ten aortas and 10 pulmonary trunks after mechanical loading were used for study of microcracks. For the histological analysis of microcracks induced by the experimental mechanical analyser, a previously established method was used (Tonar et al., 2009). Briefly, to study the relationship of microcracks and elastic fibres, we compared the estimated value of the intersection intensity of elastic fibres along the crack P_L' with its theoretical value P_L, calculated under the assumption of the independence of the cracks on the elastic fibres. The intersection density of the elastic fibres in the microcracks was defined as follows:

$$p_L = \frac{p}{l} \tag{1}$$

where p is the number of the intersections along a crack of the length l. The intensity of the intersections of the rupture profiles

Table 1
Sampling of micrographs for measuring the histological parameters.

| Tissue	Evaluated parameter	Staining	Number of microphotographs per specimen	Used objective in microscope
Artery	Whole wall thickness	Verhoeff's haematoxylin and green trichrome	4	4×
	Thickness of tunica intima and media			
	Area fraction of elastin within intima-media—A_A(elastin, media)	orcein	8	40×
	Length density of elastic fibres in media—L_A(elastin, media)			
	Area fraction of collagen in wall—A_A(collagen, wall)	picrosirius red	8	20×
Cusp	Whole wall thickness	Verhoeff's haematoxylin and green trichrome	4	4×
	Area fraction of elastin within wall—A_A(elastin, wall)	orcein	8	40×
	Area fraction of collagen within wall—A_A(collagen, wall)	picrosirius red	8	20×
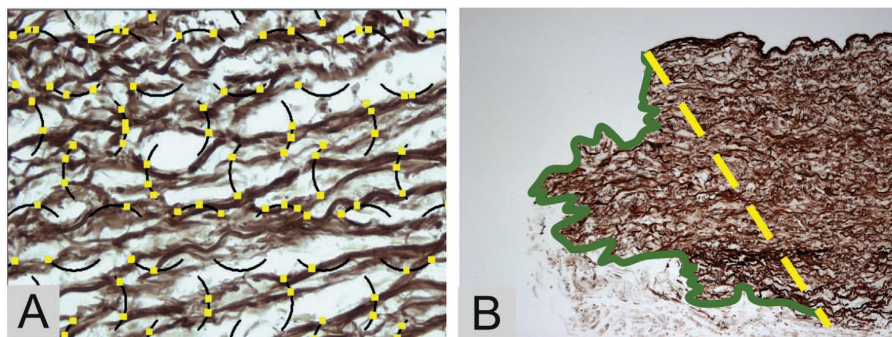
Fig. 2. Study of the relationship between microcracks and elastic fibres. (A) Circular arcs contacting the elastic fibres were used to assess the two-dimensional length density of the elastic fibres L_A. (B) The edge of the rupture is highlighted in green. The maximal projection length l is drawn as a yellow line. Red–brown elastic fibres were stained with orcein. (For interpretation of the references to colour in this figure legend, the reader is referred to the web version of this article.)

with the elastic fibres P'_L was estimated by dividing the real number of these intersections (p') counted in the sections by the maximal projection length of the profiles (l). We used the maximal projection length of the crack as a lower bound of the real length. We estimated the maximal projection length of the crack (l) as the shortest distance between the beginning and end of the rupture profile.

The theoretical intersection density, under the assumption of the independence of the cracks and elastic fibres, was calculated as the intersection intensity of a randomly oriented line (i.e., the profile of a rupture) with the elastic fibres (Stoyan et al., 1995) as follows:

$$P_L = \frac{2}{\pi} \cdot L_A \qquad (2)$$

where L_A was the 2D length density of elastic fibres in the media. For each elastic artery, we assessed the length density L_A of the elastic fibres as follows:

$$L_A = \frac{L}{A} \qquad (3)$$

where L_A is the length density, L is the length of elastic fibres and A is the area of the reference space media. L was estimated by counting the intersections between the circular arcs positioned randomly on the micrographs and the elastic fibres (Fig. 2). To estimate the L and A parameters, we used the LineSystem module in Ellipse software (ViDiTo, Košice, Slovakia) (Mouton, 2002; Tonar et al., 2009, 2015).

2.4. Statistics

The data were processed using Statistica Base 10 (StatSoft, Inc., Tulsa, OK, USA). The data had normal distribution. The t-test was used when comparing samples. Pearson's correlation was used for the correlation of samples.

3. Results

3.1. Aortic root and pulmonary trunk

Stress–strain curves showed similar shapes for all the tested tissue samples. Stress–strain curves of the aortic root and pulmonary trunk samples had a typical shape for biological materials (Fig. 3A). The curves were nonlinear, showing a small deformation region, stiffening, and a linear region of large deformations (Fig. 3C). The small deformation region was characterised by a low gradient, that is, a low Young's modulus of elasticity. In the linear region of the large deformation, the modulus of elasticity was considerably higher, representing the stiffening of the tissues with increasing strain.

The theoretical intersection density of elastic fibres in the rupture of elastic arteries was greater than the real intersection density ($p < 0.001$) (Fig. 3D).

The $E1$ deformation region showed a weakly positive correlation with intima-media thickness (IMT) in the arteries (0.34). The ulti-
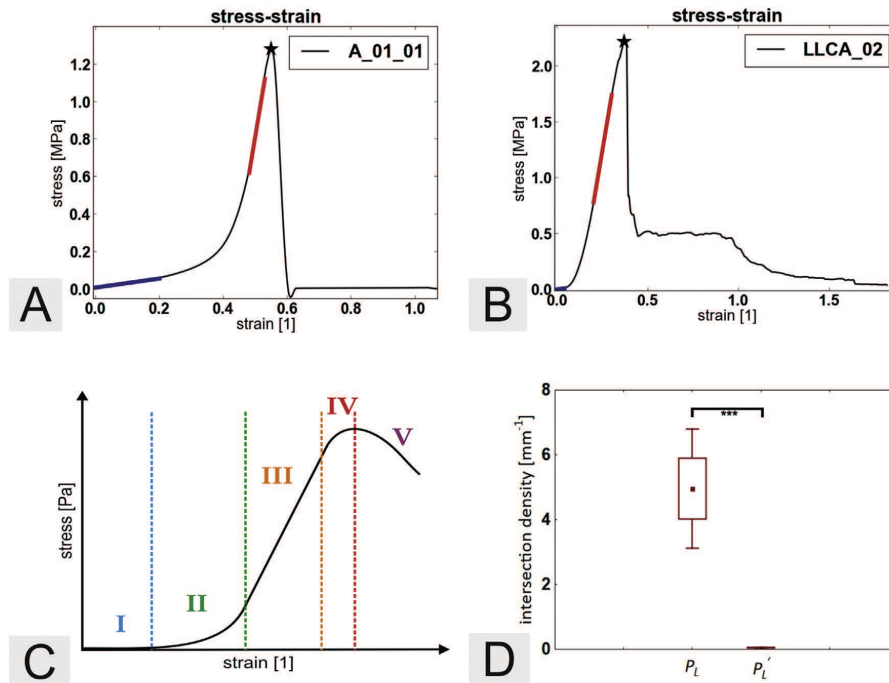
Fig. 3. Mechanical measurement and histological analysis of the aortic and pulmonary valves. (A) Example of a nonlinear stress–strain curve of the aorta; note the small deformation region (blue line) with a low stiffness and the linear region of large deformations (red line) with a higher stiffness. The star marks the beginning of the rupture of the tissue characterized by ultimate stress and strain. (B) Example of a nonlinear stress–strain curve of the heart cusp; note the small deformation region (blue line) with a low stiffness and the linear region of large deformations (red line) with a higher stiffness. The star marks the beginning of the rupture of the tissue characterized by ultimate stress and strain. (C) Nonlinear stress–strain curve characteristics of soft biological materials: I—the region of small deformations (toe curve region) with a low stiffness; II—the heel region of the curve with progressive stiffening of the tissue; III—the linear region of large deformations with a high stiffness; IV—the region before tissue rupture with initialisation of the rupture at the end of this region; and V—the region of the rupture of individual components of the tissue. (D) Theoretical intersection density (P_L) of elastic fibres in the rupture of elastic arteries was greater than the real intersection density (P_L') (***$p < 0.001$). The box plot shows the average, minimal, and maximal values and the standard deviation for each group. (For interpretation of the references to colour in this figure legend, the reader is referred to the web version of this article.)

mate strain had a moderately positive correlation with *IMT* (0.31), a moderately negative correlation with the area fraction of elastin in the intima-media (−0.48) and a moderately positive correlation with the area fraction of collagen in the wall (0.31). Ultimate strain was moderately negatively correlated with the area fraction of calcification (−0.4) in the aortas.

The whole wall thickness of the aortas was greater than the whole wall thickness of the pulmonary trunks ($p < 0.001$) (Fig. 4A). *IMT* of the aortas was greater than *IMT* of the pulmonary trunks ($p < 0.001$). There were no differences between the area fractions of elastin in the aortas and pulmonary trunks (Fig. 4B). There were no differences between the area fractions of collagen in the aortas and pulmonary trunks (Fig. 4C).

The mean values and standard deviations for all the biomechanical and histological parameters are listed in Table 2. The complete primary data from the mechanical analyses, including the Young's modulus of elasticity in small and large deformation regions, ultimate strain and ultimate stress and histological analyses of wall thickness, intima-media thickness, and area fraction of elastin, area fraction of collagen and area fraction of calcification in aortic roots and pulmonary trunks, are provided in Supplement 1 (in Supplementary data).

There were no obvious differences in the distribution of calcification in the areas of ruptures compared with the other parts of the samples (Fig. 5).

3.2. Aortic and pulmonary heart valve cusps

Stress–strain curves showed similar shapes in all the tested tissue samples. Stress–strain curves of the heart valve cusps had a typical shape for biological materials (Fig. 3B). The curves were nonlinear, showing a small deformation region, stiffening, and a linear region of large deformations (Fig. 3C). The small deformation region was characterised by a low gradient, that is, a low Young's modulus of elasticity. In the linear region of large deformation, the modulus of elasticity was considerably higher, representing the stiffening of the tissues with increasing strain.

The wall thickness had weak correlation with *E0* (0.29), a moderate correlation with *E1* (0.32) and a weak correlation with the ultimate stress (0.27). The wall thickness of the aortic cusps was greater than the wall thickness of the pulmonary valve cusps ($p < 0.001$) (Fig. 6A). There were no differences between the area fraction of elastin in the aortic cusps and pulmonary cusps (Fig. 6B). The area fraction of collagen in the aortic cusps was greater than the area fraction of collagen in the pulmonary cusps ($p < 0.05$) (Fig. 6C).

The mean values and standard deviations for all the biomechanical and histological parameters are listed in Table 3. The complete results of the mechanical analyses, including the Young's modulus of elasticity in the small and large deformation regions, ultimate strain and ultimate stress, as well as the histological analyses of wall thickness and area fraction of elastin and area fraction of col-
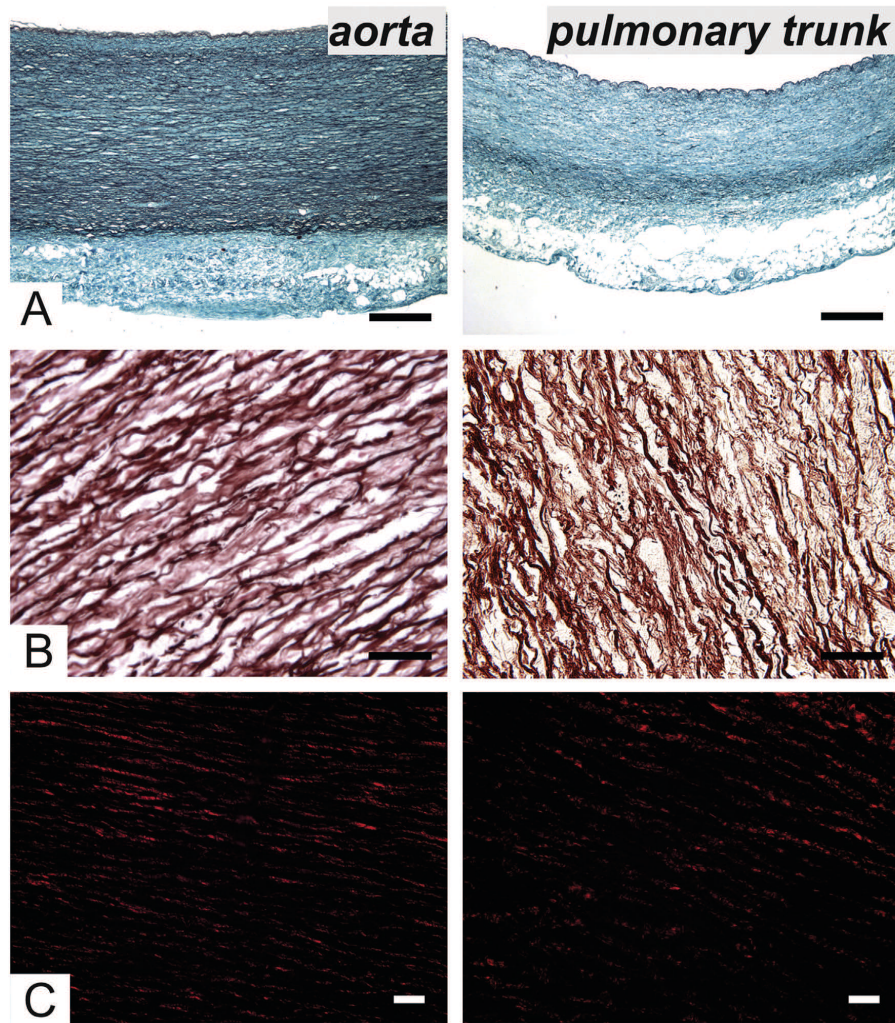
Fig. 4. Comparison of the aortas and pulmonary trunks. (A) The whole wall thickness of the aortas was greater than the whole wall thickness of the pulmonary trunks (p < 0.001). Verhoeff's haematoxylin and green trichrome stained the collagen green and elastin black. Scale bar, 500 μm. (B) There was no difference between the area fraction of elastin in the aortas and pulmonary trunks. Red–brown elastic fibres were stained with orcein in the media. Scale bar, 100 μm. (C) There were no differences between the area fractions of collagen in the aortas and pulmonary trunks. Red type I collagen was stained with picrosirius red and was viewed with polarized light. Scale bar, 50 μm. (For interpretation of the references to colour in this figure legend, the reader is referred to the web version of this article.)

lagen in aortic and pulmonary cusps, are provided in Supplement 2 (in Supplementary data).

4. Discussion

The theoretical intersection density of the elastic fibres in the rupture of elastic arteries was greater than the true intersection density (p < 0.001). The elastic fibres were not a weak component of the elastic arteries.

Stiffness increased with calcification (Pham and Sun, 2014). Our results showed that calcification was negatively correlated with ultimate strain in the aortas. Deformation of the aortic tissue was decreased with calcification. The presence of calcification led to the genesis of local stress and ruptures in these areas (Li et al., 2008; Marra et al., 2006). We did not observe more calcification around ruptures. The allografts are macroscopically inspected by the cardiac surgeon in time of heart valve allograft dissection procedure, before cryopreservation. If lesions with calcification are found, the allograft is not submitted for tissue banking. Therefore, we observed only small areas with calcification (Fig. 1F) in the media of the aortas and pulmonary trunks. Intimal calcification is regularly found in the context of an atherosclerotic alteration of the vessel wall. Medial calcification, also known as Monckeberg's disease, occurs in elderly patients (Doehring et al., 2006).

The results of histological quantification showed that the investigated tissues are composed mostly of elastin and collagen.
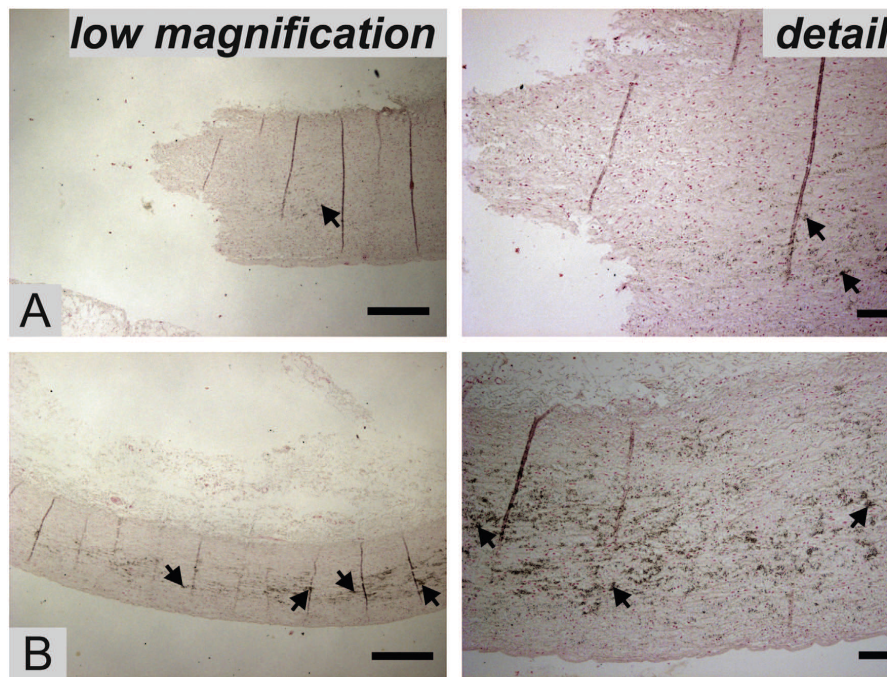
Fig. 5. Calcification in a pulmonary trunk wall. (A) In the areas of rupture, there was not more calcification (black arrows) than in other areas of the sample. (B) Distant area from the rupture. Staining by the von Kossa method. Scale bar, 1 mm (left column) and 50 μm (right column).

The nonlinear behaviour of the heart valve components can be explained by mechanical properties, structural composition and interconnection of collagen and elastin. Collagen has a wave-like organisation in the arteries and valves, thus contributing to tissue mechanical properties only at higher values of the deformation after its alignment in the loading direction. In the initial phase of loading, the material properties of collagen only marginally influence the modulus of elasticity of tissue. The main role in small deformations is played by elastin with a small Young's modulus (0.6 MPa) in ligamentum nuchae, (Vincent, 1990). After stretching, collagen fibres have a high Young's modulus of elasticity (1–2.5 GPa) for collagen in the rat tail tendon, (Meyers et al., 2008) and begin to contribute to the total mechanical response of the tissue. The characteristic distribution of the elastic fibre system is not sex dependent, but it is different in a single layer of cusps (Otto et al., 2006). We evaluated the area fraction of elastin in the whole wall of cusps.

Cryopreserved mitral allograft implantation into the tricuspid was investigated in sheep. The mechanical quality of the grafts was impressive according to the surgeon (Vojáček et al., 2006), which was why we then studied the influence of cryopreservation on the allograft mechanical properties in the porcine model. No morphological assessment was performed, unfortunately (Hlubocký et al., 2011). We obtained data showing that our standard protocol of human allograft heart valve harvesting, processing and cryopreservation seriously destroyed the allograft endothelium (Burkert et al., 2008); the mechanical and histological tissue properties were not studied in these settings, as well.

Many studies have been performed with pig heart valves (Balaoing et al., 2014; Veselý, 1998). Martin and Sun's study indicated that the 1-year-old ovine model and 6- to 9-month-old

Table 2
The mean values and standard deviations of biomechanical and histological parameters in aortas and pulmonary trunks.

Evaluated parameter	Aorta			Pulmonary trunk		
	n	Mean	Standard deviation	n	Mean	Standard deviation
Young's modulus in small deformation (MPa)	25	0.38	0.37	18	0.25	0.27
Young's modulus in large deformation (MPa)	25	18.58	17.20	18	8.25	6.99
Ultimate stress	25	0.60	0.14	18	0.43	0.11
Ultimate strain	25	2.67	2.45	18	1.40	1.53
Wall thickness (μm)	25	2399	247.55	18	1952	321.65
Intima-media thickness (μm)	25	1864	240.64	18	1252	233.18
A_A (elastin, media)	25	0.47	0.08	18	0.5	0.05
A_A (collagen I, wall)	25	0.12	0.06	18	0.11	0.04
A_A (calcification, wall)	25	0.004	0.007	18	0.002	0.005

A_A (elastin, media), the area fraction of elastin within media; A_A (collagen I, wall), the area fraction of type I collagen within wall; A_A (calcification, wall), the area fraction of calcification within wall and n, number of specimens.
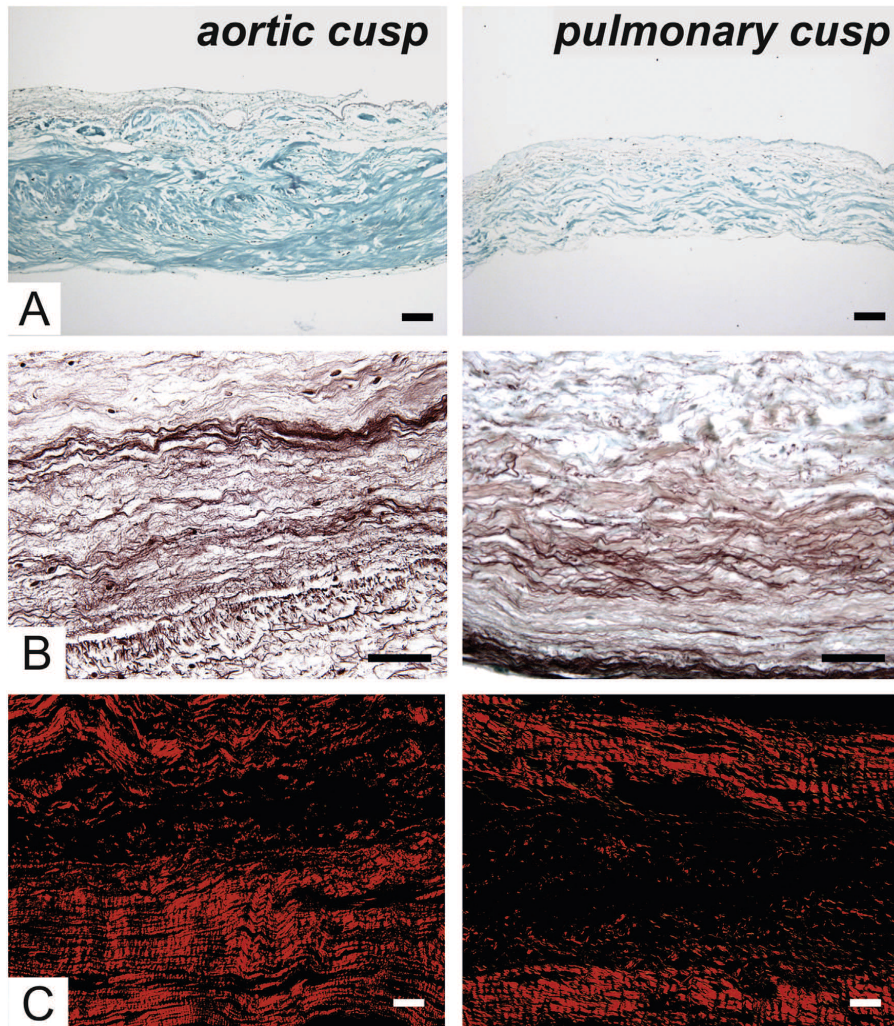
Fig. 6. Comparison of the aortic and pulmonary cusps. (A) The whole wall of an aortic cusp was greater than the wall thickness of the pulmonary valve cusps ($p < 0.001$). Verhoeff's haematoxylin and green trichrome stained the collagen green and elastin black. Scale bar, 500 μm. (B) There were no differences between the area fraction of elastin in the aortic cusps and pulmonary cusps. Red–brown elastic fibres were stained with orcein in the media. Scale bar, 100 μm. (C) The area fraction of collagen in the aortic cusps was greater than the area fraction of collagen in the pulmonary cusps ($p < 0.05$). The red type I collagen was stained with picrosirius red and was viewed with polarized light. Scale bar, 50 μm. (For interpretation of the references to colour in this figure legend, the reader is referred to the web version of this article.)

Table 3
The mean values and standard deviations of biomechanical and histological parameters in cusps of aortic and pulmonary valves.

Evaluated parameter	Aortic cusp			Pulmonary cusp		
	n	Mean	Standard deviation	n	Mean	Standard deviation
Young's modulus in small deformation (MPa)	38	3.43	6.68	29	1.88	1.86
Young's modulus in large deformation (MPa)	38	25.25	27.55	29	13.57	7.77
Ultimate stress	38	0.33	0.08	29	0.33	0.10
Ultimate strain	38	6.06	5.83	29	3.15	2.15
Wall thickness (μm)	38	555	137.95	29	437	185.45
A_A (elastin, wall)	38	0.11	0.02	29	0.11	0.03
A_A (collagen I, wall)	38	0.4	0.14	29	0.27	0.11

A_A (elastin, wall), the area fraction of elastin within wall; A_A (collagen I, wall), the area fraction of type I collagen within wall and n, number of specimens.

porcine model may not be representative of the typical aged human patient. The aged human aortic valve has stiffer mechanical properties and a different histological structure than those of moderated animal models. These animal models should be used with caution in future studies (Martin and Sun, 2012). Therefore, further studies on the usability, expiration dates and mechanical properties of human cryopreserved samples should be performed on human specimens. However, human specimens are extremely scarce because most are used in cardiac reconstruction surgery. Currently, only cryopreserved human valve allografts that have been cryopreserved for less than five years are used. This is based on the usage of tissue banks and existing results from studies of five-year-old cryopreserved samples (Goffin et al., 1996). Unfortunately, there are no studies comparing the mechanical properties and histological compositions of these samples with those that have been cryopreserved for longer periods of time. However, more aortic and pulmonary valves and roots would be required for an evaluation of the influence of time of cryostorage on the tissue morphology and biomechanical properties. A power analysis for estimating the minimum number of samples per group may be easily calculated from our results (Tables 2 and 3, Supplements 1 and 2 (in Supplementary data)). For example, the minimum number of aortic cusps needed for a reliable detection of a 25% drop in the ultimate strain (i.e., mean values 0.33 vs. 0.248 with standard deviation of 0.08) would require a minimum of 9 samples per each group, using the typical test power $1 - \beta = 0.8$ (where β is the type II error) and $\alpha = 0.05$ (where α is the type I error) (Chow et al., 2008). However, other parameters with a relatively greater biological variability might require a greater sample size.

Our results may be used to optimise the compositions of tissue-engineered valves to mimic real samples. Furthermore, our results may be used for computational modelling of the mechanics of heart valve cusps (Prot et al., 2010).

There were several limitations in the present study. Some of the parameters (such as wall thickness) may have been affected by minor differences in sample orientation and embedding. Additionally, our study included only uniaxial loading. Biaxial loading is known to provide more complex insight into the mechanical behaviour of cardiovascular samples (Metzler et al., 2012); however, we chose uniaxial loading and the Young's modulus of elasticity in two linear regions, namely the region of small deformations and the region of large deformations, to obtain a simple and physically meaningful characteristic of the passive mechanical behaviour of heart valves cusps, aortic roots and pulmonary trunks. This characteristic could be easily used to compare the various groups of allografts. To consider extending the cryopreserved allograft heart valve expiration limit to longer than 5 years, it is necessary to investigate larger groups of grafts cryopreserved for both less than 5 years and more than 5 years and to match the tested groups according to at least the age and sex of donors.

5. Conclusion

Biomechanical properties such as the Young's modulus of elasticity in the large deformation region and ultimate strain were moderately positively correlated with intima-media thickness in elastic artery samples. The ultimate strain had a moderately negative correlation with the area fraction of elastin, a moderately negative correlation with the area fraction of calcification in the intima-media and a moderately positive correlation with the area fraction of collagen in the walls of arteries. A weak positive correlation was found between the cusp wall thickness and Young's moduli and ultimate stress. The propagation of experimentally induced microcracks avoided elastic fibres. The results of the mechanical tests could not be completely explained by the histological analyses of the main tissue constituents. Therefore, both

methods should be considered complementary and should be used in further studies on the durability and ageing of cryopreserved aortas, pulmonary trunks and aortic and pulmonary cusps.

Appendix A. Supplementary data

Supplementary data associated with this article can be found, in the online version, at http://dx.doi.org/10.1016/j.aanat.2017.03.004.

References

Arabkhani, B., Mookhoek, A., Di Centa, I., Lansac, E., Bekkers, J.A., De Lind Van Wijngaarden, R., Bogers, A.J.J.C., Takkenberg, J.J.M., 2015. Reported outcome after valve-sparing aortic root replacement for aortic root aneurysm: a systematic review and meta-analysis. Ann. Thorac. Surg. 100, 1126–1131, http://dx.doi.org/10.1016/j.athoracsur.2015.05.093.

Azadani, A.N., Chitsaz, S., Matthews, P.B., Jaussaud, N., Leung, J., Wisneski, A., Ge, L., Tseng, E.E., 2012. Biomechanical comparison of human pulmonary and aortic roots. Eur. J. Cardiothorac. Surg. 41, 1111–1116, http://dx.doi.org/10.1093/ejcts/ezr163.

Balaoing, L.R., Post, A.D., Liu, H., Minn, K.T., Grande-Allen, K.J., 2014. Age-related changes in aortic valve hemostatic protein regulation. Arterioscler. Thromb. Vasc. Biol. 34, 72–80, http://dx.doi.org/10.1161/ATVBAHA.113.301936.

Bashey, R.I., Torii, S., Angrist, A., 1967. Age-related collagen and elastin content of human heart valves. J. Gerontol. 22, 203–208.

Buchanan, R.M., Sacks, M.S., 2014. Interlayer micromechanics of the aortic heart valve leaflet. Biomech. Model. Mechanobiol. 13, 813–826, http://dx.doi.org/10.1007/s10237-013-0536-6.

Burkert, J., Krs, O., Vojáček, J., Mokráček, A., Slížová, D., Hlubocký, J., Kobylka, P., Špatenka, J., 2008. Cryopreserved semilunar heart valve allografts: leaflet surface damage in scanning electron microscopy. Zentralbl. Chir. 133, 367–373, http://dx.doi.org/10.1055/s-2008-1076872.

Chow, S.-C., Shao, J., Wang, H. (Eds.), 2008. Chapman & Hall/CRC Biostatistics Series. , 2nd ed. Chapman & Hall/CRC, Boca Raton.

Doehring, L.C., Kaczmarek, P.M., Ehlers, E., Mayer, B., Erdmann, J., Schunkert, H., Aherrahrou, Z., 2006. Arterial calcification in mice after freeze–thaw injury. Ann. Anat. 188, 235–242.

Goffin, Y., Grandmougin, D., Van Hoeck, B., 1996. Banking cryopreserved heart valves in Europe: assessment of a 5-year operation in an international tissue bank in Brussels. Eur. J. Cardiothorac. Surg. 10, 505–512.

Hinton, R.B., Yutzey, K.E., 2011. Heart valve structure and function in development and disease. Annu. Rev. Physiol. 73, 29–46, http://dx.doi.org/10.1146/annurev-physiol-012110-142145.

Hlubocký, J., Mokráček, A., Nováček, V., Vojáček, J., Burkert, J., Kochová, P., Klepáček, J., Pepper, J., Špatenka, J., 2011. Mechanical properties of mitral allografts are not reasonably influenced by cryopreservation in sheep model. Physiol. Res. 60, 475–482.

Hopkins, R.A., 2005. Cardiac Reconstructions with Allograft Tissues. Springer-Verlag, New York.

Huygens, S.A., Mokhles, M.M., Hanif, M., Bekkers, J.A., Bogers, A.J.J.C., Rutten-van Mölken, M.P.M.H., Takkenberg, J.J.M., 2016. Contemporary outcomes after surgical aortic valve replacement with bioprostheses and allografts: a systematic review and meta-analysis. Eur. J. Cardiothorac. Surg. 50 (4), 605–616, http://dx.doi.org/10.1093/ejcts/ezw101.

Kochová, P., Kuncová, J., Švíglerová, J., Cimrman, R., Miklíková, M., Liška, V., Tonar, Z., 2012. The contribution of vascular smooth muscle, elastin and collagen on the passive mechanics of porcine carotid arteries. Physiol. Meas. 33, 1335–1351, http://dx.doi.org/10.1088/0967-3334/33/8/1335.

Kočová, J., 1970. Overall staining of connective tissue and the muscular layer of vessels. Folia Morphol. (Praha) 18, 293–295.

Li, Z.-Y., U-King-Im, J., Tang, T.Y., Soh, E., See, T.C., Gillard, J.H., 2008. Impact of calcification and intraluminal thrombus on the computed wall stresses of abdominal aortic aneurysm. J. Vasc. Surg. 47, 928–935, http://dx.doi.org/10.1016/j.jvs.2008.01.006.

Marra, S.P., Daghlian, C.P., Fillinger, M.F., Kennedy, F.E., 2006. Elemental composition, morphology and mechanical properties of calcified deposits obtained from abdominal aortic aneurysms. Acta Biomater. 2, 515–520, http://dx.doi.org/10.1016/j.actbio.2006.05.003.

Martin, C., Sun, W., 2012. Biomechanical characterization of aortic valve tissue in humans and common animal models. J. Biomed. Mater. Res. A 100, 1591–1599, http://dx.doi.org/10.1002/jbm.a.34099.

Metzler, S.A., Digesu, C.S., Howard, J.I., Filip To, S.D., Warnock, J.N., 2012. Live en face imaging of aortic valve leaflets under mechanical stress. Biomech. Model. Mechanobiol. 11, 355–361, http://dx.doi.org/10.1007/s10237-011-0315-1.

Meyers, M.A., Chen, P.-Y., Lin, A.Y.-M., Seki, Y., 2008. Biological materials: structure and mechanical properties. Prog. Mater. Sci. 53, 1–206, http://dx.doi.org/10.1016/j.pmatsci.2007.05.002.

Mouton, P.R., 2002. Principles and Practices of Unbiased Stereology: an Introduction for Bioscientists. Johns Hopkins University Press, Baltimore.

Otto, S., Baum, T., Keller, F., 2006. Sex-dependence of the relative number of elastic fibres in human heart valves. Ann. Anat. 188, 153–158, http://dx.doi.org/10.1016/j.aanat.2005.08.017.

Pham, T., Sun, W., 2014. Material properties of aged human mitral valve leaflets: mechanical properties of aged human Aml and Pml. J. Biomed. Mater. Res. A 102, 2692–2703, http://dx.doi.org/10.1002/jbm.a.34939.

Prosecká, E., Rampichová, M., Vojtová, L., Tvrdík, D., Melčáková, S., Juhasová, J., Plencner, M., Jakubová, R., Jančář, J., Nečas, A., Kochová, P., Klepáček, J., Tonar, Z., Amler, E., 2011. Optimized conditions for mesenchymal stem cells to differentiate into osteoblasts on a collagen/hydroxyapatite matrix. J. Biomed. Mater. Res. A 99, 307–315, http://dx.doi.org/10.1002/jbm.a.33189.

Prot, V., Skallerud, B., Sommer, G., Holzapfel, G.A., 2010. On modelling and analysis of healthy and pathological human mitral valves: two case studies. J. Mech. Behav. Biomed. Mater. 3, 167–177, http://dx.doi.org/10.1016/j.jmbbm.2009.05.004.

Špatenka, J., Kostelka, M., Kobylka, P., Hučín, B., Honěk, T., Lochmann, O., Hájek, T., Tláskal, T., Povýšilová, V., Fišer, B., 1997. Preparation, storage, transportation and use of heart valves for allotransplantation. Rozhl. Chir. 76, 118–125.

Stoyan, D., Kendall, W.S., Mecke, J., 1995. Stochastic geometry and its applications. In: Wiley Series in Probability and Statistics, 2nd ed. Wiley, Chichester New York.

Stradins, P., 2004. Comparison of biomechanical and structural properties between human aortic and pulmonary valve*1. Eur. J. Cardiothorac. Surg. 26, 634–639, http://dx.doi.org/10.1016/j.ejcts.2004.05.043.

Tonar, Z., Janáček, J., Nedorost, L., Grill, R., Báča, V., Zát'ura, F., 2009. Analysis of microcracks caused by drop shatter testing of porcine kidneys. Ann. Anat. 191, 294–308, http://dx.doi.org/10.1016/j.aanat.2009.02.005.

Tonar, Z., Kubíková, T., Prior, C., Demjén, E., Liška, V., Králíčková, M., Witter, K., 2015. Segmental and age differences in the elastin network, collagen, and smooth muscle phenotype in the tunica media of the porcine aorta. Ann. Anat. 201, 79–90, http://dx.doi.org/10.1016/j.aanat.2015.05.005.

Veselý, I., 1998. The role of elastin in aortic valve mechanics. J. Biomech. 31, 115–123.

Vincent, J.F.V., 1990. Structural Biomaterials, Rev. ed. Princeton University Press, Princeton, N.J.

Vojáček, J., Mokráček, A., Špatenka, J., Vambera, M., Šulda, M., Šetina, M., Burkert, J., Pavel, P., Pepper, J., 2006. Implantation of cryopreserved mitral allograft into the tricuspid position in an experimental study in sheep: technical aspects of implantation and immediate results evaluated by epicardial echocardiography. Zentralbl. Chir. 131, 511–516, http://dx.doi.org/10.1055/s-2006-955455.

Weinberg, E.J., Shahmirzadi, D., Mofrad, M.R.K., 2010. On the multiscale modeling of heart valve biomechanics in health and disease. Biomech. Model. Mechanobiol. 9, 373–387, http://dx.doi.org/10.1007/s10237-009-0181-2.

Příloha II:

TONAR, Z., **KUBIKOVA, T.**, PRIOR, C., DEMJEN, E., LISKA, V., KRALICKOVA, M., WITTER, K. Segmental and age differences in the elastin network, collagen, and smooth muscle phenotype in the tunica media of the porcine aorta. Ann Anat. 2015; 201:79-90. DOI: 10.1016/j.aanat.2015.05.005. ISSN 0940-9602. IF=1.483.

Contents lists available at ScienceDirect

Annals of Anatomy

Research Article

Segmental and age differences in the elastin network, collagen, and smooth muscle phenotype in the tunica media of the porcine aorta

Zbyněk Tonar [a,*], Tereza Kubíková [a], Claudia Prior [b], Erna Demjén [c], Václav Liška [d], Milena Králíčková [a], Kirsti Witter [b]

[a] Department of Histology and Embryology and Biomedical Centre, Faculty of Medicine in Pilsen, Charles University in Prague, Husova 3, 306 05 Pilsen, Czech Republic
[b] Institute of Anatomy, Histology and Embryology, Department of Pathobiology, University of Veterinary Medicine Vienna, Veterinärplatz 1, A-1210 Vienna, Austria
[c] Department of Biophysics, Institute of Experimental Physics, Slovak Academy of Sciences, Watsonova 47, 043 53 Kosice, Slovak Republic
[d] Department of Surgery and Biomedical Center, Faculty of Medicine in Pilsen, Charles University in Prague, Husova 3, 306 05 Pilsen, Czech Republic

ABSTRACT

The porcine aorta is often used in studies on morphology, pathology, transplantation surgery, vascular and endovascular surgery, and biomechanics of the large arteries. Using quantitative histology and stereology, we estimated the area fraction of elastin, collagen, alpha-smooth muscle actin, vimentin, and desmin within the tunica media in 123 tissue samples collected from five segments (thoracic ascending aorta; aortic arch; thoracic descending aorta; suprarenal abdominal aorta; and infrarenal abdominal aorta) of porcine aortae from growing domestic pigs ($n = 25$), ranging in age from 0 to 230 days. The descending thoracic aorta had the greatest elastin fraction, which decreased proximally toward the aortic arch as well as distally toward the abdominal aorta. Abdominal aortic segments had the highest fraction of actin, desmin, and vimentin positivity and all of these vascular smooth muscle markers were lower in the thoracic aortic segments. No quantitative differences were found when comparing the suprarenal abdominal segments with the infrarenal abdominal segments. The area fraction of actin within the media was comparable in all age groups and it was proportional to the postnatal growth. Thicker aortic segments had more elastin and collagen with fewer contractile cells. The collagen fraction decreased from ascending aorta and aortic arch toward the descending aorta. By revealing the variability of the quantitative composition of the porcine aorta, the results are suitable for planning experiments with the porcine aorta as a model, i.e. power test analyses and estimating the number of samples necessary to achieving a desirable level of precision. The complete primary morphometric data, in the form of continuous variables, are made publicly available for biomechanical modeling of site-dependent distensibility and compliance of the porcine aorta.

© 2015 Elsevier GmbH. All rights reserved.

1. Introduction

The porcine aorta is often used in studies on morphology, pathology, transplantation surgery, vascular and endovascular surgery, and biomechanics of the large arteries. Although aged human aortae contain less elastin and more collagen and are therefore stiffer than the corresponding porcine aortic segments (Martin

* Corresponding author at: Department of Histology and Embryology and Biomedical Centre, Faculty of Medicine in Pilsen, Charles University in Prague, Karlovarska 48, 301 66 Pilsen, Czech Republic. Tel.: +420 607818614.
E-mail address: tonar@lfp.cuni.cz (Z. Tonar).

et al., 2011), there are no alternative large laboratory species. The pig aorta is currently the best described and most suitable animal model of the human aorta in terms of its caliber as well as gross and microscopic morphology or physiology.

Examples of studies using porcine aorta as a model for the human aorta comprise models of aortic coarctation (Hu et al., 2008), post-vagotomy remodeling (Sokolis et al., 2005), thoracic sympathectomy (Angouras et al., 2012), and models of abdominal aortic aneurysm (AAA) (Hynecek et al., 2007; Molacek et al., 2009; Houdek et al., 2013). Porcine models of AAA are used for the introduction of mesenchymal stem cells into aortic injury (Turnbull et al., 2011), simulation of ruptured AAA repair (Suk et al., 2012), testing of endovascular repair techniques (Lederman et al., 2014), and

stent grafts (Saari et al., 2012). Worthley et al. (2000) showed that the porcine abdominal aorta has histopathological lesions that are comparable to human atherosclerosis.

1.1. The tunica media as a carrier of the mechanical properties of the aortic wall

As a typical elastic artery (Mayersbach, 1956), the tunica media of the aorta is a composite structure consisting of vascular smooth muscle cell (VSMC) layers that are periodically reinforced by an elastic network and collagen fiber bundles (Shadwick, 1999). The matrix fibers and the amorphous matrix are produced by and attached to the VSMC (Shadwick, 1999). The specific influence of these constituents on the mechanical behavior has been assessed by their selective removal from the vessel wall (Gundiah et al., 2007; Gundiah et al., 2009; Gundiah et al., 2013; Zou and Zhang, 2012; Zeinali-Davarani et al., 2013; also cf. Kochova et al., 2012). The contribution of elastin to the inflation response of the porcine thoracic aorta has been thoroughly mapped by Lillie et al. (2012). The tunica media of the porcine aorta seems to have similar elastic properties throughout its thickness (Stergiopulos et al., 2001; Gundiah et al., 2007). Using the isolated elastic network, advanced biomechanical models of porcine aortic elastin behavior have been developed (Watton et al., 2009; Lillie et al., 2010; Weisbecker et al., 2013). The application of elastin-specific magnetic resonance contrast agents allows for three-dimensional imaging (Makowski et al., 2012) at a lower resolution than conventional histology.

The inhomogeneous distribution of collagen fibers in the porcine aortic wall was recently reported by Sugita and Matsumoto (2013a), who detected higher collagen content in the dorsal and distal parts of the aorta than in the ventral and proximal wall regions. This finding might explain the localization of the predilection sites of aortic wall disruption, such as dissection and aneurisms, because its tensile strength depends on the intramural collagen fiber content and alignment (Kochova et al., 2012; Sugita and Matsumoto, 2013b).

VSMCs contain not only actin microfilaments and desmin intermediate filaments, they also contain vimentin intermediate filaments (Gabbiani et al., 1981; Fujimoto et al., 1987). VSMCs can modulate their phenotype from contractile (more actin and desmin) to synthesis (less actin and desmin, more vimentin, and higher proliferative activity) (Miyazaki et al., 2002; Owens et al., 2004; Boccardi et al., 2007). Actin, desmin, and vimentin can be detected in both porcine and human aortic samples using the same antibodies, their immunopositivity is robust and therefore easily to be quantified (Witter et al., 2010; Houdek et al., 2013; Eberlova et al., 2013). The Advanced models of the aortic wall are currently able to link the macroscopic mechanical behavior of the whole arteries with the cytoskeletal filaments of individual VSMCs (Unterberger et al., 2013).

1.2. Age-related and segmental differences in the porcine aorta

For experiments on the porcine aorta, animals of various ages are used, depending on the study design, experiment time points, post-operative follow-up, diet duration, etc. Most of the studies cited above analyze animals ranging in age between 0 days up to 6 months, depending also on the period of analysis. However, studies on postnatal ontogenesis of the porcine aorta composition are scarce, although changes in the tunica media composition described in people (e.g. Martin et al., 2011, Tsamis et al., 2013) might alert us to consider these developmental changes.

In general, the abdominal aorta is more accessible for vascular or endovascular surgery than the thoracic aorta; therefore, it has been established as a model of thoracic aortic dissection and in the application of vascular prostheses (Witter et al., 2010; Dziodzio et al., 2011; Okuno et al., 2012; Johnson et al., 2013). Using aorta

segments as a model that differs from the natural site of the modeled disease might have drawbacks, especially if the aortic wall composition and properties differ between the target sites.

Anatomically, the porcine aorta consists of the ascending aorta, aortic arch, and descending aorta, which is subdivided into the aorta thoracica and aorta abdominalis. The latter is often divided further into the suprarenal and infrarenal abdominal aorta. The structural and mechanical properties of the porcine aorta vary as a function of distance from the heart. Davidson et al. (1985) suggested that the VSMC phenotype of the porcine aortic wall is distinct in different regions. Lillie and Gosline (2007) reported that the elastin meshwork in the thoracic aorta might become progressively anisotropic with increasing distance from the heart. Sugita and Matsumoto (2013a) found more collagen in the distal and dorsal aortic regions than in the proximal and ventral regions. Tremblay et al. (2010) reported heterogeneous orientation, density and contractile properties of aortic VSMCs within the ascending porcine aorta. Further segmental differences of the smooth muscle orientation along the entire porcine aorta have recently been reported (Tonar et al., 2015).

Histological and biomechanical differences between the aortic segments were mapped by Sokolis (2007) and Sokolis et al. (2008), who found a predominance of elastin over collagen in the proximal segments of aortic wall as well as a predominance of collagen over elastin in distal segments. Kim and Baek (2011) and Kim et al. (2013) reported a biomechanical variability among circumferential and longitudinal aortic regions, reporting the greatest elastic moduli in the posterior distal regions. However, systematic histological and histopathological studies, including of the whole porcine aorta, as in Sokolis et al. (2008), are still very rare in spite of the importance and number of papers on the porcine aorta. Contributing to the knowledge on segmental and age-related differences became the rationale for our study.

1.3. Study aims

The aim of our study was to assess the quantity of elastin, collagen, alpha smooth muscle actin, desmin, and vimentin using transversal histological sections of the porcine aorta and to compare these data between single aorta segments and age groups. The following null hypotheses were formulated and tested:

$H_0(A)$: The area fraction of elastin, collagen, smooth muscle actin, vimentin, and desmin is the same in all proximodistal aortic segments of the same individuals when comparing the aortae of growing domestic pigs (age 0–230 days).

$H_0(B)$: The area fraction of elastin, collagen, smooth muscle actin, vimentin, and desmin is the same for suckling piglets, weaners, and fattening pigs when comparing corresponding aortic segments.

$H_0(C)$: The area fraction of elastin, collagen, smooth muscle actin, vimentin, and desmin does not correlate with the intima-media thickness or the wall thickness of the porcine aorta.

2. Materials and methods

2.1. Animals and specimen preparation

Whole aortae were collected from domestic pigs within a typical age range for experimental and model approaches (Molacek et al., 2009; Houdek et al., 2013; Witter et al., 2010). The animals (commercial fattening hybrids, $n = 25$; 12 males, 11 females, one castrated male, one without documented sex; age 0–230 days; weight 0.7–95 kg) were euthanized in a time frame comparable to other experiments (Ondrovics et al., 2013; Gabner et al., 2012; Worliczek et al., 2010). All of the animals were raised conventionally
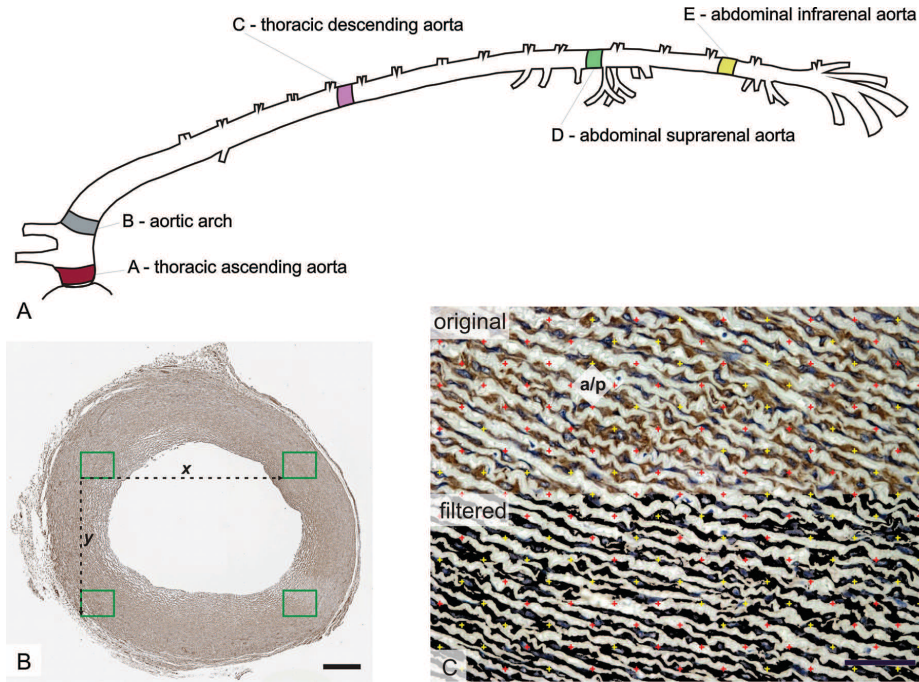
Fig. 1. Position and sampling of the porcine aortic wall for quantitative assessment of the tunica media constituents. (a) Anatomical position of the aortic segments (A–E) collected in the present study. The positions were redrawn according to the anatomical dissection of the porcine aortae (KW) and according to Nickel et al. (1996) and Tonar et al. (2015). (b) Four micrographs (demonstrated with proportionally sized rectangles) were collected from the tunica media for each tissue sample and staining method. The (x,y) distances between the micrographs were uniform in a particular section to cover the entire circumference of the tunica media including the image fields bordering with the adventitia or with the lumen. The size of the uniform sampling step (x,y) was modified proportionally to the size of any particular vascular segment. (c) The original micrographs (image given in the upper area; only the upper half of the original image is shown) were processed and the pixels representing the original brown areas of staining positivity were replaced with black (the lower area of the image; the lower half of the thresholded image is shown). Using a stereological point grid, the number of points hitting the highlighted black color was counted automatically. The positive staining area of interest was calculated for each staining method by multiplying the number of positive points with the area associated with each point (a/p). The reference area of the tunica media was quantified using the same point grid. In 48 images, the counting was performed both with and without thresholding and the resulting area estimates were paired and statistically compared. Immunohistochemical detection of alpha-smooth muscle actin (B) and vimentin (C), visualization horseradish peroxidase/diaminobenzidine, and counterstaining with hematoxylin. Scale bar (b) 500 μm and (c) 50 μm.

and treated in compliance with the European Convention on Animal Care. A large subset of the samples analyzed for this study has already been used in a study on the orientation of smooth muscle cells in the tunica media (Tonar et al., 2015).

Immediately after dissection, aortae without any macroscopic signs of pathological changes were routinely fixed in buffered formalin according to Lillie (Romeis, 1989) and divided into five aortic segments representing the following regions: ascending aorta (aorta ascendens), aortic arch (arcus aortae), thoracic descending aorta (aorta thoracica), abdominal suprarenal aorta (aorta abdominalis, pars suprarenalis), and abdominal infrarenal aorta (aorta abdominalis, pars infrarenalis) (Fig. 1a). In total, 123 tissue samples were collected (two infrarenal segments were missing as they were damaged during dissection). After fixation, the samples were rinsed in 70% ethanol, dehydrated in ethanol and embedded in paraffin using a Shandon Excelsior tissue processor (Thermo Scientific, Fremont, CA, USA). From each aortic segment, one tissue block was embedded for transversal sectioning. To compare the aortic samples according to the age groups, the animals were divided into the following three groups: suckling piglets (age 0–28 days, $n = 64$ vascular segments collected from 13 animals), weaners (age 29–75 days, $n = 35$ vascular segments collected from seven animals) and fattening pigs (age 180–230 days, $n = 24$ vascular segments from five animals).

2.2. Preparation of histological sections

Six serial histological sections per sample (section thickness of 4 μm) were cut and mounted on Super Frost slides coated with (3-aminopropyl)triethoxysilane (Sigma-Aldrich, Vienna, Austria). The cutting plane was perpendicular to the longitudinal axis of the vessel. The sections were deparaffinized and rehydrated. In one section, the overall morphology of the aortic wall was shown using a combination of Verhoeff's hematoxylin and green trichrome staining according to Kocova (1970). In another section, only the elastic network was stained using orcein (Tanzer's orcein, Bowley Biochemical Inc., Danvers, MA, USA) for 12 min without nuclear counterstaining. In another section, only the collagen was stained using picrosirius red (Direct Red 80, Sigma-Aldrich, Munich, Germany) diluted in saturated picric acid solution for 1 h. In each of the remaining sections, α-smooth muscle actin, desmin, and vimentin were detected imunohistochemically to characterize the vascular smooth muscle cells (Table 1 for the manufacturers and details of the antibodies and immunohistochemical processing).

For immunohistochemistry, endogenous peroxidase activity was blocked in the rehydrated sections with 0.6% H_2O_2 in methanol, which was followed by antigen demasking, if necessary, as described in Table 1. Unspecific binding activity was blocked with normal goat serum (1.5% in phosphate-buffered saline (PBS), pH

Table 1
Primary antibodies used for immunohistochemistry.

Antibody	Manufacturer	Dilution factor	Final antibody concentration (mg/l)	Pretreatment
Monoclonal Mouse Anti-Human Smooth Muscle Actin, Clone 1A4 (smooth muscle phenotype marker)	DakoCytomation (Glostrup, Denmark)	1:400	0.178	None
Monoclonal Mouse Anti-Human Desmin, Clone D33 (smooth muscle contractile phenotype marker)	DakoCytomation	1:300	0.400	Microwave cooking in TRIS−EDTA, pH 9, 3 × 5 min
Monoclonal Mouse Anti-swine Vimentin, Clone V9 (synthetic smooth muscle phenotype marker)	DakoCytomation	1:200	1.03	Microwave cooking in citrate buffer, pH 6.0, 5 min

7.4; DakoCytomation, Glostrup, Denmark). Afterwards, the sections were incubated overnight with primary antibodies as specified in Table 1. The products of the immunoreaction were detected using the BrightVision Poly HRP-anti-mouse kit (ImmunoLogic, Duiven, The Netherlands) according to manufacturer's instructions. The reactions were visualized with diaminobenzidine (Sigma-Aldrich, Vienna, Austria) in 0.03% H_2O_2 in PBS. After immunohistochemistry, the sections were counterstained with Mayer's hematoxylin, dehydrated and mounted with a medium soluble in xylene.

2.3. Quantification of the area fraction of elastin, collagen, actin, desmin, and vimentin

From each section, 4 micrographs were collected in a systematic, uniform, random manner; i.e. 4 micrographs per staining method and 16 micrographs per each of the 123 tissue samples for a total 1968 micrographs. We used a 40× objective mounted on the Olympus BX51 microscope. This magnification provided a resolution that guaranteed reliable visual control of all immunopositive regions as well as the fine bridges and branches between the elastic lamellae and the collagen in a satisfactorily large field of view. The unbiased sampling of the micrographs from the sections is explained in Fig. 1b.

The original micrographs (see the upper area in Fig. 1c for an example) were processed using the ColorFilter module of the Ellipse software (VIDITO, Kosice, Slovak Republic) to highlight the staining. This module reads the hue-saturation-brightness (HSB) values (for a detailed description of color models and their application on image segmentation, see Cheng et al., 2001) from pixels clicked by the user as a learning sample. Multiple learning samples of pixels may be collected from the image. Then, the module highlights all pixels within the marked range of selected HSB values and changes their color to any artificial color that is selected by the user. In our case, we replaced the brown areas of orcein of picrosirius red positive staining or the diaminobenzidine-positive brown areas with black (RGB values (0,0,0)). This black color was absent from the original micrographs. Whenever the micrograph contained a region outside the area of interest (e.g. the vascular lumen or the tunica adventitia), only the region of the tunica media was manually selected for analysis using the polygone tool in the software.

Afterwards, a stereological point grid (PointGrid module of the Ellipse software, cf. Howard and Reed, 1998) was loaded and randomly superposed on the micrographs. The number of points hitting the highlighted black color (RGB 0,0,0) was counted automatically using a Threshold function set to the corresponding zero grayscale value (for an example, see lower area in Fig. 1c). The user (ZT) checked the thresholding of the point grid before the results were saved and used for further calculations. The point grid method allowed for individual corrections of the reference space (i.e. the tunica media) for any possible artifacts as well as correction of the reference space if there were microcracks or the adventitia or vascular lumen were present in the field of view. At least 150 intersections of the point grid per each section and method were always used for estimating the area fractions. The profile area of elastin, actin, desmin, and vimentin positivity was then calculated for each staining method by multiplying the number of points with the area associated with each point according to the image and grid calibration. The profile area of the tunica media within the image field was assessed in the same manner, excluding the adventitia, aortic lumen, and artifacts. The area fraction of elastin, actin, desmin, and vimentin within the tunica media represented on the actual micrographs was calculated as the ratio of the profile area of interest and reference area (profile area of the tunica media).

Highlighting the stained structures increased the speed of the point grid estimates significantly, because only points hitting the black pixels were automatically selected during the point grid thresholding. The advantage of combining highlighting of pixels representing positively stained tissue components with fast thresholding of classical stereological point grid is as follows: after adaptive modifying, the contrast depending on the particular staining intensity (evaluated by a histologist), the results of the thresholding of stereological grid can still be supervised by a histologist to correct any false positivity or false negativity and to correct the background area of interest. As both steps may be processed in stacks of micrographs, the sequence of these steps is significantly faster than classical manual point counting, but the robustness of the stereological point counting method is retained. To test the reliability of the highlighting, we performed a pilot study. We took three sets of images per staining method, and each of the 12 sets consisted of four images. In these selected sets, classical manual point counting methods were performed on the original unmodified micrographs three months after evaluating the highlighted images (ZT). The area of the stained structures resulting from the highlighting and automatic point grid was paired with the area that resulted from the fully manual point grid counting in the original micrographs ($n = 48$). The Wilcoxon-matched pairs test did not find a difference between the two methods ($p = 0.430$). All results presented below are based on the faster automatic method.

2.4. Measurement of the intima-media thickness

The thickness of the tunica intima and media was measured in the transverse histological sections as described previously (Tonar et al., 2015). We measured the intima-media thickness instead of the media thickness itself because most samples lacked a visually distinct border between the media and intima with the latter consisting of a flat endothelial layer and a very thin subendothelial connective tissue layer. To exclude any effects of deformation of the aorta due to histological processing, the wall thickness was assessed as follows. In micrographs of the complete transverse sections of the aorta, the outline of the vascular lumen and media/adventitia border were traced using a graphic tablet and the polygon tool of the morphometric Ellipse software package. We used software to calculate the circumference values (U).

The undeformed cross section of the aorta was considered a circle; therefore, the inner diameter and "outer" diameter, including the intima and media (d), were calculated as $d = U/\pi$. The mean thickness of the aortic tunica intima/media complex was calculated as a ratio $(d_1-d_2)/2$, where d_1 was the outer diameter and d_2 was the inner diameter. A subset of the intima-media thickness values has been recently published in a study on the orientation of smooth muscle cells (Tonar et al., 2015). The total wall thickness was measured using the same approach. Because the phenomenon of tissue shrinkage due to histological processing is well-known (Rieger et al., 2013), the absolute parameters in this study; i.e. the thickness of intima-media and the aortic wall, are not expected to match the values found intra vitam and, therefore, were considered supplementary results used for correlation analysis only. To test the reliability of the thickness estimation in samples with slightly ellipsoidal cross-sectional profile, the thickness was also measured in 20 micrographs by manually drawing four equidistant calibrated lines per image, connecting the inner surface of the intima with the last regular elastic lamella of the medina (intima-media thickness) and the outermost layer of the adventitia (wall thickness). The mean lengths of each set of lines were compared with the thickness calculated from the aortic diameters (see above). The Wilcoxon-matched pairs test did not find a difference between the two methods ($p = 0.560$). Therefore, it seems that the method used for estimating the mean thickness is robust even to slight deviations from the circular shape.

2.5. Statistics

Shapiro−Wilk's W-test was used for the normality testing of the data. In some of the aortic segments, the distribution of the values differed from the normal distribution; therefore, we used nonparametric statistics for further analysis. The Wilcoxon-matched pairs test was used to compare the manual area estimates using the point grid in original micrographs with the automatic area estimates using the point grid automatic thresholding in images with highlighted positivity of the markers under study. The Friedman ANOVA test and Wilcoxon-matched pair test were used to assess the differences between the corresponding aortic segments (A−E) in the animals under study. The Kruskal−Wallis ANOVA test and Mann−Whitney U-test were used to assess the differences between the age groups. The correlation between the area fractions of the tunica media components and intima-media thickness was evaluated using the Spearman correlation coefficient. These tests were used as available in the Statistica Base 11 package (StatSoft, Inc., Tulsa, OK, USA).

3. Results

3.1. Segmental differences in the tunica media composition

A number of differences were found when comparing the values in all aortic proximodistal segments of the same individuals. The results are displayed and statistics are summarized in Fig. 2. The $H_0(A)$ hypothesis was rejected for all tunica media constituents under study. The area fraction of elastin (Fig. 2a) showed highly significant differences between nearly all aortic segments under study, which was followed by actin (Fig. 2c), desmin (Fig. 2d), and vimentin content (Fig. 2e). The greatest area fraction of elastin (Fig. 2a) was found in the thoracic descending aorta, which was followed by the aortic arch, thoracic ascending aorta, and suprarenal and infrarenal aorta. The area fraction of collagen (Fig. 2b) showed a proximodistal decrease only when comparing the ascending aorta with the thoracic descending and abdominal suprarenal aorta, as well as when comparing the aortic arch with the suprarenal abdominal aorta.

The greatest area fraction of actin (Fig. 2c), desmin (Fig. 2d), and vimentin (Fig. 2e) was observed in both segments of the abdominal aorta, which was followed by the thoracic descending aorta, aortic arch, and ascending aorta. The thoracic ascending aorta did not differ from the aortic arch in any of the parameters except for having a lower fraction of desmin positivity. No differences were found when the suprarenal abdominal aorta was compared with the infrarenal abdominal aorta.

3.2. Comparison of the tunica media composition between the age groups

The quantitative results displaying age differences in the composition of the aortic wall are summarized in Fig. 3. The $H_0(B)$ hypothesis was retained for actin (Fig. 3c) only, but it was rejected for elastin (Fig. 3a), collagen (Fig. 3b), desmin (Fig. 3d), and vimentin (Fig. 3e). The area fraction of elastin within the media was lower in fattening pigs than in weaners. The area fraction of collagen was greater in fattening pigs than in suckling pigs. The area fraction of actin within the media was comparable in all age groups. The area fraction of desmin was lower in suckling piglets than in weaners or fattening pigs. The area fraction of vimentin gradually decreased with age: it was greater in suckling piglets than in weaners and fattening pigs, and it was greater in the weaners than in fattening pigs.

3.3. Correlation of the tunica media composition with the thickness of the aortic wall

The non-parametric Spearman rank-order correlations between quantitative parameters are listed in Table 2, and the significant values ($p < 0.05$) are highlighted. The $H_0(C)$ is rejected for all of the parameters under study; i.e. the area fraction of tissue components in the tunica media correlates with both the intima-media thickness and the aortic wall thickness.

Selected micrographs with both segmental and age-related differences of the aortic wall composition are shown in Figs. 4 and 5. Subtle differences, e.g. the slightly smaller area fraction of elastin and greater fraction of collagen in the ascending aorta compared with the descending thoracic aorta were not visible by simple microscopic examination (Fig. 4a−c) and were detectable only by quantitative assessment of the vessel wall components. However, the increasing area fraction of actin in the proximodistal direction was clearly visible even by microscopic examination (Fig. 5a and b). As the micrographs show, there were no differences in immunohistochemical VSMC markers between the suckling piglets and weaners except the greater fraction of desmin in weaners. The desmin positivity was low in the thoracic aorta and if present, it was limited to individual VSMCs. Desmin increased from the thoracic aorta toward the abdominal aorta, and it also visibly increased with age (Fig. 5c and d). Vimentin positivity was uniformly distributed in the wall of all aortic segments and age groups. The higher level of vimentin in the abdominal aorta compared with the thoracic aorta was only detectable by quantitative assessment (Fig. 5e and f), which was also true for its tendency to decrease with age. The complete data set with all the morphometric results for all of the samples of all aortic segments is provided in Supplement 1.

4. Discussion

4.1. The thoracic aorta has a different composition than the abdominal aorta

Following the aortic segments in the proximodistal direction, the elastin content increased and reached its maximum in the thoracic descending aorta and then decreased to a minimum in
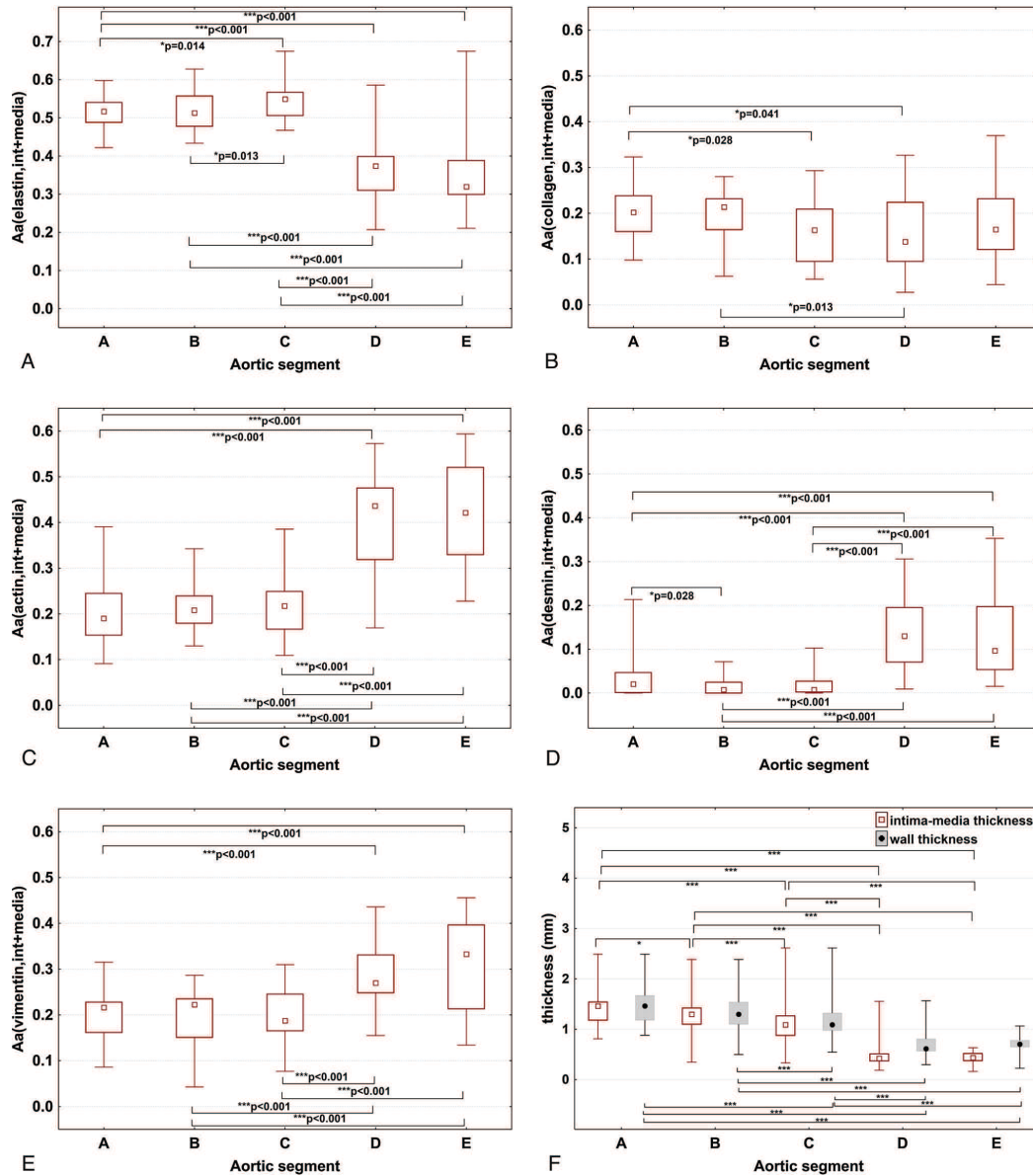
Fig. 2. Area fractions (A_A) of (a) elastin, (b) collagen, (c) alpha-smooth muscle actin, (d) desmin and (e) vimentin within the aortic tunica media, (f) intima-media thickness and (f) aortic wall thickness in five aortic segments of the pig in the proximo-distal direction. Segments A, B, C, D, and E denote the aorta ascendens, arcus aortae, thoracic aorta descendens, suprarenal, and infrarenal abdominal aorta, respectively. Age groups were pooled for this comparison. Only the corresponding paired values from the same individuals were tested. Significant p-values of the Wilcoxon-matched pairs test are presented (except in E). Data are displayed as the median values with boxes spanning the upper limits of the first and third quartiles and with whiskers spanning the minimum and maximum values for each group.

the abdominal aorta. Surprisingly, the wall of the suprarenal aorta was comparable to the wall of the infrarenal abdominal aorta. The infrarenal aorta showed a tendency toward a lower elastin content (Fig. 3a) and higher vimentin positivity (Fig. 3d) than the suprarenal aorta, but none of these differences were significant in paired samples of the suprarenal and infrarenal abdominal aorta.

The higher elastin content of the thoracic aorta compared with the abdominal aorta that we observed in our study is consistent with the results of a number of studies in different mammalian species (e.g. Guo and Kassab, 2004; Sokolis et al., 2008; Dinardo et al., 2014). Most authors directly attributed the differences in the mechanical behavior of the aortic wall to different elastin content
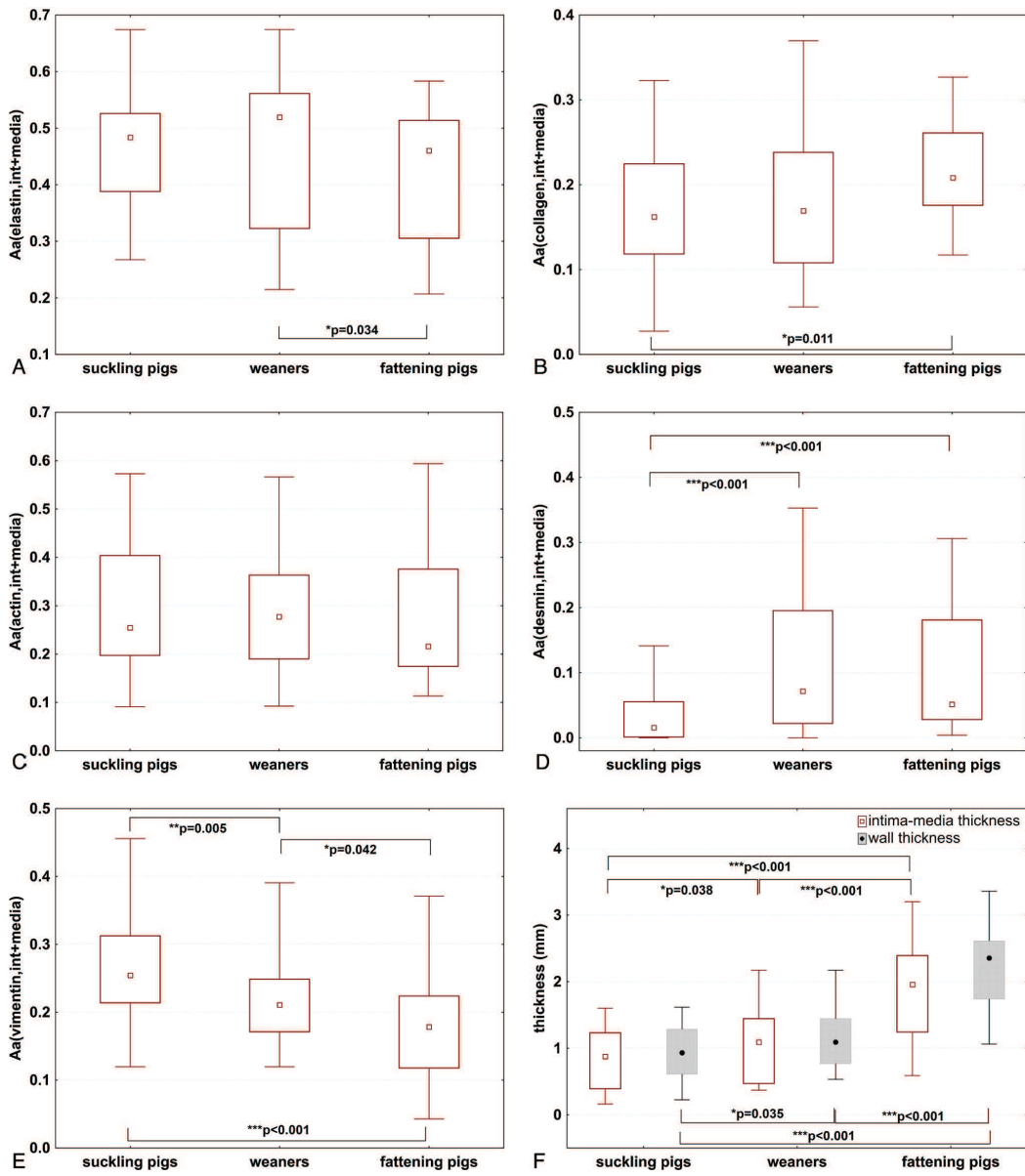
Fig. 3. (A_A) Area fractions of (a) elastin, (b) collagen, (c) smooth muscle actin, (d) desmin and (e) vimentin within the aortic tunica media, (f) intima-media thickness and (f) aortic wall thickness in three pig age groups. Aortic segments were pooled for this comparison. The significant p-values for the Mann–Whitney test are presented. Data are displayed as the median values with boxes spanning the upper limits of the first and third quartiles and with whiskers spanning the minimum and maximum values for each group.

in the tunica media. For example, Guo and Kassab (2004) observed a lower stretch ratio and Cauchy stress in the porcine thoracic aorta, and Roach and Song (1994) observed that the abdominal aorta tears more easily while needing higher pressure for propagation of the defect when liquid is injected into the tunica media. Dinardo et al. (2014) observed higher stiffness in the abdominal aorta due to reduced elastin content. In addition to the mechanical function

of elastin in the aortic wall, this protein might be important in the progression of inflammatory changes because Lannoy et al. (2014) observed elastin, together with fibrillin, acts as an autocrine factor that regulates the activity and availability of TGFs within the tissue. Interestingly, the lower level of elastin in the ascending aorta and aortic arch in our study has not been mentioned in any other studies even though disorders, such as thoracic aortic aneurisms,

Table 2
Spearman rank-order correlations between the quantitative parameters.

	A_A(collagen)	A_A(actin)	A_A(desmin)	A_A(vimentin)	IMT	WT
A_A(elastin)	−0.14	**−0.60***	**−0.52***	**−0.37***	**0.38***	**0.30***
A_A(collagen)	–	**−0.57***	−0.11	−0.06	**0.22***	**0.20***
A_A(actin)		–	**0.56***	**0.43***	**−0.54***	**−0.44***
A_A(desmin)			–	**0.27***	**−0.26***	−0.16
A_A(vimentin)				–	**−0.49***	**−0.48***
IMT					–	**0.97***

Note: The data were pooled across the experimental groups. A_A(component) stays for the area fraction of the respective component within the tunica intima and media reference spaces; IMT, intima-media thickness and WT, wall thickness. All correlations significant at $p < 0.05$ are marked (*) and typed in bold face. Remaining correlations have no statistical significance ($p > 0.05$). Autocorrelations and repeating values are replaced by the − sign.

are known to have a predilection site exactly within the proximal aortic regions (Kuzmik et al., 2012). The combination of high blood pressure in the most proximal aortic segments and somewhat smaller levels of elastin in the tunica media might lead to decreased resilience of this region of the cardiovascular system.

The ascending aorta seems to differ from the aortic arch and descending thoracic and abdominal aorta in its elastin content and the phenotype of its vascular smooth muscle cells (VSMCs). Ko et al. (2001) found a predominantly desmin negative and connexin 43 positive cell populations in the aortic arch and descending thoracic aorta of the rat as well as predominantly desmin positive and connexin 43 negative VSMC populations in the abdominal aorta. Desmin and connexin positive VSMCs were restricted to the ascending aorta in rats. In our study, the connexin expression of VSMCs was not studied; however, even in the porcine aorta, there was a higher level of desmin in the tunica media of the ascending aorta compared with the aortic arch (with a trend in the descending thoracic aorta). In general, our results confirmed a higher relative level of (actin positive) VSMCs in the abdominal aorta compared with the segments of the thoracic aorta within the vessel wall. These data support the results of Arnaud (2000), who reported higher metabolic activity and a resulting decreased tolerance against cryopreservation in the distal aortic wall segments. Information about the distribution of VSMC phenotypes within the aorta and the vascular tree might help us to understand the development of atherosclerosis and its predilection sites because (at least in humans) VSMCs with a synthetic phenotype can proliferate and produce matrix, playing an important role in the progression of this disease (Rao et al., 2000).

4.2. The elastin and collagen fractions remained constant in weaners, but actin fraction remained constant during growth even in fattening pigs

The increase in wall thickness (Fig. 3f) was not accompanied by significant age-related changes in the elastin and collage fractions in weaners until the day 75. The results suggest that the elastin and collagen formation continues in suckling pigs after birth and in weaners proportionally with thickening of the aortic wall, which corresponds with the high fractions of vimentin-positive mesenchyme-derived cells that are producing the extracellular matrix fibers. In fattening pigs older than 180 days, the elastin decreased and collagen increased (Fig. 4a and b). Should we speculate about an explanation, this could be caused by a lower rate of elastin synthesis during aging. Also metalloproteases or fibrinolytic factors affecting the remodeling of aortic wall (Krikova et al., 2009) could be involved. Interestingly, actin fraction was not affected by the age of the animals at all.

4.3. Thicker aortic segments have more elastin and collagen with lower fraction of contractile cells

It should be noted that the aortic thickness depends on two variables simultaneously, namely it increases with age (Fig. 3f), but it

decreases in the proximodistal direction (Fig. 2f). Therefore, the correlation coefficients provided in the Table 2 describe the resulting effects of both age of animals and anatomical localization of the samples and have to be interpreted in the context of the results summarized in Figs. 2 and 3. The correlation analysis between the elastin and VSMC markers showed that increased wall thickness in proximal aortic segments is statistically linked with higher elastin and collagen content, and inversely, a lower fraction of actin, desmin, and vimentin. The overall desmin fraction was lower than vimentin, which is consistent with the original findings by Frank and Warren (1981), who reported that the vimentin intermediate filament predominates over desmin filaments in aortic VSMCs. Moreover, some regulatory functions that are not directly related to tension and contraction have been attributed to these VSMC intermediate filaments, including cell division, migration, and gene expression (for review, see Tang, 2008).

4.4. Study implications

The knowledge of segmental and age-related biological variability of the porcine aorta is useful when planning experiments with thoracic and abdominal aortas and estimating the number of animals involved. Due to the rapid growth of piglets, this will be beneficial for experiments done with the growing porcine model, in which the growth of the arterial wall is a part of the experimental design, such as experiments with aortic reconstruction and aortic arch replacement (Ioannou et al., 2003; Chen et al., 2012), studies on post-operative aortic compliance (Ioannou et al., 2013), and arterial banding simulating the palliative pulmonary artery surgery of newborn infants with congenital heart defects (Nedorost et al., 2013). The aortic wall composition should be further correlated with quantification of vasa vasorum (Witter et al., 2010; Tonar et al., 2012) and with the distribution of aortic branching points (cf. Panagouli et al., 2011). The lack of quantitative differences in the wall composition between the supra- and infrarenal abdominal aorta in our study provides interesting information about the development of surgical approaches. The infrarenal aorta is considerably easier to assess and can therefore serve as an equivalent model for the suprarenal aorta with similar histological composition. When used to model other regions of the aorta, differences in the aortic wall composition have to be carefully considered when interpreting the results.

The data provided in the Supplement 1 can be directly used in biomechanical models of the porcine aorta that are based on histological findings (Sokolis, 2010; Horný et al., 2014a, 2014b). According to the Delesse principle (Howard and Reed, 1998), the area fractions occupied by the components are consistent estimates of the corresponding volume fractions of these components. The data might contribute to explaining the circumferential distensibility and site-specific inflation–extension behavior of the abdominal aorta for predicting the outcomes of angioplasty or stenting (Maher et al., 2012). The high fractions of elastin in thoracic aorta are useful for explaining the high compliance of thoracic aorta (namely the ascending aorta and aortic arch), which serves as an elastic
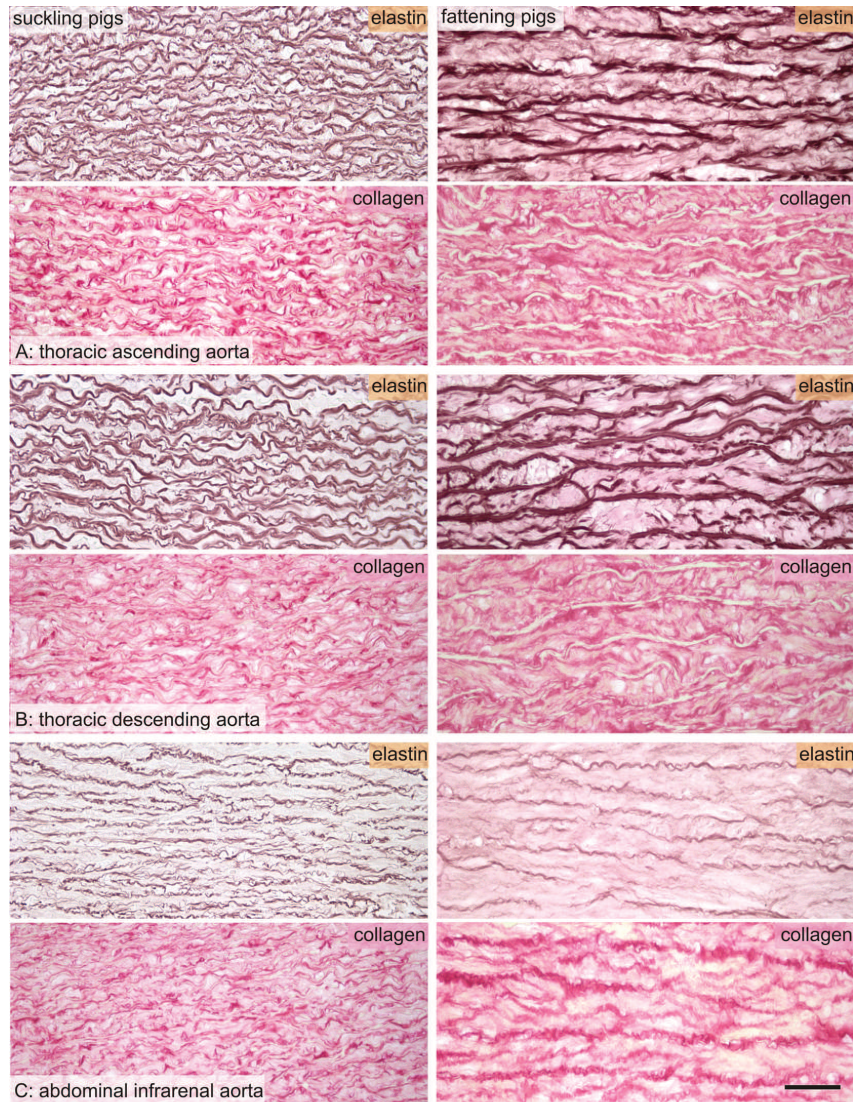
Fig. 4. Elastin and collagen content in the aortic tunica media of suckling piglets (left) and fattening pigs (right). Fattening pigs had the lowest area fraction of elastin (brown staining) and the greatest fraction of collagen (red staining). Although there were no clear differences between the area fraction of elastin and collagen within the tunica media of the (a) thoracic ascending and (b) descending aorta according to simple microscopic observation, quantitative analysis demonstrated that the fraction of elastin was generally larger and the fraction of collagen was generally smaller in the thoracic (b) descending aorta than in the thoracic (a) ascending aorta (cf. Fig. 3a,b). The area fraction of elastin within the media was the smallest in the (c) infrarenal abdominal aorta, where medium values of collagen fraction were found. Elastin stained with orcein; collagen stained with picrosirius red; nuclei were not counterstained; scale bar 50 μm.

reservoir. Thus, the aorta transforms the pulsatile cardiac output to a more constant flow by absorbing the systolic kinetic energy and emitting it back during diastole, which is known as the "Windkessel effect" studied both in human (Gülan et al., 2014) as well as in pig (Krüger et al., 2015). Modeling of the porcine aorta biomechanics greatly overlaps with models of the human aorta (Holzapfel and Ogden, 2010; Wilson et al., 2012; Schriefl et al., 2012; Humphrey and Holzapfel, 2012). For this purpose, the growth of aortic wall may be described using the growth curves according to Gielecki et al. (2006) or Szpinda (2007).

4.5. Study limitations

The wall thickness measurements were affected by dissecting the aortae and by the post-mortem contraction of the vascular segments. However, an effort was made to manipulate all aortic samples in the same way to preserve the natural outer borders of the aortic wall. We did not perform any correction for tissue shrinkage. However, we encountered almost no ruptures or microcracks within the tunica media and no gaps between the tissue constituents. Therefore, no traces of significant differential
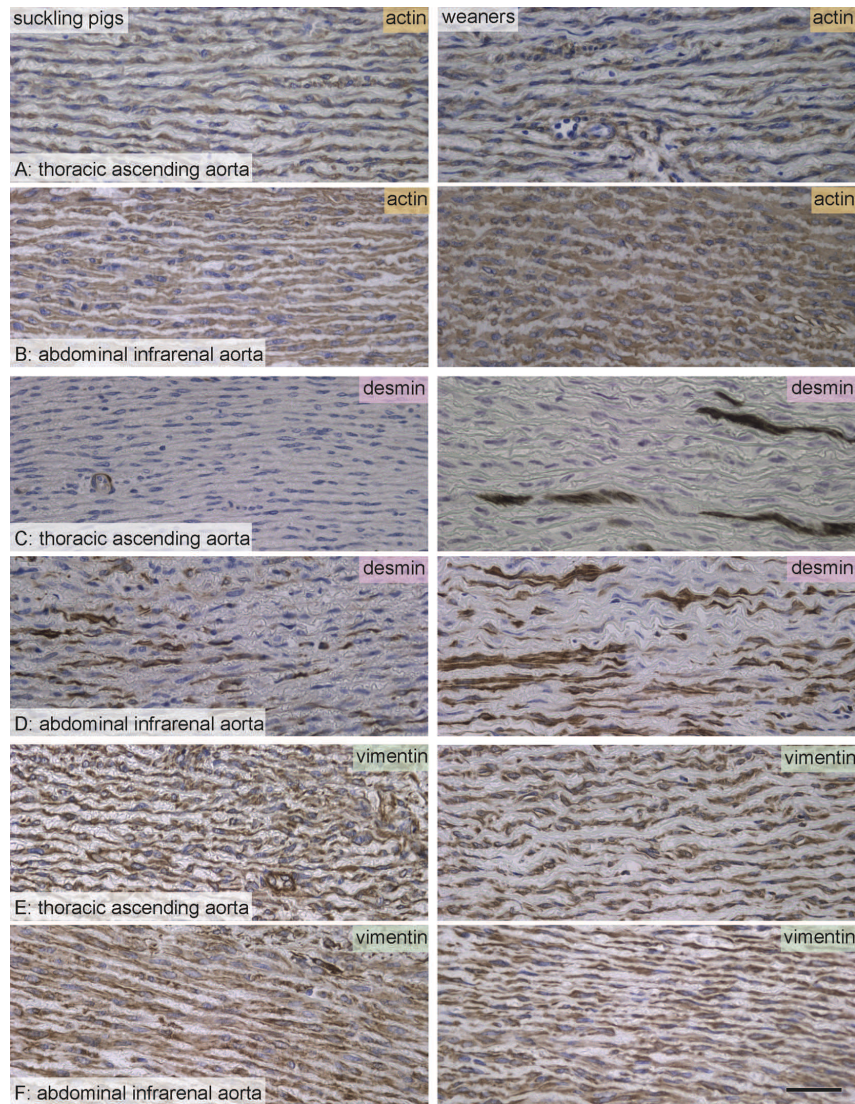
Fig. 5. Actin, desmin, and vimentin content in the aortic tunica media of suckling piglets (left) and weaners (right). The area fraction of actin (brown staining in a,b) was higher in the (b) abdominal infrarenal aorta than in the (a) thoracic ascending aorta and showed no differences between the suckling piglets and weaners. Nearly absent desmin positivity (brown staining in c, d) in the thoracic aorta of suckling piglets, which was mostly limited to the (c) vasa vasorum vascular profiles. Desmin positivity increased in the proximodistal direction in suckling piglets as well as in weaners (compare c and d). Desmin was more frequent in weaners than in suckling pigs (cf. Fig. 3). Vimentin positivity (brown staining in e and f) was higher in the abdominal infrarenal aorta than in the thoracic ascending aorta. Vimentin positivity in weaners was lower than in suckling pigs. For quantitative comparison, see Fig. 3b–d. Immunohistochemical detection of alpha smooth muscle actin, desmin, and vimentin; visualization with horseradish peroxidase/diaminobenzidine and counterstaining with hematoxylin. Scale bar 50 μm.

shrinkage were found between the elastin, collagen, VSMCs, and other constituents of the tunica media during the fixation, embedding, or sectioning. Therefore, the area fractions that we estimated were most likely not biased by the shrinkage. We present the data as mean values for the tunica media without describing any radial differences across the tunica media. Assessing the differences between the elastin lamellar units would have required perfusion fixation to exclude any bias introduced by post-mortem contraction.

Additionally, the presence of the vasa vasorum within the tunica media could be a source of bias because it is elastin-negative, but actin-, desmin-, and vimentin positive. Our study did not differentiate samples from the dorsal, lateral, and ventral sides of the abdominal aorta. Another limitation is that the estimates were always based on one section per staining and anatomical position. Due to the number of animals, we did not perform simultaneous statistics with grouping of the samples according to the aortic segments and the age.

5. Conclusion

Using quantitative histology, we estimated the area fraction of elastin, collagen, smooth muscle actin, vimentin, and desmin within the tunica media in 123 tissue samples collected from five segments of the porcine aortae from growing domestic pigs, ranging in age from 0 to 230 days. The descending thoracic aorta had the highest elastin fraction, which decreased proximally toward the aortic arch as well as distally toward the abdominal aorta, where it reached a minimum in the infrarenal segment. The collagen fraction decreased from ascending aorta and aortic arch toward the descending aorta. The abdominal aortic segments had the highest fraction of actin, desmin, and vimentin positivity, and all of these vascular smooth muscle markers were smaller in the thoracic aortic segments. No quantitative differences were found when comparing the suprarenal abdominal segments with the infrarenal abdominal segments. The area fraction of actin within the media was comparable in all age groups, and it was proportional to the postnatal growth up to 7 months of age. Thicker aortic segments had more elastin and more collagen with fewer contractile cells. Our results are consistent with other studies on the porcine aorta. By revealing the variability of the quantitative composition of the porcine aorta, our results are suitable for planning experiments with the porcine aorta as a model; i.e. power test analyses and estimating the number of samples necessary to attain a desirable level of precision. The complete primary morphometric data in the form of continuous variables are made publicly available for biomechanical modeling of site-dependent distensibility and compliance of the porcine aorta.

Acknowledgments

Appendix A. Supplementary data

Supplementary data associated with this article can be found, in the online version, at http://dx.doi.org/10.1016/j.aanat.2015.05.005

References

Angouras, D.C., Dosios, T.J., Dimitriou, C.A., Chamogeorgakis, T.P., Rokkas, C.K., Manos, T.A., Sokolis, D.P., 2012. Surgical thoracic sympathectomy induces structural and biomechanical remodeling of the thoracic aorta in a porcine model. J. Surg. Res. 172, 68–76.

Arnaud, F., 2000. Endothelial and smooth muscle changes of the thoracic and abdominal aorta with various types of cryopreservation. J. Surg. Res. 89, 147–154.

Boccardi, C., Cecchettini, A., Caselli, A., Camici, G., Evangelista, M., Mercatanti, A., Rainaldi, G., Citti, L., 2007. A proteomic approach to the investigation of early events involved in vascular smooth muscle cell activation. Cell Tissue Res. 328, 185–195.

Chen, C.C., Tseng, Y.C., Lin, C.C., Li, C.F., Yeh, M.L., 2012. A modular branched stent-graft system for sutureless anastomoses in extensive aortic arch replacement—a porcine study. Ann. Vasc. Surg. 26, 527–536.

Cheng, H.D., Jiang, X.H., Sun, Y., Wang, J., 2001. Color image segmentation: advances and prospects. Pattern Recogn. 34, 2259–2281.

Davidson, J.M., Hill, K.E., Mason, M.L., Giro, M.G., 1985. Longitudinal gradients of collagen and elastin gene expression in the porcine aorta. J. Biol. Chem. 260, 1901–1908.

Dinardo, C.L., Venturini, G., Zhou, E.H., Watanabe, I.S., Campos, L.C., Dariolli, R., da Motta-Leal-Filho, J.M., Carvalho, V.M., Cardozo, K.H., Krieger, J.E., Alencar, A.M., Pereira, A.C., 2014. Variation of mechanical properties and quantitative proteomics of VSMC along the arterial tree. Am. J. Physiol. Heart Circ. Physiol. 306, H505–H516.

Dziodzio, T., Juraszek, A., Reineke, D., Jenni, H., Zermatten, E., Zimpfer, D., Stoiber, M., Scheikl, V., Schima, H., Grimm, M., Czerny, M., 2011. Experimental acute type B aortic dissection: different sites of primary entry tears cause different ways of propagation. Ann. Thorac. Surg. 91, 724–727.

Eberlova, L., Tonar, Z., Witter, K., Krizkova, V., Nedorost, L., Korabecna, M., Tolinger, P., Kocova, J., Boudova, L., Treska, V., Houdek, K., Molacek, J., Vrzalova, J., Pesta, M., Topolcan, O., Valenta, J., 2013. Asymptomatic abdominal aortic aneurysms show histological signs of progression: a quantitative histochemical analysis. Pathobiology 80, 11–23.

Frank, E.D., Warren, L., 1981. Aortic smooth muscle cells contain vimentin instead of desmin. Proc. Natl. Acad. Sci. U. S. A. 78, 3020–3024.

Fujimoto, T., Tokuyasu, K.T., Singer, S.J., 1987. Direct morphological demonstration of the coexistence of vimentin and desmin in the same intermediate filaments of vascular smooth muscle cells. J. Submicr. Cytol. 19, 1–9.

Gabbiani, G., Schmid, E., Winter, S., Chaponnier, C., de Ckhastonay, C., Vandekerckhove, J., Weber, K., Franke, W.W., 1981. Vascular smooth muscle cells differ from other smooth muscle cells: predominance of vimentin filaments and a specific alpha-type actin. Proc. Natl. Acad. Sci. U. S. A. 78, 298–302.

Gabner, S., Tonar, Z., Tichy, A., Saalmüller, A., Worliczek, H.L., Joachim, A., Witter, K., 2012. Immunohistochemical detection and quantification of T cells in the small intestine of Isospora suis-infected piglets-influence of fixation technique and intestinal segment. Microsc. Res. Technol. 75, 408–415.

Gielecki, J.S., Syc, B., Wilk, R., Musiał-Kopiejka, M., Piwowarczyk-Nowak, A., 2006. Quantitative evaluation of aortic arch development using digital-image analysis. Ann. Anat. 188, 19–23.

Gülan, U., Lüthi, B., Holzner, M., Liberzon, A., Tsinober, A., Kinzelbach, W., 2014. Experimental investigation of the influence of the aortic stiffness on hemodynamics in the ascending aorta. IEEE J. Biomed. Health Inform. 18, 1775–1780.

Gundiah, N., Babu, A.R., Pruitt, L.A., 2013. Effects of elastase and collagenase on the nonlinearity and anisotropy of porcine aorta. Physiol. Meas. 34, 1657–1673.

Gundiah, N., Ratcliffe, M.B., Pruitt, L.A., 2007. Determination of strain energy function for arterial elastin: experiments using histology and mechanical tests. J. Biomech. 40, 586–594.

Gundiah, N., Ratcliffe, M.B., Pruitt, L.A., 2009. The biomechanics of arterial elastin. J. Mech. Behav. Biomed. Mater. 2, 288–296.

Guo, X., Kassab, G.S., 2004. Distribution of stress and strain along the porcine aorta and coronary arterial tree. Am. J. Physiol. Heart Circ. Physiol. 286, H2361–H2368.

Holzapfel, G.A., Ogden, R.W., 2010. Modelling the layer-specific three-dimensional residual stresses in arteries, with an application to the human aorta. J. R. Soc. Interface 7, 787–799.

Horný, L., Netušil, M., Daniel, M., 2014a. Limiting extensibility constitutive model with distributed fibre orientations and ageing of abdominal aorta. J. Mech. Behav. Biomed. Mater. 38, 39–51.

Horný, L., Netušil, M., Voňavková, T., 2014b. Axial prestretch and circumferential distensibility in biomechanics of abdominal aorta. Biomech. Model Mechanobiol. 13, 783–799.

Houdek, K., Moláček, J., Třeška, V., Křížková, V., Eberlová, L., Boudová, L., Nedorost, L., Tolinger, P., Kočová, J., Kobr, J., Baxa, J., Liška, V., Witter, K., Tonar, Z., 2013. Focal histopathological progression of porcine experimental abdominal aortic aneurysm is mitigated by atorvastatin. Int. Angiol. 32, 291–306.

Howard, C.V., Reed, M.G., 1998. Unbiased Stereology. Three-Dimensional Measurement In Microscopy. Springer, New York.

Hu, J.J., Ambrus, A., Fossum, T.W., Miller, M.W., Humphrey, J.D., Wilson, E., 2008. Time courses of growth and remodeling of porcine aortic media during hypertension: a quantitative immunohistochemical examination. J. Histochem. Cytochem. 56, 359–370.

Humphrey, J.D., Holzapfel, G.A., 2012. Mechanics, mechanobiology, and modeling of human abdominal aorta and aneurysms. J. Biomech. 45, 805–814.

Hynecek, R.L., DeRubertis, B.G., Trocciola, S.M., Zhang, H., Prince, M.R., Ennis, T.L., Kent, K.C., Faries, P.L., 2007. The creation of an infrarenal aneurysm within the native abdominal aorta of swine. Surgery 142, 143–149.

Ioannou, C.V., Stergiopulos, N., Georgakarakos, E., Chatzimichali, E., Katsamouris, A.N., Morel, D.R., 2013. Effects of isoflurane anesthesia on aortic compliance and systemic hemodynamics in compliant and noncompliant aortas. J. Cardiothor. Vasc. Anesth. 27, 1282–1288.

Ioannou, C.V., Stergiopulos, N., Katsamouris, A.N., Startchik, I., Kalangos, A., Licker, M.J., Westerhof, N., Morel, D.R., 2003. Hemodynamics induced after acute reduction of proximal thoracic aorta compliance. Eur. J. Vasc. Endovasc. Surg. 26, 195–204.

Johnson, J.J., Jacocks, M.A., Gauthier, S.C., Irwin, D.A., Wolf, R.F., Garwe, T., Lerner, M.R., Lees, J.S., 2013. Establishing a swine model to compare vascular prostheses in a contaminated field. J. Surg. Res. 181, 355–358.

Kim, J., Baek, S., 2011. Circumferential variations of mechanical behavior of the porcine thoracic aorta during the inflation test. J. Biomech. 44, 1941–1947.

Kim, J., Hong, J.W., Baek, S., 2013. Longitudinal differences in the mechanical properties of the thoracic aorta depend on circumferential regions. J. Biomed. Mater. Res. A 101, 1525–1529.

Ko, Y.-S., Coppen, S.R., Dupont, E., Rothery, S., Severs, N.J., 2001. Regional differentiation of desmin, connexin43, and connexin45 expression patterns in rat aortic smooth muscle. Arterioscler. Thromb. Vasc. Biol. 21, 355–364.

Kocova, J., 1970. Overall staining of connective tissue and the muscular layer of vessels. Fol. Morphol. 18, 293–295.

Kochova, P., Kuncova, J., Sviglerova, J., Cimrman, R., Miklíková, M., Liska, V., Tonar, Z., 2012. The contribution of vascular smooth muscle, elastin and collagen on the passive mechanics of porcine carotid arteries. Physiol. Meas. 33, 1335–1351.

Krikova, V., Korabecna, M., Kocova, J., Treska, V., Molacek, J., Tonar, Z., Tolinger, P., Nedorost, L., 2009. Quantification of plasminogen activator inhibitor type 1 in the aortic wall. Int. Angiol. 28, 44–49.

Krüger, T., Grigoraviciute, A., Veseli, K., Schibilsky, D., Wendel, H.P., Schneider, W., Schlensak, C., 2015. Elastic properties of the young aorta-ex vivo perfusion experiments in a porcine model. Eur. J. Cardiothorac. Surg. 48, 221–227.

Kuzmik, G.A., Sang, A.X., Elefteriades, J.A., 2012. Natural history of thoracic aortic aneurysms. J. Vasc. Surg. 56, 565–571.

Lannoy, M., Slove, S., Jacob, M.-P., 2014. The function of elastic fibers in the arteries: beyond elasticity. Pathol. Biol. 62, 79–83.

Lederman, A., Saliture Neto, F.T., Ferreira, R., de Figueiredo, L.F., Otoch, J.P., Aun, R., da Silva, E.S., 2014. Endovascular model of abdominal aortic aneurysm induction in swine. Vasc. Med. 19, 167–174.

Lillie, M.A., Armstrong, T.E., Gérard, S.G., Shadwick, R.E., Gosline, J.M., 2012. Contribution of elastin and collagen to the inflation response of the pig thoracic aorta: assessing elastin's role in mechanical homeostasis. J. Biomech. 45, 2133–2141.

Lillie, M.A., Gosline, J.M., 2007. Mechanical properties of elastin along the thoracic aorta in the pig. J. Biomech. 40, 2214–2221.

Lillie, M.A., Shadwick, R.E., Gosline, J.M., 2010. Mechanical anisotropy of inflated elastic tissue from the pig aorta. J. Biomech. 43, 2070–2078.

Maher, E., Early, M., Creane, A., Lally, C., Kelly, D.J., 2012. Site specific inelasticity of arterial tissue. J. Biomech. 45, 1393–1399.

Makowski, M.R., Preissel, A., von Bary, C., Warley, A., Schachoff, S., Keithan, A., Cesati, R.R., Onthank, D.C., Schwaiger, M., Robinson, S.P., Botnar, R.M., 2012. Three-dimensional imaging of the aortic vessel wall using an elastin-specific magnetic resonance contrast agent. Invest. Radiol. 47, 438–444.

Martin, C., Pham, T., Sun, W., 2011. Significant differences in the material properties between aged human and porcine aortic tissues. Eur. J. Cardiothorac. Surg. 40, 28–34.

Mayersbach, H., 1956. Der Wandbau der Gefäßübergangsstrecken zwischen Arterien rein elastischen und rein muskulösen Typs. Anat. Anz. 102, 333–360.

Miyazaki, H., Hasegawa, Y., Hayashi, K., 2002. Tensile properties of contractile and synthetic vascular smooth muscle cells. JSME Int. J. C Mech. Syst. 45, 870–879.

Molacek, J., Treska, V., Kobr, J., Certik, B., Skalicky, T., Kuntscher, V., Krizkova, V., 2009. Optimization of the model of abdominal aortic aneurysm—experiment in an animal model. J. Vasc. Res. 46, 1–5.

Nedorost, L., Uemura, H., Furck, A., Saeed, I., Slavik, Z., Kobr, J., Tonar, Z., 2013. Vascular histopathologic reaction to pulmonary artery banding in an in vivo growing porcine model. Pediatr. Cardiol. 34, 1652–1660.

Nickel, R., Schummer, A., Seiferle, E., 1996. Lehrbuch der Anatomie der Haustiere. Band III Kreislaufsystem, Haut und Hautorgane, third ed. Parey Buchverlag, Berlin, Germany.

Ondrovics, M., Silbermayr, K., Mitreva, M., Young, N.D., Razzazi-Fazeli, E., Gasser, R.B., Joachim, A., 2013. Proteomic analysis of oesophagostomum dentatum (Nematoda) during larval transition, and the effects of hydrolase inhibitors on development. PLoS ONE 8, e63955.

Okuno, T., Yamaguchi, M., Okada, T., Takahashi, T., Sakamoto, N., Ueshima, E., Sugimura, K., Sugimoto, K., 2012. Endovascular creation of aortic dissection in a swine model with technical considerations. J. Vasc. Surg. 55, 1410–1418.

Owens, G.K., Kumar, M.S., Wamhoff, B.R., 2004. Molecular regulation of vascular smooth muscle cell differentiation in development and disease. Physiol. Rev. 84, 767–801.

Panagouli, E., Lolis, E., Venieratos, D., 2011. A morphometric study concerning the branching points of the main arteries in humans: relationships and correlations. Ann. Anat. 193, 86–99.

Rao, R.N., Greer Falls, D., Gerrity, R.G., Sethuraman, S.N., Thiruvaiyaru, D.S., 2000. Intimal thickness and layering, and smooth muscle cell phenotypes in aorta of youth. Pathobiology 68, 18–28.

Rieger, J., Twardziok, S., Huenigen, H., Hirschberg, R.M., Plendl, J., 2013. Porcine intestinal mast cells. Evaluation of different fixatives for histochemical staining techniques considering tissue shrinkage. Eur. J. Histochem. 57, e21.

Roach, M.R., Song, S.H., 1994. Variations in strength of the porcine aorta as a function of location. Clin. Invest. Med. 17, 308–318.

Romeis, B., 1989. Mikroskopische Technik. Urban & Schwarzenberg, München.

Saari, P., Lähteenvuo, M., Honkonen, K., Manninen, H., 2012. Antegrade in situ fenestration of aortic stent graft: in-vivo experiments using a pig model. Acta Radiol. 53, 754–758.

Schriefl, A.J., Zeindlinger, G., Pierce, D.M., Regitnig, P., Holzapfel, G.A., 2012. Determination of the layer-specific distributed collagen fibre orientations in human thoracic and abdominal aortas and common iliac arteries. J. R. Soc. Interface 9, 1275–1286.

Shadwick, R.E., 1999. Mechanical design in arteries. J. Exp. Biol. 202, 3305–3313.

Sokolis, D.P., 2007. Passive mechanical properties and structure of the aorta: segmental analysis. Acta Physiol. 190, 277–289.

Sokolis, D.P., 2010. A passive strain-energy function for elastic and muscular arteries: correlation of material parameters with histological data. Med. Biol. Eng. Comput. 48, 507–518.

Sokolis, D.P., Boudoulas, H., Karayannacos, P.E., 2008. Segmental differences of aortic function and composition: clinical implications. Hellenic J. Cardiol. 49, 145–154.

Sokolis, D.P., Zarbis, N., Dosios, T., Papalouka, V., Papadimitriou, L., Boudoulas, H., Karayannacos, P.E., 2005. Post-vagotomy mechanical characteristics and structure of the thoracic aortic wall. Ann. Biomed. Eng. 33, 1504–1516.

Stergiopulos, N., Vulliémoz, S., Rachev, A., Meister, J.J., Greenwald, S.E., 2001. Assessing the homogeneity of the elastic properties and composition of the pig aortic media. J. Vasc. Res. 38, 237–246.

Sugita, S., Matsumoto, T., 2013a. Quantitative measurement of the distribution and alignment of collagen fibers in unfixed aortic tissues. J. Biomech. 46, 1403–1407.

Sugita, S., Matsumoto, T., 2013b. Heterogeneity of deformation of aortic wall at the microscopic level: contribution of heterogeneous distribution of collagen fibers in the wall. Bio. Med. Mater. Eng. 23, 447–461.

Suk, P., Cundrle Jr., I., Hruda, J., Vocilková, L., Konecny, Z., Vlasin, M., Matejovic, M., Pavlik, M., Zvoníček, V., Sramek, V., 2012. Porcine model of ruptured abdominal aortic aneurysm repair. Eur. J. Vasc. Endovasc. Surg. 43, 698–704.

Szpinda, M., 2007. Morphometric study of the ascending aorta in human fetuses. Ann. Anat. 189, 465–472.

Tang, D.D., 2008. Intermediate filaments in smooth muscle. Am. J. Physiol. Cell Physiol. 294, C869–C878.

Tonar, Z., Kochova, P., Cimrman, R., Perktold, J., Witter, K., 2015. Segmental differences in the orientation of smooth muscle cells in the tunica media of porcine aortae. Biomech. Model. Mechanobiol. 14, 315–332.

Tonar, Z., Kural Jr., T., Kochova, P., Nedorost, L., Witter, K., 2012. Vasa vasorum quantification in human varicose great and small saphenous veins. Ann. Anat. 194, 473–481.

Tremblay, D., Cartier, R., Mongrain, R., Leask, R.L., 2010. Regional dependency of the vascular smooth muscle cell contribution to the mechanical properties of the pig ascending aortic tissue. J. Biomech. 43, 2448–2451.

Tsamis, A., Krawiec, J.T., Vorp, D.A., 2013. Elastin and collagen fibre microstructure of the human aorta in ageing and disease: a review. J. R. Soc. Interface 10, 20121004.

Turnbull, I.C., Hadri, L., Rapti, K., Sadek, M., Liang, L., Shin, H.J., Costa, K.D., Marin, M.L., Hajjar, R.J., Faries, P.L., 2011. Aortic implantation of mesenchymal stem cells after aneurysm injury in a porcine model. J. Surg. Res. 170, e179–e188.

Unterberger, M.J., Schmoller, K.M., Bausch, A.R., Holzapfel, G.A., 2013. A new approach to model cross-linked actin networks: multi-scale continuum formulation and computational analysis. J. Mech. Behav. Biomed. Mater. 22, 95–114.

Watton, P.N., Ventikos, Y., Holzapfel, G.A., 2009. Modelling the mechanical response of elastin for arterial tissue. J. Biomech. 42, 1320–1325.

Weisbecker, H., Viertler, C., Pierce, D.M., Holzapfel, G.A., 2013. The role of elastin and collagen in the softening behavior of the human thoracic aortic media. J. Biomech. 46, 1859–1865.

Wilson, J.S., Baek, S., Humphrey, J.D., 2012. Importance of initial aortic properties on the evolving regional anisotropy, stiffness and wall thickness of human abdominal aortic aneurysms. J. R. Soc. Interface 9, 2047–2058.

Witter, K., Tonar, Z., Matejka, V.M., Martinca, T., Jonák, M., Rokosný, S., Pirk, J., 2010. Tissue reaction to three different types of tissue glues in an experimental aorta dissection model: a quantitative approach. Histochem. Cell Biol. 133, 241–259.

Worliczek, H.L., Buggelsheim, M., Alexandrowicz, R., Witter, K., Schmidt, P., Gerner, W., Saalmüller, A., Joachim, A., 2010. Changes in lymphocyte populations in suckling piglets during primary infections with Isospora suis. Parasite Immunol. 32, 232–244.

Worthley, S.G., Helft, G., Fuster, V., Fayad, Z.A., Fallon, J.T., Osende, J.I., Roqué, M., Shinnar, M., Zaman, A.G., Rodriguez, O.J., Verhallen, P., Badimon, J.J., 2000. High resolution ex vivo magnetic resonance imaging of in situ coronary and aortic atherosclerotic plaque in a porcine model. Atherosclerosis 150, 321–329.

Zeinali-Davarani, S., Chow, M.J., Turcotte, R., Zhang, Y., 2013. Characterization of biaxial mechanical behavior of porcine aorta under gradual elastin degradation. Ann. Biomed. Eng. 41, 1528–1538.

Zou, Y., Zhang, Y., 2012. Mechanical evaluation of decellularized porcine thoracic aorta. J. Surg. Res. 175, 359–368.

Příloha III:

TÁBORSKÝ, M., RICHTER, D., TONAR, Z**., KUBÍKOVÁ, T.**, HERMAN, A., PEREGRIN, J., ČERVENKOVÁ, L., HUSKOVÁ, Z., KOPKAN, L. Early morphologic alterations in renal artery wall and renal nerves in response to catheter-based renal denervation procedure in sheep: difference between single-point and multiple-point ablation catheters. Physiol Res 2017. IF=1.643.

Early morphologic alterations in renal artery wall and renal nerves in response to catheter-based renal denervation procedure in sheep: difference between single-point and multiple-point ablation catheters

Miloš Táborský,[1] David Richter,[1] Zbyněk Tonar,[2] Tereza Kubíková,[2] Aleš Herman,[3] Jan Peregrin,[3] Lenka Červenková, [3] Zuzana Husková,[3] Libor Kopkan[3]

[1] Department of Internal Medicine I, Cardiology, University Hospital Olomouc and Palacký University, Olomouc, Czech Republic

[2] Department of Histology and Embryology and Biomedical Center, Faculty of Medicine in Pilsen, Charles University in Prague, Pilsen, Czech Republic

[3] Center for Experimental Medicine, Institute for Clinical and Experimental Medicine, Prague, Czech Republic

Author for correspondence:

Miloš Táborský, MD, PhD, MBA, FESC.

Department of Internal Medicine I, Cardiology, University Hospital Olomouc and Palacký University, I. P. Pavlova 6, 775 20 Olomouc, Czech Republic

email: milos.taborsky@seznam.cz

phone: + 420 588 443 201

Short title: **Renal denervation in sheep**

Summary:

Renal sympathetic hyperactivity is critically involved in hypertension pathophysiology; renal denervation (RDN) presents a novel strategy for treatment of resistant hypertension cases. This study assessed effects of two RDN systems to detect acute intravascular, vascular and peri-vascular changes in the renal artery, and renal nerve alterations, in the sheep. The procedures using a single-point or multi-point ablation catheters, Symplicity Flex^{TM}, Medtronic versus EnligHTN^{TM}, St. Jude Medical were compared; the intact contralateral kidneys served as controls. Histopathological and immunohistochemical assessments were performed 48 hours after RDN procedures; the kidney and suprarenal gland morphology was also evaluated. Special staining methods were applied for histologic analysis, to adequately score the injury of renal artery and adjacent renal nerves. These were more pronounced in the animals treated with the multi-point compared with the single-point catheter. However; neither RDN procedure led to complete renal nerve ablation. Forty-eight hours after the procedure no significant changes in plasma and renal tissue catecholamines were detected. The morphologic changes elicited by application of both RDN systems appeared to be dependent on individual anatomical variability of renal nerves in the sheep. Similar variability in humans may limit the therapeutic effectiveness of RDN procedures used in patients with resistant hypertension.

Introduction:

Renal sympathetic innervation is involved not only in the regulation of renal function, circulating fluid volume and homeostasis of ions, but also in the regulation of blood pressure (Johns *et al.* 2011). Activation of efferent renal sympathetic nerves leads to water retention, sodium reabsorption and reduction of renal blood flow, as well as activation of the renin-angiotensin-aldosterone system (DiBona 2000). Although the mechanisms that link these conditions in resistant hypertension are not fully elucidated, enhanced sympathetic nervous system activity is considered as a major contributing factor (Rippy *et al.* 2011, Tsioufis *et al.* 2011). Therefore catheter-based renal denervation (RDN) has been applied as a potential cost-effective approach for patients with resistant hypertension unresponsive to standard antihypertensive therapy (Rippy *et al.* 2011). Although this method has been very widely applied over the last five years and claimed to be effective for blood pressure (BP) reduction in select patients (Bhatt *et al.* 2014, Mahfoud *et al.* 2013), satisfactory safety and efficacy data are still not available.

The evidence from preclinical experimental studies related to the safety and effectiveness of different radiofrequency-based RDN systems is limited. A single-point catheter system (the Symplicity Flex from Medtronic) has been used extensively in pig, sheep and human studies (Rippy *et al.* 2011, Bhatt *et al.* 2014, Mahfoud *et al.* 2013, Booth *et al.* 2015, Sakakura *et al.* 2015). The originally promising results of the Symplicity HTN-1 and 2 studies have been recently challenged by the early-terminated Symplicity HTN-3 study, which proposed more rigorous endpoints than did the previous studies (Mahfoud *et al.* 2013). Furthermore, the preclinical animal studies provided only inconclusive data regarding effectiveness of the denervation procedures. Some recent studies also address the issue of the

reinnervation of the kidney within months after RDN (Booth *et al.* 2015, Sakakura *et al.* 2015).

An innovative multi-ablation device, the EnligHTN™ multi-electrode RNA catheter from St. Jude Medical has been tested in pig, dog and also in humans (Worthley *et al.* 2013, Henegar *et al.* 2014, Gan *et al.* 2015, Mahfoud *et al.* 2016). This multi-point ablation catheter operates at multiple depth levels of the renal artery at the same time. Thus the adjacent nerve bundle is supposed to be more affected by the radio-frequency energy applied; on the other hand, several locations of the vascular wall within this single cross section are also affected, which could result in severe damage of the renal artery. No data have been provided so far to compare the morphological effects of the one-point and multi-point systems in the acute phase.

In the context of the above evidence the main goal of this study was to assess the acute morphologic effects and thereby evaluate to some extent the safety of two renal denervation systems using a single-point or multi-point ablation catheters in the sheep. The safety was verified by angiography and the evaluation of the kidney and the suprarenal gland morphology. The effectiveness of either RDN procedure was assessed by comparing histopathologic and immunohistochemical features of intra-vascular, vascular and peri-vascular structures between the renal artery subjected to RDN and the contralateral renal artery. In addition, the levels of catecholamines were determined in the intact and post-RDN kidney.

Methods:

The study performed in sheep (total n = 12; body weight 35-48 kg) was approved by the Institute for Clinical and Experimental Medicine Animal Care and Use Committee in

accordance with the regulations accepted in the Czech Republic and guidelines from Directive 2010/63/EU of the European Parliament. The sheep model can be regarded as optimal for RDN in many respects: the adult animal is large and shows minimal body weight gain over time, which is of obvious advantage with long-term experiments. In consequence, the results of acute and chronic studies can be readily compared over prolonged period of time. Last but not least, the commercially available ablation catheters fit the diameter of the renal artery in the sheep.

Renal artery angiography and RDN procedure:

The sheep were randomly assigned into two mixed-sex groups, each containing six animals. Anaesthesia was induced with combination of propofol (10 mg/kg; Fresenius Kabi, Bad Homburg, Germany) and fentanyl (3 mg/kg; Torrex, Chiesi, Wien, Austria) given intravenously. After endotracheal intubation, anesthesia was maintained with 0.5% to 2.0% isoflurane (Isofluran Rhodia, Nicholas Piramar, Mumbai, India) in O_2/air mixture. The right femoral artery incision was performed as the access point for the catheterization, a sheath was introduced into the exposed artery and heparin (3000 IU) was administered. After that a pigtail catheter was inserted through the sheath into the abdominal aorta to reach the area where the renal arteries originate from the aorta. Angiography was performed using a standard contrast agent (Telebrix 35, Guerbet BP, Roissy CdG Cedex, France) injection to assess the above-defined area before application of the RDN procedure. The guiding catheter was inserted into the right renal artery and then the appropriate ablation catheter approved for the clinical use (Symplicity Flex[TM], Medtronic, INC, Santa Rosa, CA, USA or EnligHTN[TM] Basket, St. Jude Medical, INC, Saint Paul, MN, USA), was connected to a generator and RDN procedure was performed. Both RDN systems are fully automatic with predefined limits. The Medtronic generator utilizes an algorithm for the delivery within 120 s of

radiofrequency energy (4-8 W) with maximal temperature limit 75 °C. The EnligHTN generator employs 60 s cycle of radiofrequency energy of 3-6 W for each of four electrodes, with maximal temperature limit 70 °C. When RDN procedure was completed, the ablation catheter was removed, and angiography of both arteries was repeated. After the experiments the catheter, wire and sheath were withdrawn, the femoral wound was closed and sheep were monitored till full recovery from anaesthesia. For analgesia butorphanol 0.2-0.4 mg/kg s.c. (Torbugesic, Zoetis Manufacturing and Reserch Spain S.L., Vall de Bianya, Spain) was administered when needed.

Forty-eight hours post-RDN the animals were anesthetized and prepared (by the same procedure as described above) for another angiography of both renal arteries via left femoral artery. Then the abdomen was opened for gross examination of the kidneys, the tissue samples of the both intact and intervened kidney were taken and immediately frozen in liquid nitrogen, for later catecholamine assays. After that the animals were euthanized by an anaesthetic overdose (thiopental, VUAB Brno, Czech Repaublic) together with KCl, then the aorta was clamped proximally and the kidneys were flushed with 10% buffered formalin via an introduced angiography catheter. The whole block (the abdominal aorta with attached renal arteries and kidneys) was excised for histological examination.

Histological processing:

From each animal under study, tissue samples were removed for histological assessment of renal arteries and the accompanying nerves (8-9 samples per each renal artery that were processed in series of transversal sections), the kidneys (8 samples to include all anatomical zones), and the suprarenal gland (1-2 samples to include each anatomical part). The extensive sampling scheme was identical for organs subjected to RDN and for the intact contralateral organs.

Seven staining procedures including four immunohistochemical methods were applied and combined to reveal the most important microscopic features of the vascular wall, sympathetic peripheral nerves, kidney and suprarenal gland morphology: Hematoxylin-eosin; Verhoeff's hematoxylin and green trichrome; Mallory trichrome; Orcein (Tanzer's orcein, Bowley Biochemical Inc., Danvers, MA, USA); the Monoclonal Mouse Anti-Human Smooth Muscle Actin Antibody, Clone 1A4, dilution 1:100, pretreatment Target Retrieval Solution, pH 9.0, 96°C, 20 min; the Monoclonal Mouse Anti-Human Neurofilament Protein Antibody, Clone 2F11, dilution 1:75, pretreatment Target Retrieval Solution, pH 6.0, 96°C, 20 min; the Polyclonal Rabbit Anti-Tyrosine Hydroxylase, pretreatment Target Retrieval Solution, pH 9.0, 96°C, 20 min; the Polyclonal Rabbit Anti-Human Von Willebrand Factor, solution 1:200, pretreatment 10 min in chilled acetone and Proteinase K; the binding of the primary antibody was visualized using the peroxidase reaction and 3,3´-diaminobenzidine (these chemicals form DakoCytomation, Glostrup, Denmark).

Histological evaluation of the intact and post-RDN renal arteries, renal nerves, kidneys and suprarenal glands

The histological changes reflecting injuries found in the renal artery and in nerves surrounding the renal artery after 48 hours post-RDN procedure, as well as their classification and scoring are given in Table 1. Typical examples of the renal artery injury are shown in Figure 1, and the injury of the renal nerves is presented in Figure 2. The scoring system reflected either severity (or grade) of the damage to the artery wall and adjacent nerves, and the relative extent of these changes. After performing the scoring, the values calculated for each sample under study were listed and presented in Table 2.

Measurement of catecholamines in the renal tissue and plasma

The tissue samples were homogenized in phosphate buffer with protease inhibitors and ascorbic acid and centrifuged (10 000 G, 10 minutes, 4°C); full blood samples with EDTA were centrifuged (10 000 G, 10 minutes, 4°C) and assayed by TriCat TM Elisa kit (IBL International, Hamburg, Germany).

Statistical analysis:

Nonparametric statistics was used: the Wilcoxon matched pairs test was used to compare the results found in RDN intervened and intact organs of the same animal. The Mann-Whitney U-test was used to assess the differences between the results of intervention using two different types of catheters. The correlation between the parameters calculated from the scoring systems was evaluated using the Spearman correlation coefficient. These tests were used as available in the Statistica Base 11 package (StatSoft, Inc., Tulsa, OK, USA).

Results:

Pre- and post-RDN angiography of the renal artery

The post-RDN angiography indicated that neither of RDN systems caused any serious alteration of renal blood flow in the intervened kidney confirming the safety of these procedures. No evidence of adverse effects, such as renal artery stenosis, thrombosis, perforation or spasm was apparent based on angiography immediately post-procedure or 48 hours later, suggesting that no major renal vascular abnormality occurred after RDN procedure.

Vascular and nerve injury status with and without RDN intervention

The scoring system showed that the sum, the maximum, and the mean vascular injury score were greater after intervention compared to the contralateral untreated renal artery in both groups of animals: those treated with the Symplicity Flex catheter and the EnligHTN catheter. However, in the former group the difference in nerve injury score did not reach significance when compared with the nerves surrounding the renal artery without intervention. In contrast, the nerve injury score was significantly greater after intervention with the EnligHTN catheter compared to the nerves of the untreated renal artery (Figure 3).

Vascular and nerve injury caused by the two types of the catheter

Compared with the impact of the Symplicity Flex catheter, RDN procedure using the EnligHTN catheter resulted in significantly greater injury to the renal artery (Figure 3A) and also in a greater nerve injury score (Figure 3B).

Typical histological findings showing the wall of renal arteries after RDN intervention are depicted in Figure 4. In the renal arteries treated with the Symplicity catheter, the lesions of the vascular wall were less extensive, often restricted to only one quadrant of the vascular section (Figure 4A-C). In one animal, more quadrants were affected (Figure 4D). In arteries treated with the EnligHTN catheter, the vascular lesions were more extensive, often affecting multiple quadrants in cross sections of several segments (Figure 4 E-H). Except for the circular layer of smooth muscle, all renal arteries examined in this sheep model had also an additional layer of longitudinal smooth muscle (Figure 4).

Typical findings in the nerves accompanying the renal arteries are illustrated in Figure 5. In many sections, morphologically normal unaltered nerves were found, often running in the direction opposite to those in the damaged arterial quadrant (Figure 5A and 5E). All types of nerve injury as shown in Figure 5B-D and 5F-H, and also in Figure 2, were more

pronounced in the animals treated with the EnligHTN catheter when compared with those treated with the Symplicity catheter.

Histological findings in the kidneys and suprarenal glands after intervention

Figure 6 represents histological findings illustrating normal appearance of the kidneys and the suprarenal glands after either RDN intervention. No signs of ischemia, haemorrhage, necrosis, or increased leukocyte infiltration were found in the renal cortex (Figure 6A and 6E) or medulla (Figure 6B and 6F). Both neurofilament protein-positive as well as tyrosine-hydroxylase-positive nerve fibres were found in samples of all tissue blocks from all kidneys under study (Figure 6C and 6G). In all samples of the suprarenal gland, a well-defined tyrosine-hydroxylase positive medulla was seen (Figure 6D and 6H); there was no difference between individual experimental groups.

Plasma and kidney catecholamine levels in anesthetized sheep

Compared to basal dopamine (0.73 ± 0.49 ng/ml), norepinephrine (1.70± 0.86 ng/ml), and epinephrine (1.41± 0.67 ng/ml) levels in plasma of anesthetized sheep, RDN did not lead to any appreciable change in catecholamines immediately after procedure and also after 48 hours. Compared to the intact kidney, norepinephrine levels in the post-RDN kidney tended to be slightly higher (NS) in the RDN-treated kidney after 48 hours (Symplicity Flex 10.7 ± 3.6 vs. 5.8 ± 2.8 g/g tissue; EnligHTN Basket 15.9 ± 4.6 vs. 8.6 ± 2.2 g/g tissue; respectively). A similar trend was seen in epinephrine levels (Symplicity Flex 14.8 ± 6.7 vs. 7.1 ± 5.2 g/g tissue; EnligHTN Basket 17.6 ± 5.1 vs. 10.0 ± 2.1 g/g tissue; respectively).

Discussion:

In order to extend the knowledge obtained in earlier pre-clinical studies (Booth *et al.* 2015, Sakakura *et al.* 2015, Gan *et al.* 2015, Mahfoud *et al.* 2016), we aimed to examine the effects of the single-point and multi-point ablation catheters at 48 hours post-RDN procedure. This early phase post-RDN has not yet been investigated. We confirmed that there was no noticeable alteration within the renal vascular bed (e.g. due to renal artery stenosis or occlusion by angiography), similarly so in the case of post-RDN and control kidneys. Furthermore, histological evaluation of the kidney and suprarenal gland tissue morphology did not reveal any significant changes in the parenchyma, such as ischemia or necrosis. Thus, **our first conclusion** is that in the sheep model neither RDN variant causes noticeable vascular complications, at least not within the first 48 hours.

Another focus in this study was histopathological and immunohistochemical evaluation of the possible acute intravascular, vascular and peri-vascular changes induced by exposure to radio-frequency energy, in comparison with the features of the renal artery and nerves of the contralateral kidney. The main finding was that the RDN procedure by multi-point ablation catheter led to significantly higher occurrence of vascular and peri-vascular damage, most likely due to superior efficacy of this procedure. Nevertheless, neither of the RDN systems achieved complete damage of the targeted renal nervous plexuses or significantly reduced the level of catecholamines in the post-RDN kidney within 48 hours. Thus **our second conclusion** is that RDN procedures caused renal nerve damage that was only incomplete, most likely due to anatomical variability of the renal artery wall, and of the variable peri-arterial renal nerve distribution in the sheep.

Although we are aware of gross anatomical and morphological differences between the relevant structures in the sheep and humans, the sheep model studies appear to be of

clinical relevance. Besides different anatomical localization of the left kidney in sheep, we also noticed differences in the thickness of tunica media of the renal artery. Histomorphometric analysis has shown that the thickness of renal artery in human is significantly related to age, and both the intima and media undergo age-related hyperplasia (Reddy *et al.* 2011). Another issue is that in humans the peri-arterial renal nerve distribution with respect to density, size, and distance from renal artery lumen varies along the renal artery length (Sakakura *et al.* 2014). We observed that in the sheep the distance of peri-arterial renal nerve from renal artery lumen varied from 1 to 3 mm. Overall, such individual variabilities may obviously affect the efficiency of RDN procedure to target renal innervation, and this study provides additional evidence that the extent of nerve structure damage during RDN depends on the distance from the ablation site. This observation may help explain the limited antihypertensive effects of RDN and possibly may also be relevant to the process of the subsequent progressive renal nerve regeneration and reinnervation of the kidneys (Booth *et al.* 2015, Sakakura *et al.* 2015).

A comparison of the morphologic effects of using single-point and multi-point ablation catheters strongly suggests that increasing the number of ablation sites increases the probability to induce damage to renal nerves (Tzafriri *et al.* 2014, Tsioufis *et al.* 2015, Rosa *et al.* 2016). Admittedly, the evidence on the long-lasting superior effects of multi-electrode RDN system still remains limited (Tsioufis *et al.* 2015, Rosa *et al.* 2016). Moreover, optical coherence tomography studies performed directly after the RDN procedure have shown that compared to the Simplicity RDN, the multi-electrode variant may increase the occurrence of thrombus formation (Templin *et al.* 2013). Unfortunately, although this method can precisely depict the vascular response to RDN procedure, it does not allow assessing the renal nerve damage and thus predict the denervation effectiveness. In the present study, the anatomical

variability of the distribution of renal nerves in the sheep did not allow to achieve a complete or major disruption of the renal nerve bundle. Therefore it can be assumed that the effectiveness of any RDN system is highly influenced by the specific anatomical distribution of renal nerves and also by tissue conductivity determining energy transition from the ablation site to the peri-arterial nerve plexus (Sakakura *et al.* 2014). Furthermore, the nervous plexuses surrounding the renal artery have a considerable anatomical inter-individual variability in terms of a different number of nerves, different spatial distribution of their branching and anastomoses, and a variable distance from the renal artery (Reddy *et al.* 2011). Therefore, histological scoring systems seem most suitable for assessing the impact of renal denervation (Tzafriri *et al.* 2014). Our modified scoring system used in this study was focused on detailed evaluation of the variable microscopic changes of renal artery wall and the nerve microstructure following acute denervation. Although we observed that the multi-point ablation procedure resulted in a greater damage to renal nerves compared to the single-point ablation, our histologic analysis of renal nerves plexuses indicated still incomplete RDN effectiveness of both systems.

Numerous studies confirmed the value of renal tissue norepinephrine level as an index of RDN effectiveness (Krum *et al.* 2009, Cohen-Mazor *et al.* 2014, Booth *et al.* 2015). Renal denervation has also been shown to reduce whole-body norepinephrine spillover dependent on reduced sympathetic nerve signaling. However, the relationship between norepinephrine levels and the degree of renal nerve damage has never been established. Our results confirm that renal catecholamine content is not an early sensitive marker of the efficiency of RDN procedure, at least not within the first 48 hours. Moreover, one should be aware that catecholamine levels must also be affected by anaesthesia and the stress underlying preparatory surgery and the denervation procedure. It seems that an appreciable response of

renal norepinephrine content cannot be observed until after one week after denervation (Krum *et al.* 2009, Booth *et al.* 2015). This suggests that alterations in the renal nerves after RDN procedure can progress over days or weeks. Further studies are still required to provide adequate knowledge of this issue.

An obvious limitation of this study was that experiments were performed in normotensive animals with unaltered basal renal sympathetic activity. This could be expected to reduce the catecholamine level response to RDN in our sheep. Secondly, the very design of the study implied observation of the earliest morphologic alterations in renal artery wall and renal nerves in response to RDN; these results do not throw light on the expected further progression of vascular and peri-vascular changes, including the development of local fibrosis, or on the extent of functional responses to altered renal sympathetic activity. Another limitation is that histological processing of the tissue samples could have caused endothelial damage, therefore the value of the scoring of intra-vascular changes could be described as uncertain.

In conclusion, the effectiveness of the two catheter-based RDN systems approved for the clinical use seems largely dependent on anatomical interindividual variability of renal artery wall and adjacent renal nerves. Both systems tested in the present study provided only incomplete renal nerve ablation in the sheep. This observation indicates that the extensive variability of renal nerve plexuses and renal artery wall structure may limit the wide-range use of RDN procedure in patients with resistant hypertension.

Conflict of Interest:

The authors have no conflict of interest

References:

BHATT DL, KANDZARI DE, O'NEILL WW, D'AGOSTINO R, FLACK JM, KATZEN BT, LEON MB, LIU M, MAURI L, NEGOITA M, COHEN SA, OPARIL S, ROCHA-SINGH K, TOWNSEND RR, BAKRIS GL; SYMPLICITY HTN-3 INVESTIGATORS. A controlled trial of renal denervation for resistant hypertension. *N Engl J Med* **370**: 1393-1401, 2014.

BOOTH LC, NISHI EE, YAO ST, RAMCHANDRA R, LAMBERT GW, SCHLAICH MP, MAY CN. Reinnervation of renal afferent and efferent nerves at 5.5 and 11 months after catheter-based radiofrequency renal denervation in sheep. *Hypertension* **65**: 393-400, 2015.

COHEN-MAZOR M, MATHUR P, STANLEY JR, MENDELSOHN FO, LEE H, BAIRD R, ZANI BG, MARKHAM PM, ROCHA-SINGH K. Evaluation of renal nerve morphological changes and norepinephrine levels following treatment with novel bipolar radiofrequency delivery systems in a porcine model. *J Hypertens* **32**: 1678–1691, 2014.

DIBONA GF. Nervous kidney: interaction between renal sympathetic nerves and the renin-angiotensin system in the control of renal function. *Hypertension* 2000;36:1083–1088.

GAN Q, QU XK, GONG KZ, GUAN SF, HAN WZ, DAI JJ, LI RG, ZHANG M, LIU H, XU YJ, ZHANG YJ, FANG WY. Efficacy and safety of a novel multi-electrode radiofrequency ablation catheter for renal sympathetic denervation in pig. *J Geriatr Cardiol* **12**: 618–625, 2015.

HENEGAR JR, ZHANG Y, RAMA RD, HATA C, HALL ME, HALL JE. Catheterbased radiorefrequency renal denervation lowers blood pressure in obese hypertensive dogs. *Am J Hypertens* **27**: 1285–1292, 2014.

JOHNS EJ, KOPP UC, DIBONA GF. Neural control of renal function. *Compr Physiol* **1**: 731-767, 2011.

KRUM H, SCHLAICH M, WHITBOURN R, SOBOTKA PA, SADOWSKI J, BARTUS K, KAPELAK B, WALTON A, SIEVERT H, THAMBAR S, ABRAHAM WT, ESLER M. Catheter-based renal sympathetic denervation for resistant hypertension: a multicentre safety and proof-of-principle cohort study. *Lancet* **373**: 1275-1281, 2009.

MAHFOUD F, LÜSCHER TF, ANDERSSON B, BAUMGARTNER I, CIFKOVA R, DIMARIO C, DOEVENDANS P, FAGARD R, FAJADET J, KOMAJDA M, LEFÈVRE T, LOTAN C, SIEVERT H, VOLPE M, WIDIMSKY P, WIJNS W, WILLIAMS B, WINDECKER S, WITKOWSKI A, ZELLER T, BÖHM M; EUROPEAN SOCIETY OF CARDIOLOGY. Expert consensus document from the European Society of Cardiology on catheter-based renal denervation. *Eur Heart J* **34**: 2149-2157, 2013.

MAHFOUD F, MOON LB, PIPENHAGEN CA, JENSEN JA, PATHAK A, PAPADEMETRIOU V, EWEN S, LINZ D, BÖHM M. Catheter-based radio-frequency renal nerve denervation lowers blood pressure in obese hypertensive swine model. *J Hypertens* **34**: 1854-1862, 2016.

REDDY S, KUMAR P, PRASAD K. Histomorphometric and sympathetic innervation of the human renal artery: A cadaveric study. *Urol Ann* **3**: 141-146, 2011.

RIPPY MK, ZARINS D, BARMAN NC, WU A, DUNCAN KL, ZARINS CK. Catheter-based renal sympathetic denervation: chronic preclinical evidence for renal artery safety. *Clin Res Cardiol* **100**: 1095-1101, 2011.

ROSA J, WIDIMSKÝ P, WALDAUF P, LAMBERT L, ZELINKA T, TÁBORSKÝ M, BRANNY M, TOUŠEK P, PETRÁK O, ČURILA K, BEDNÁŘ F, HOLAJ R, ŠTRAUCH B, VÁCLAVÍK J, NYKL I, KRÁTKÁ Z, KOCIÁNOVÁ E, JIRAVSKÝ O, RAPPOVÁ G, INDRA T, WIDIMSKÝ J JR. Role of Adding Spironolactone and Renal Denervation in True Resistant Hypertension: One-Year Outcomes of Randomized PRAGUE-15 Study. *Hypertension* **67**: 397-403, 2016.

SAKAKURA K, LADICH E, CHENG Q, OTSUKA F, YAHAGI K, FOWLER DR, KOLODGIE FD, VIRMANI R, JONER M. Anatomic assessment of sympathetic peri-arterial renal nerves in man. *J Am Coll Cardiol* **64**: 635-643, 2014.

SAKAKURA K, TUNEV S, YAHAGI K, O'BRIEN AJ, LADICH E, KOLODGIE FD, MELDER RJ, JONER M, VIRMANI R. Comparison of histopathologic analysis following renal sympathetic denervation over multiple time points. *Circ Cardiovasc Interv* **8**: e001813, 2015.

TEMPLIN C, JAGUSZEWSKI M, GHADRI JR, SUDANO I, GAEHWILER R, HELLERMANN JP, SCHOENENBERGER-BERZINS R, LANDMESSER U, ERNE P, NOLL G, LÜSCHER TF. Vascular lesions induced by renal nerve ablation as assessed by optical coherence tomography: pre- and post-procedural comparison with the Simplicity catheter system and the EnligHTN multi-electrode renal denervation catheter. *Eur Heart J* **34**:2141-2148, 2013.

TSIOUFIS C, KORDALIS A, FLESSAS D, ANASTASOPOULOS I, TSIACHRIS D, PAPADEMETRIOU V, STEFANADIS C. Pathophysiology of resistant hypertension: the role of sympathetic nervous system. *Int J Hypertens* **2011**: 642416, 2011.

TSIOUFIS CP, PAPADEMETRIOU V, DIMITRIADIS KS, KASIAKOGIAS A, TSIACHRIS D, WORTHLEY MI, SINHAL AR, CHEW DP, MEREDITH IT, MALAIAPAN Y, THOMOPOULOS C, KALLIKAZAROS I, TOUSOULIS D, WORTHLEY SG. Catheter-based renal denervation for resistant hypertension: Twenty-four month results of the EnligHTN I first-in-human study using a multi-electrode ablation system. *Int J Cardiol* **201**: 345-350, 2015.

TZAFRIRI AR, MAHFOUD F, KEATING JH, MARKHAM PM, SPOGNARDI A, WONG G, FUIMAONO K, BÖHM M, EDELMAN ER. Innervation patterns may limit response to endovascular renal denervation. *J Am Coll Cardiol* **64**: 1079-1087, 2014.

WORTHLEY SG, TSIOUFIS CP, WORTHLEY MI, SINHAL A, CHEW DP, MEREDITH IT, MALAIAPAN Y, PAPADEMETRIOU V. Safety and efficacy of a multi-electrode renal sympathetic denervation system in resistant hypertension: the EnligHTN I trial. *Eur Heart J* **34**: 2132-2140, 2013.

Legend:

Figure 1. Histological assessment of the RDN-induced injury of the renal artery in transverse histological sections, arranged using a semiquantitative scale

A – No histological signs of injury of either artery or nerves (black arrow). **B** – Eccentric focal damage and weakening of the wall (blue arrow). **C** – Collagen denaturation in three quadrants (yellow arrows). An intraluminal thrombus is visible. **D** – Damaged elastic membranes within the tunica media layer (black arrow). **E** – Loss of immunopositivity for alpha-smooth muscle actin in two quadrants (red arrows). **F** – Dilated or obliterated vasa vasorum in the adventitia of the artery (magenta arrow) close to the nerves.

Verhoeff's hematoxylin and green trichrome staining (A, C), hematoxylin-eosin staining (B), orcein staining (D, elastin stained dark brown), immunohistochemical detection of alpha-smooth muscle actin in vascular smooth muscle (E, dark brown positivity), immunohistochemical detection of von-Willebrand factor in endothelial cells (F, dark brown positivity). Scale bar 500 µm (A-C, E), 100 µm (D) and 200 µm (F).

Figure 2. Histological assessment of the RDN-induced injury of the nerves accompanying the renal artery in transverse histological sections, arranged using a semiquantitative scale.

A – No histological signs of nerve injury (black arrow). **B** – Hyperemia of the nerve with dilated vasa nervorum (red arrow). **C** – Destructive fragmentation and complete loss of nuclei of Schwann glia cells (blue arrow). **D** – Loss of the fine structure of endoneurium connective tissue between the nerve fibres (yellow arrow). **E** – Moderate loss (red arrow) or complete loss (red arrowhead) of immunopositivity for neurofilament protein. **F** – Loss of

immunopositivity for tyrosinehydroxylase (magenta arrow). Immunohistochemical detection of neurofilament protein (A, E, dark brown positivity).

Verhoeff's hematoxylin and green trichrome staining (B), hematoxylin-eosin staining (C), Mallory trichrome staining (D), immunohistochemical detection of tyrosine-hydroxylase (F, dark brown positivity). Scale bar 500 µm (A) and 200 µm (B-F).

Figure 3. Comparison of the the RDN-induced renal artery (A) and renal nerve (B) injury scores for single-point and multiple-ablation catheters.

A – the sum, the maximum and the mean injury to the renal artery treated with the Symplicity Flex catheter or EnligHTN catheter. **B** – the sum, the maximum and the mean injury to the renal nerve treated with the Symplicity Flex catheter or EnligHTN catheter. Data are displayed as the mean ± SEM, differences significant at *p<0.05.

Figure 4. Examples of histological signs of arterial injury in the animals after intervention using the Symplicity Flex catheter (left) or EnligHTN catheter (right).

In the renal arteries treated with the Symplicity catheter, the lesions of vascular wall were less extensive, often affecting only one quadrant of the vascular section (A, B, arrrows). The accompanying nerves were often normal (A, B, arrowheads). Occasionally, the weakening of the wall and collagen denaturation with smooth muscle loss was (C, arrow) was accompanied by adjacent oedema of the tunica media layer (C, arrowheads). In one animal, more quadrants were affected (D). In the arteries treated with the EnligHTN catheter, the vascular lesions were more extensive, often affecting multiple quadrants in the cross sections of several segments (E-H, arrows in E, H).

Verhoeff's iron hematoxylin and green trichrome stain (A, B, E-F), Mallory trichrome (C), immunohistochemical detection of alpha-smooth muscle actin (G-H, dark brown positivity). Scale bar 500 µm (A-H).

Figure 5. Examples of histological signs of nerves damage in the animals after intervention using the Symplicity Flex catheter (left) and EnligHTN catheter (right).

In many sections, adjacent to the renal artery, morphologically and immunohistochemically normal nerves were found (A, E, red arrows). In both groups of animals, hyperemia of nerves without further damage to the nerve microstructure (B, F) was commonly seen. Despite complete immunohistochemical negativity (not shown here, see Figure 2), some nerve bundles were partially damaged, showing focal loss of immunopositivity for neurofilament protein (C) or tyrosine hydroxylase (D, H). In some nerve bundles, the vasa nervorum microvessels (G, black arrow) were either dilated or destroyed.

Immunohistochemical detection of neurofilament protein (A, C, E, dark brown positivity), immunohistochemical detection of tyrosine-hydroxylase (D, H, dark brown positivity), Verhoeff's hematoxylin and green trichrome (B,F). Scale bar 500 µm (A,E), 200 µm (B-D, F) and 100 µm.

Figure 6. Histological findings illustrating normal appearance of the kidneys and the suprarenal glands after intervention using the Symplicity Flex catheter (left) and EnligHTN catheter (right).

Both kidney cortex (A, E) and medulla (B, F) showed no damage, necrosis, or inflammatory infiltration. In both groups of animals, nerves positive for immunohistochemical detection of neurofilament protein (C) and tyrosin hydroxylase (G) were found. The medulla of the suprarenal glands was positive for tyrosine-hydroxylase in both groups (D, H). Hematoxylin-

eosin (A, B, E, F), immunohistochemical detection of neurofilament protein (C, dark brown positivity), immunohistochemical detection of tyrosine-hydroxylase (G-H, dark brown positivity). Scale bar 500 μm (A,E) and 200 μm (B-D, F-H).

Table 1: Semiquantitative scale for assessing the injury of the renal artery and adjacent nerves in transverse histological sections. Points (1-4) were allocated per each arterial quadrant showing an injury of the artery or nerves in the segment under study. See Figures 1-2 for illustration of typical histological findings.

Injury assessment of the post-RDN renal artery

Points per each arterial segment	Histological injury found in renal artery
0	no histological signs of injury
1,2,3,4	eccentric focal damage and weakening of the wall
1,2,3,4	collagen denaturation
1,2,3,4	damaged elastic membranes
1,2,3,4	loss of immunopositivity for alpha-smooth muscle actin
1,2,3,4	damage to the vasa vasorum
1	presence of intraluminal thrombus

Injury assessment of the post-RDN peripheral nerves accompanying the renal artery

Points per each nerve segment	Histological injury found in nerves surrounding the renal artery
0	no histological signs of injury
1,2,3,4	hyperemia of nerve
1,2,3,4	destructive fragmentation or complete loss of nuclei of Schwann cells
1,2,3,4	damage to the inner nerve structure: loss of neurilemma and structure of the endoneurial connective tissue
1,2,3,4	loss of immunopositivity for neurofilament protein
1,2,3,4	loss of immunopositivity for tyrosine hydroxylase

Table 2: Parameters calculated from the semiquantitative scoring systems.

Parameter	Definition
Sum of the vascular injury score and sum of the nerve injury score per animal	Calculated by summing up the points scored along all the 3 mm-long segments of the renal artery (typically 8 segments). This was done for the vascular injury and the nerve injury separately.
Maximum vascular injury score and maximum nerve injury score	The maximum value found among the segments under study in the given animal and organ.
Mean vascular/nerve injury score per segment	Arithmetic mean value of the score results per one segment, calculated by dividing the sum of the vascular injury score, or the sum of the nerve injury score, respectively, by the number of arterial segments in the given animal and organ.

Figure 1
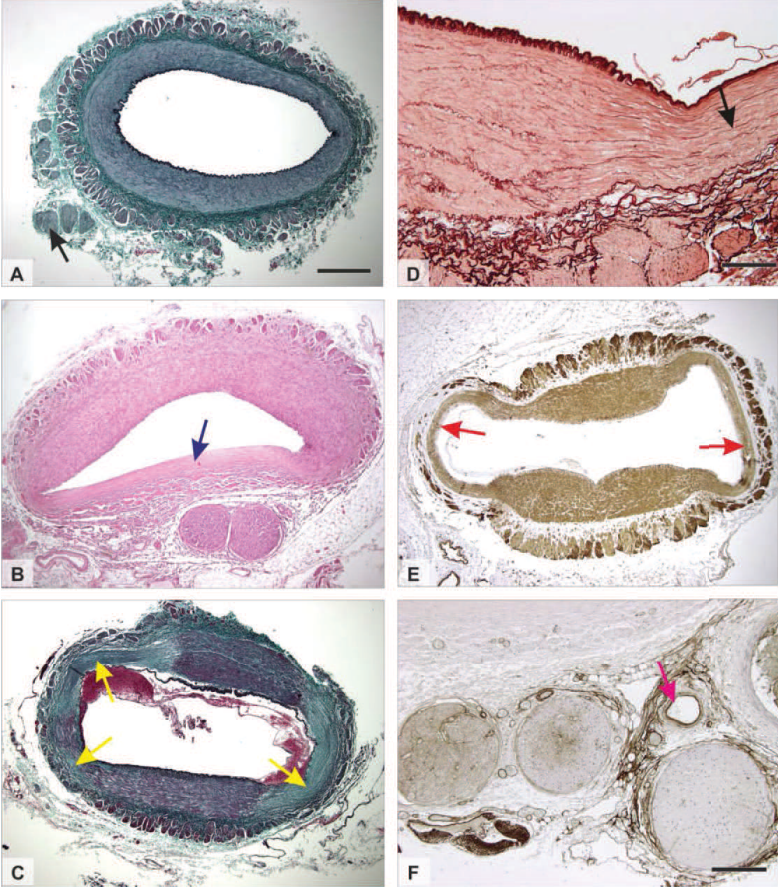
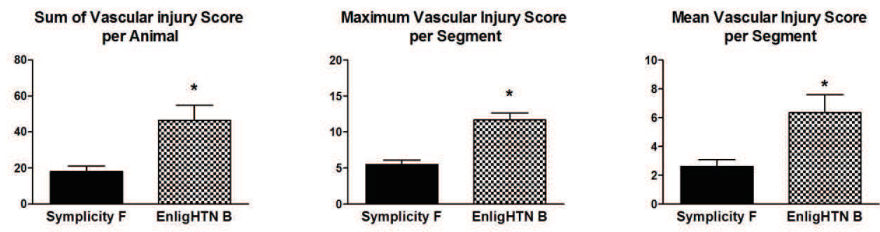**Figure 2**
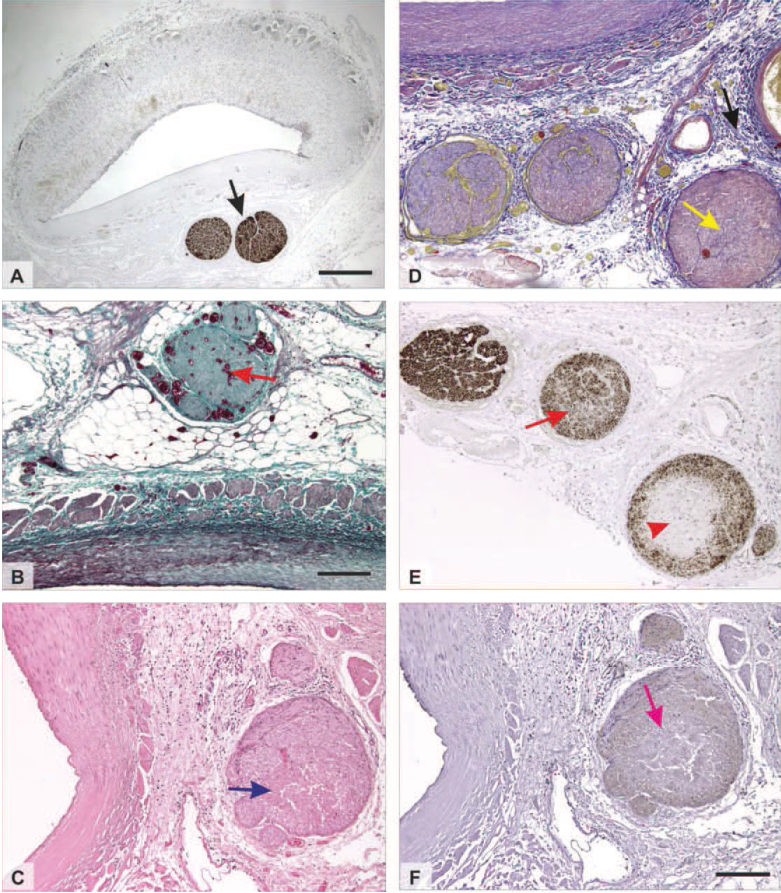
Figure 3

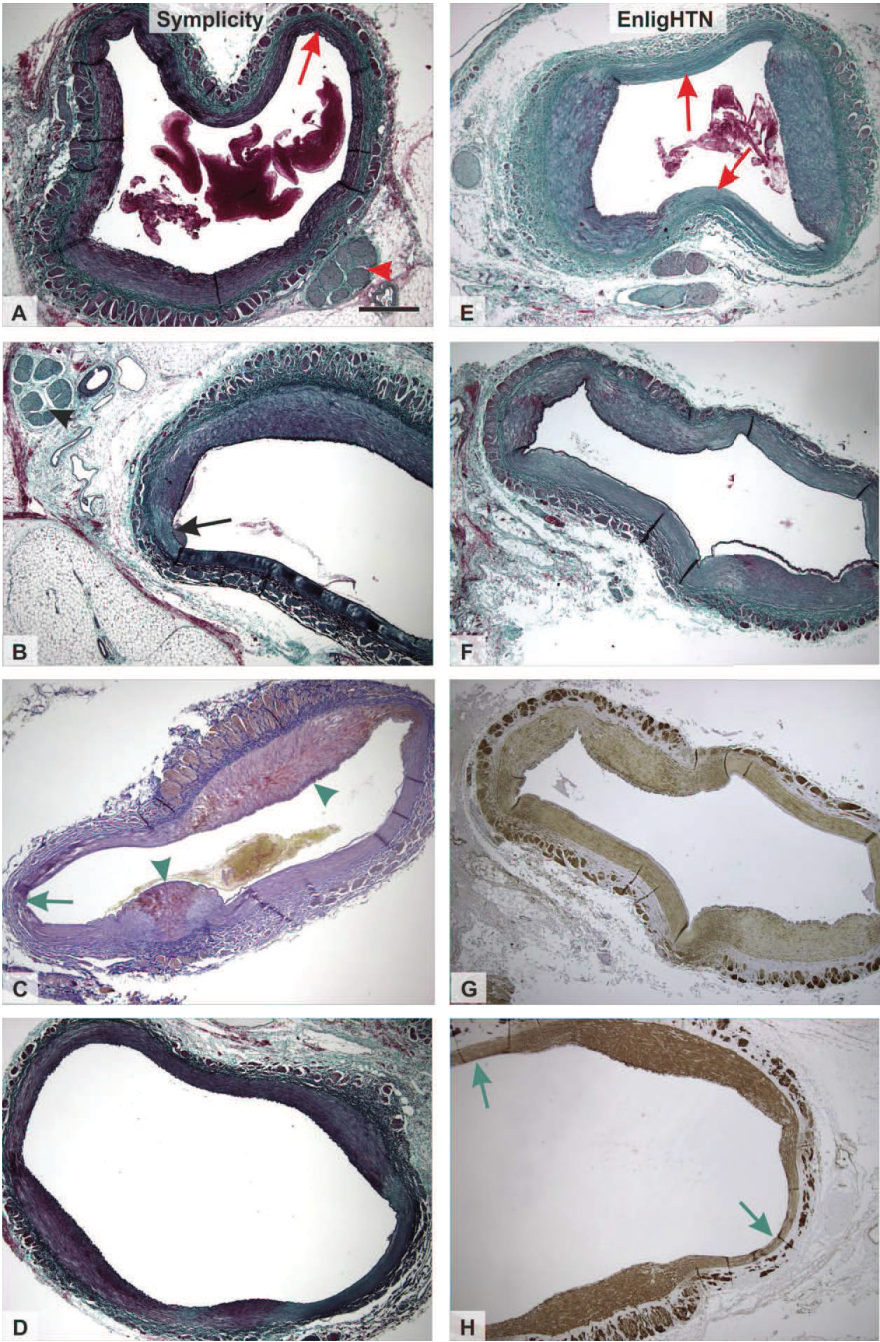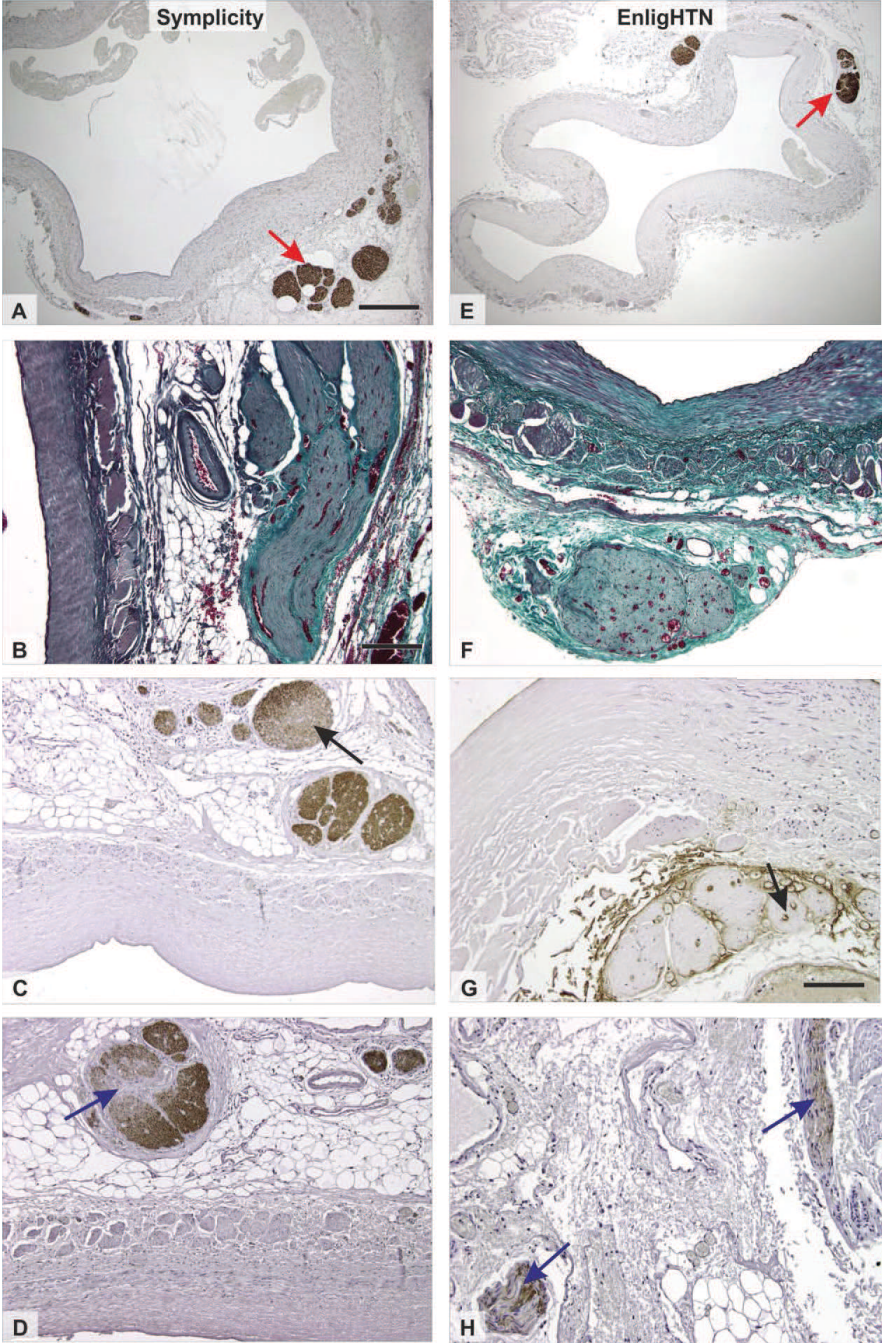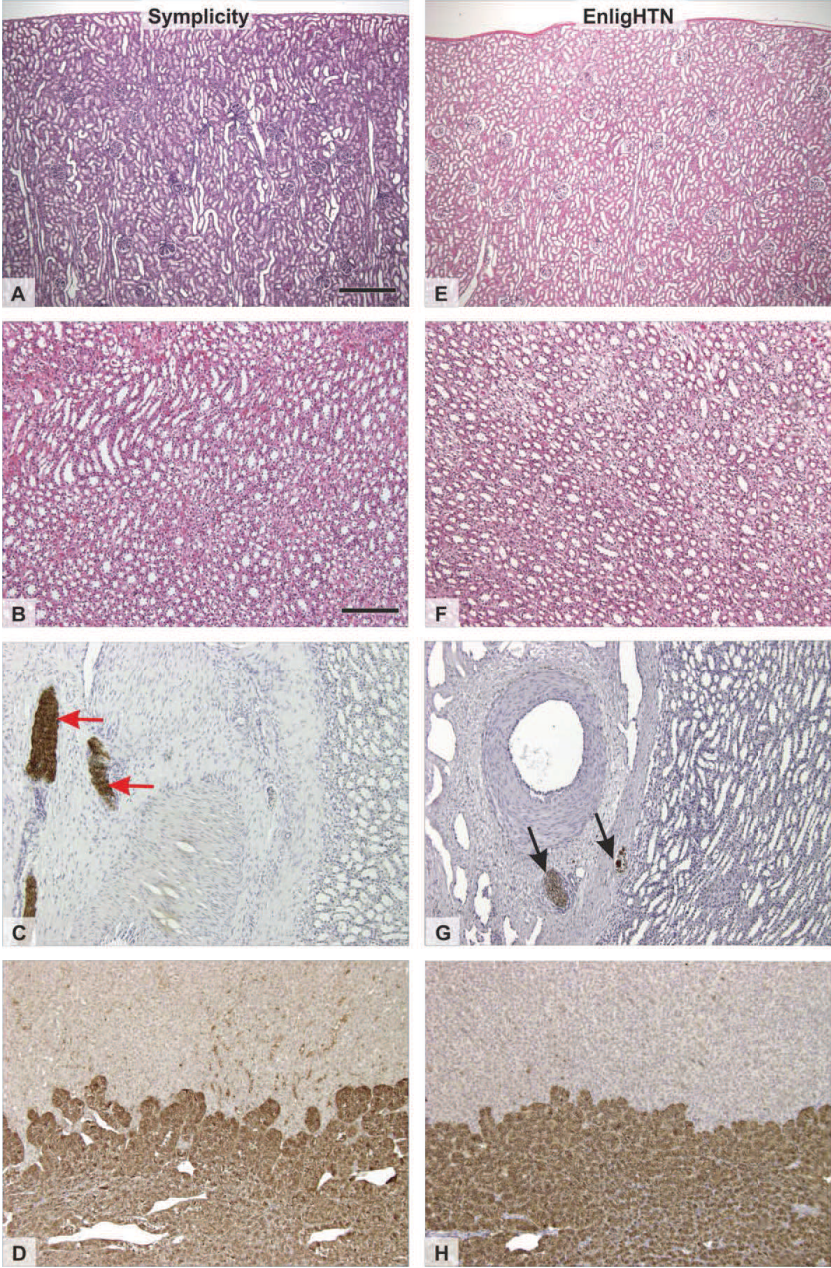**A**

B
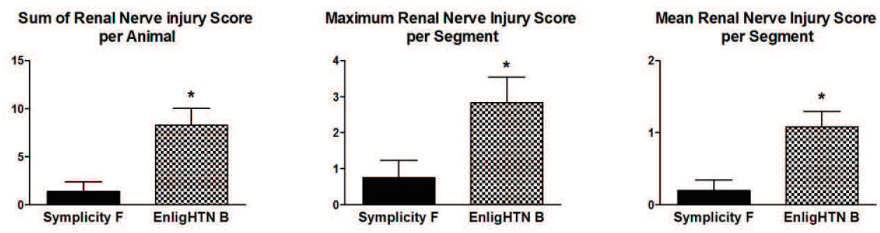
Figure 4

Figure 5

Figure 6

Příloha IV:

KUBIKOVA, T., KOCHOVA, P., FIALA, R., SPATENKA, J., BURKERT, J., KRALICKOVA, M., TONAR, Z. Histological Composition and Mechanical Properties of Cryopreserved Samples of Aortic and Pulmonary Valves. Solid State Phenomena 2017; 341-344.

Histological Composition and Mechanical Properties of Cryopreserved Samples of Aortic and Pulmonary Valves

Tereza Kubíková[1,a], Petra Kochová[2,b], Radovan Fiala[3,c],
Jaroslav Špatenka[3,4,d], Jan Burkert[3,4,e], Milena Králíčková[1,f], Zbyněk Tonar[2,g]

[1]Department of Histology and Embryology and Biomedical Centre, Faculty of Medicine in Pilsen, Charles University in Prague, Karlovarská 48, 301 00, Pilsen, Czech Republic

[2]European Centre of Excellence NTIS, Faculty of Applied Sciences, University of West Bohemia in Pilsen, Univerzitní 8, 306 14, Pilsen, Czech Republic

[3]Department of Cardiothoracic Surgery, 2nd Faculty of Medicine, Charles University in Prague, V Úvalu 84, 150 06, Prague, Czech Republic

[4]Department of Transplantation and Tissue Banking, University Hospital Motol, V Úvalu 84, 150 06, Prague, Czech Republic

[a]tereza.kubikova@lfp.cuni.cz, [b]kochovap@ntc.zcu.cz, [c]radovan.fiala@fnmotol.cz, [d]jaroslav.spatenka@fnmotol.cz, [e]jan.burkert@fnmotol.cz, [f]milena.kralickova@lfp.cuni.cz, [g]tonar@ntc.zcu.cz

Abstract. Human cryopreserved allografts of pulmonary and aortic valves are routinely used as total valve replacement. For successful surgery it is needed to sufficiently preserve biomechanical properties and histological structures of allografts. However, it is not known how the mechanical properties of these allografts relate to their histological composition. The aim of our study was to compare the histological composition and mechanical properties of the valves. From allografts we prepared 2 valve cusps and samples of aorta or pulmonary trunk. In a previous study we had measured following parameters: ultimate stress, ultimate strain, Young's moduli of elasticity, intima-media thickness, wall thickness, area fraction of elastin and area fraction of collagen in the whole wall. We found weak positive correlation between ultimate stress and Young's modulus in small and large deformation with wall thickness in the valve cusps. In the arteries we found positive correlation between Young's modulus in large deformation with intima-media thickness and ultimate strain with intima-media thickness and area fraction of collagen, and negative correlation between ultimate strain with area fraction of elastin. In our study we quantified also the other components of wall with mechanical significance, such as the fraction of smooth muscle cells and chondroitin sulfate, which belong to glycosaminoglycans. We did not find correlation between these components and mechanical properties of these valves. Therefore, it is recommended to perform both mechanical and histological analysis to further characterize cryopreserved allografts.

Introduction

Human cryopreserved allografts of pulmonary and aortic heart valves and the roots of these major elastic arteries are routinely used for valve replacement. Together with surgical technique, biomechanical sufficiency and preservation of the histological structures of the grafts are considered to be necessary for a proper outcome for reconstructive surgery [1].

The aortic and pulmonary valves prevent the reversal of blood flow to the heart ventricles in diastole. Valve function normally relies on 3 cusps, as well as the annular dense collagenous connective tissue and the arterial root geometry. The cusps have similar semilunar shapes. The valves are primarily composed of endothelium and connective tissue cells and extracellular matrix components of connective tissue. The main constituents of the connective tissue are collagen fibrils, elastic fibres and proteoglycans, such as chondroitin sulfate (CS) [2].

Elastic arteries such aortic root and pulmonary trunk receive blood flow directly from the heart ventricles in systole. Elastic arteries consist of three layers as follows: (i) The tunica intima, which

is composed of the vascular endothelium and a subendothelial layer; (ii) the tunica media, which is the thickest layer, which contains concentrically elastic fenestrated membranes and smooth muscle cells; (iii) the tunica adventitia, which is the most abluminal layer of the elastic arteries. It is composed of elastic and collagenous fibres that are interspersed with connective tissue cells, blood vessels (the vasa vasorum) and nerve fibres (the nervi vasorum).

The microstructure and the mechanics of the mitral valve have been thoroughly studied [3,4], but similar results for cryopreserved aortic and pulmonary valves are lacking in the literature.

Our hypotheses were as follows:

H_A: There is no difference between the area fraction of smooth muscle actin in wall *(A_A(SMA, wall)* of aortas and *A_A(SMA, wall)* of pulmonary trunks; there is no difference between the area fraction of chondroitin sulfate in wall *(A_A(CS, wall)* of aortas and *A_A(CS, wall)* of pulmonary trunks; there is no difference between *A_A(CS, wall)* of cusps of aortic valves and *A_A(CS, wall)* of cusps of pulmonary valves.

H_B: There is no correlation between *A_A(SMA, wall)* or *A_A(CS, wall)* and the mechanical properties of the aortas and the pulmonary trunks; there is no correlation between *A_A(CS, wall)* and mechanical properties of the aortic and the pulmonary cusps.

Materials and methods

Samples for our study were obtained from Heart Valve Bank of the Department of Transplantation and Tissue Banking, University Hospital Motol, Czech Republic after their expiration (five years). The allograft heart valves are cryopreserved at -196 °C according to the established protocol [5]. We prepared eight rings of aortas, eight rings of pulmonary trunks, twelve cusps from aortic valves and twelve cusps from pulmonary valves.

Mechanical loading
All specimens were 5 mm wide. The 5 mm wide circumferential strips of the cups were loaded at room temperature by a uniaxial tensile test using a Zwick/Roell Z50 traction machine equipped with a 1-kN load cell to obtain the mechanical parameters, namely Young's moduli of elasticity, ultimate stress and ultimate strain. Uniaxial ring test was used for measuring mechanical properties of elastic arteries. The Young's moduli of elasticity were determined in the linear regions of the stress-strain curve, namely in the small deformation region and in the large deformation region, using linear regression. The strains were approximately 0-20% and 40-60% for elastic arteries (0-10% and 8-60% for cusps) for the two regions, respectively, depending on the shape of the curve. The ultimate stresses and the ultimate strains were determined at the start of the rupture. The stress was defined as force divided by initial area. The strain was defined as the actual circumference change divided by its initial circumference for elastic arteries, respectively, as the elongation of the specimen divided by its initial length for cusps. Our own software – Elfpy [6], was used for the evaluation.

Histological analysis
Tissue samples were fixed with 4% buffered formalin and embedded in paraffin blocks. In each sample, two 5-µm-thick histological sections of elastic arteries were processed immunohistochemically in order to reveal the presence of smooth muscle actin (SMA) and two sections of elastic arteries or cusps of valves were processed immunohistochemically in order to reveal the presence of CS. Antibodies and protocols used for immunohistochemistry are in Table 1.

Table 1. Antibodies, their dilution, technique of pretreatment and detection of immunoreactions used for immunohistochemistry.

Antibody	Dilution	Pretreatment	Detection of immunoreaction
Monoclonal Mouse Anti-Actin (Smooth Muscle) Antibody Clone 1A4 (M0851, Dako, Glostrup, Denmark)	1:200	20 minutes with Target pretreatment (Dako, Glostrup, Denmark) at 96°C	Immununoperoxidase technique by N-Histofine (Nichirei Biosciences, Tokyo, Japan) vizualitation reaction by diaminobenzidine (Dako, Glostrup, Denmark)
Monoclonal Mouse Anti-Chondroitin Sulfate Antibody Clone CS-56 (C8035, Sigma Aldrich, Missouri, USA)	1:500	5 minutes with Proteinase K (Dako, Glostrup, Denmark)	Immunofluorescence technique by secondary antibody Goat Anti-Mouse IgG H&L (Alexa Fluor® 488) (ab150117, Abcam, Cambridge, UK)

Eight microphotographs were taken from each sample and each method. The area fraction of SMA and CS were evaluated using a stereological grid point [7]. All quantitative estimates were calculated using well established stereological methods [7] and Ellipse software (ViDiTo, Košice, Slovakia). The data were processed using STATISTICA 10 (StatSoft, Inc., Tulsa, OK, USA). The results had normal distribution. The t-test was used when comparing samples.

Results

We did not find significant difference between $A_A(SMA, wall)$ of aortas and $A_A(SMA, wall)$ of pulmonary trunks. No significant difference was found between $A_A(CS, wall)$ of aortas and $A_A(CS, wall)$ of pulmonary trunks. Histological comparison of elastic arteries is in Figure 1A-D. We did not find correlation between mechanical properties and histological composition in aortas or pulmonary trunks.

We did not find significant difference between $A_A(CS, wall)$ of cusps of aortic valves and $A_A(CS, wall)$ of cusps of pulmonary valves. Histological comparison of cusps is in Figure 1E-F. We did not find correlation between mechanical properties and histological composition in cusps of aortic or pulmonary valves.
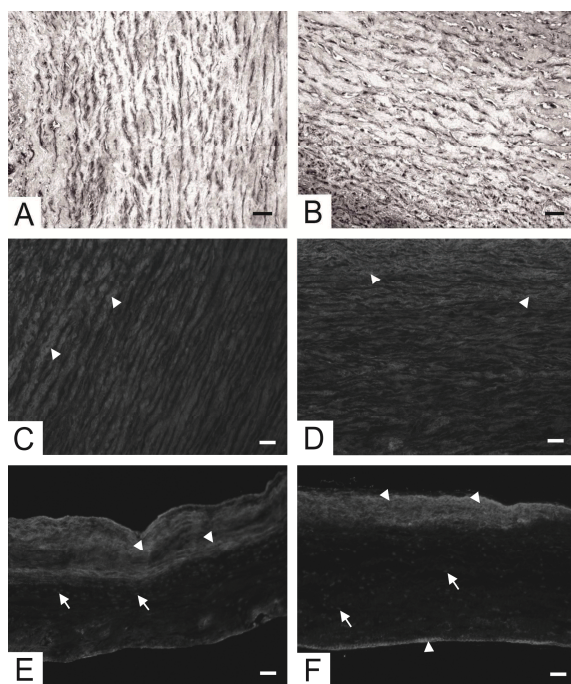
Summary

Histological composition of aortic and pulmonary valves did not correlate with their mechanical properties. Therefore, characterization of these allografts during cryopreservation requires both histological assessment as well as mechanical tests.

Fig. 1 Comparison of aortic and pulmonary valves components using immunochemical reaction. **A** Smooth muscle cells contain smooth muscle actin (dark objects in wall of aorta; **B** smooth muscle cells (dark objects) in wall of pulmonary trunk; **C** chondroitin sulfate (white arrowheads) in wall of aortas; **D** chondroitin sulfate (white arrowheads) in wall of pulmonary trunk; **E** chondroitin sulfate (white arrowheads) in wall of cusps of aortic valves; **F** chondroitin sulfate (white arrowheads) in wall of cusps of pulmonary valves; nuclei of cells (white arrows), scale 50 μm.

References

[1]   B. Arabkhani, A. Mookhoek, I. Di Centa, E. Lansac, J.A. Bekkers, R. De Lind Van Wijngaarden, A.J.J.C. Bogers, J.J.M. Takkenberg: Reported Outcome After Valve-Sparing Aortic Root Replacement for Aortic Root Aneurysm: A Systematic Review and Meta-Analysis, Ann. Thorac. Surg. Vol. 100 (2015), p. 1126–1131.

[2]   R.A. Hopkins: Cardiac reconstructions with allograft tissues, Springer-Verlag, New York (2005).

[3]   V. Prot, B. Skallerud, G. Sommer, G.A. Holzapfel: On modelling and analysis of healthy and pathological human mitral valves: two case studies, J. Mech. Behav. Biomed. Mater. Vol. 3 (2010), p. 167–177.

[4]   C.-H. Lee, J.-P. Rabbah, A.P. Yoganathan, R.C. Gorman, J.H. Gorman, M.S. Sacks: On the effects of leaflet microstructure and constitutive model on the closing behavior of the mitral valve, Biomech. Model. Mechanobiol. Vol. 14 (2015), p. 1281–1302.

[5]   J. Spatenka, M. Kostelka, P. Kobylka, B. Hucín, T. Honěk, O. Lochmann, T. Hájek, T. Tláskal, V. Povýsilová, B. Fiser: Preparation, storage, transportation and use of heart valves for allotransplantation, Rozhl. V Chir. Měsíčník Československé Chir. Společnosti. Vol. 76 (1997), p. 118–125.

[6]   E. Prosecká, M. Rampichová, L. Vojtová, D. Tvrdík, S. Melčáková, J. Juhasová, M. Plencner, R. Jakubová, J. Jančář, A. Nečas, P. Kochová, J. Klepáček, Z. Tonar, E. Amler: Optimized conditions for mesenchymal stem cells to differentiate into osteoblasts on a collagen/hydroxyapatite matrix, J. Biomed. Mater. Res. A. Vol. 99 (2011), p. 307–315.

[7]   Z. Tonar, T. Kubíková, C. Prior, E. Demjén, V. Liška, M. Králíčková, K. Witter, Segmental and age differences in the elastin network, collagen, and smooth muscle phenotype in the tunica media of the porcine aorta, Ann. Anat. Anat. Anz. Off. Organ Anat. Ges. Vol. 201 (2015), p. 79–90.

Příloha V:

TONAR, Z., KOCHOVA, P., CIMRMAN, R., PERKTOLD, J., **KUBIKOVA, T.**, DEMJEN, E., LISKA, V., KRALICKOVA, M., WITTER, K. Links between the orientation of vascular smooth muscle and microscopical composition of aortic segments. Solid State Phenomena; 2017; 329-332.

Links between the Orientation of Vascular Smooth Muscle and Microscopical Composition of Aortic Segments

Zbyněk Tonar[1,a], Petra Kochová[2,b], Robert Cimrman[3,c], Josef Perktold[4,d], Tereza Kubíková[1,e], Erna Demjen[5,f], Václav Liška[6,g], Milena Králíčková[1,h] and Kirsti Witter[7,g]

[1]Department of Histology and Embryology and Biomedical Center, Faculty of Medicine in Pilsen, Charles University in Prague, Karlovarská 48, 301 66 Pilsen, Czech Republic

[2]NTIS, European Centre of Excellence, Faculty of Applied Sciences, University of West Bohemia, Univerzitní 8, 306 14 Pilsen, Czech Republic

[3]New Technologies – Research Centre, University of West Bohemia, Univerzitní 8, 306 14 Pilsen, Czech Republic

[4]156 Avenue Willowdale, Outremont, QC H3T1E9, Canada

[5]Department of Biophysics, Institute of Experimental Physics, Slovak Academy of Sciences, Watsonova 47, 043 53 Košice, Slovak Republic

[6]Department of Surgery and Biomedical Center, Faculty of Medicine in Pilsen, Charles University in Prague, Husova 3, 306 05 Pilsen, Czech Republic

[7]Institute of Anatomy, Histology and Embryology, Department of Pathobiology, University of Veterinary Medicine Vienna, Veterinärplatz 1, A-1210 Vienna, Austria

[a]tonar@lfp.cuni.cz, [b]kochovap@ntis.zcu.cz, [c]cimrman3@ntc.zcu.cz, [d]josef.pktd@gmail.com, [e]tereza.kubikova@lfp.cuni.cz. [f]demjen@saske.sk, [g]vena.liska@gmail.com, [f]milena.kralickova@lfp.cuni.cz, [g]Kirsti.Witter@vetmeduni.ac.at

Abstract. We analyzed histological data statistically describing the distribution of orientations of vascular smooth muscle cells (VSMC) within porcine aorta. The data were correlated with the fractions of actin, desmin, vimentin, elastin and collagen within the same samples. In samples with more contractile VSMC and less elastin, the symmetrical helices of VSMC were arranged closely to each other and they were more concentrated than in samples with fewer actin- and desmin-positive VSMC and more elastin. The findings are suitable for microstructurally-motivated biomechanical modeling of porcine aorta under normal conditions.

Introduction

Porcine aorta is frequently used in vascular research as a large-animal model of the human aorta. Most studies deal with pathological conditions, such as abdominal aortic aneurysms [1] and simulations of aneurysm repair or testing repair techniques using endovascular approach. Aorta of pig may develop microscopical lesions similar to human atherosclerotic aorta.

From biomechanical point of view, porcine aorta is an elastic artery [2]. It has three layers: (i) the innermost tunica intima contains the endothelial lining supported by subendothelial connective tissue, (ii) the tunica media consists of vascular smooth muscle cells (VSMC) supported by a network of elastic and collagen fibres and proteoglycans of the ground extracellular matrix, and (iii) the outer tunica adventitia contains dense or loose collagenous connective tissue with nervi vasorum and vasa vasorum. Aortic wall has a nonlinear elasticity [2]. Computer models of aortic wall assume that the VSMC and collagen fibres are arranged as two almost symmetrical helices [3]. This reasonable assumption has been recently confirmed for most segments of the porcine aorta [4]. Another histological analysis [5] showed the volume fractions of elastin, collagen, and VSMC

within the tunica media of collagen in five anatomically defined parts of aorta. Other papers [6] reported biomechanical differences between the proximal and distal aortic segments.

Current microstructure-based models of aortic wall [7] aim to explore mechanisms linking the histology and mechanics so that the biaxial properties of aorta could be predicted from the histological morphometric data. The aim of this paper is to perform an analysis of morphometric data published on porcine aorta [4, 5] and to find out, whether the orientation of VSMC within aortic tunica media is statistically linked to the composition of this layer or not.

Material and methods

Data were collected from the electronical supplements of papers recently published on porcine aorta [4,5]. The data described the distribution of VSMC quantified in 83 samples of five anatomical segments of aortae harvested from 17 pigs ranging in age from 5 to 120 days. Each of the aortic segments represented one of the following regions: the ascending aorta, aortic arch, thoracic descending aorta, suprarenal abdominal aorta, and infrarenal abdominal aorta.

Briefly, the histograms representing the orientations of VSMC nuclei visible in tangential sections were fitted using a mixture of two von Mises distributions characterized by the μ angle and κ shape (concentration, or reciprocal dispersion) parameters [8], see Eq. 1.

$$f(x \mid \mu, \kappa) = \frac{e^{\kappa \cdot \cos(x - \mu)}}{2\pi I_0(\kappa)}, \tag{1}$$

where $I_0(\kappa)$ is the modified Bessel function of the order 0. The parameter μ shows the location around which the distribution is clustered and is analogous to the mean of the normal distribution; κ shows the concentration of the distribution and is analogous to the variance of the normal (Gaussian) distribution [9]. Greater values of κ represent orientations of VMSC population more concentrated around their μ angle, while lower values of κ represent more widely dispersed VSMC orientations. We used the assumption [3,10] of the central angle of symmetry that divides the VSMC populations into two main directions (helices), each of which is characterized by its own $\mu1$ and $\mu2$ parameter. The mean angle between both directions characterizes the proximity between the two assumed symmetrical helices of VMSC. In the same samples, the intima–media thickness and the volume fractions of the following tissue constituents were assessed using stereological procedures applied on transversal histological sections: elastin, collagen, alpha-smooth muscle actin (VSMC marker), desmin (marker of contractile phenotype of VMSC), and vimentin (marker of synthetic phenotype of VSMC). The quantification technique is briefly explained in Fig. 1.

Results

Analysis of correlations revealed that the central angle of symmetry separating the two smooth muscle helices into two main directions is statistically independent of local wall composition. The mean angle between the directions of both helices was decreased in regions with a greater muscle desmin fraction (Pearson r=-0.33, p<0.05), but increased in regions with a greater elastin fraction (r=0.37, p<0.05). Whereas the directions, around which the distributions were clustered ($\mu1$ and $\mu2$ for the two helices) were statistically independent of the wall composition, the dispersions of the distributions $1/\kappa$ were increasing in regions with a greater elastin fraction (r=0.42, p<0.05), but decreasing within regions rich in desmin (r=-0.42). Biologically important correlations are summarized in Table 1.

The study has following limitations: Only morphology and microscopic arrangement of the tissue is considered without providing data on *in vivo* passive or active mechanical behavior of aortic muscle and wall matrix. Similar quantitative morphological analyses in human aortae are lacking in the literature and so is direct comparison between corresponding segments of human and porcine aorta.
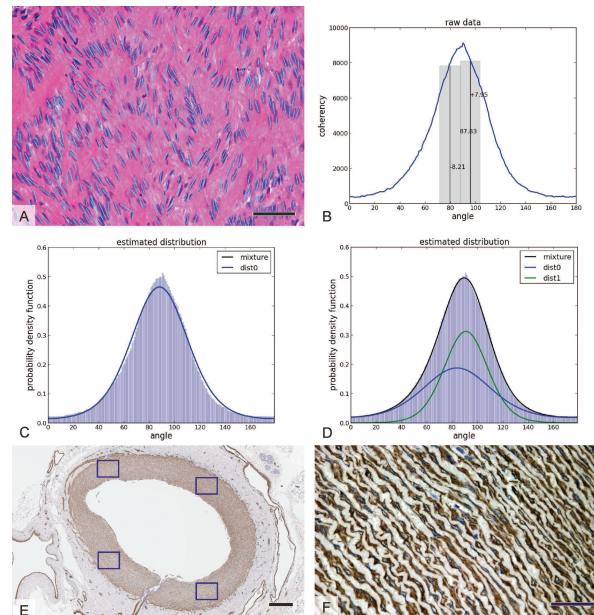
Fig. 1. Quantification of orientation of vascular smooth muscle cells (VSMC) and volume fractions of histological components. Only examples illustrating the methods are shown. For detailed primary data showing interindividual, anatomical and age-related differences, see original publicly available data [4,5]. A – The direction of each VSMC nucleus photographed in tangential sections of porcine aorta was marked using oriented line parallel to the long axis of the nucleus. Scale bar 50 μm. B – The original raw data shown as a line plot. The horizontal axis shows the angular deviation from the longitudinal direction, where the value of 90° denotes the circumferential direction. When assuming that the VSMCs are arranged in two helices according to [3,10], a central angle of symmetry (87.83 in the given example) divides the VSMC populations into two main directions. The deviations of each population from the central angle of symmetry are shown. The vertical axis represents coherency (above) defined as the ratio between the difference and the sum of the structure tensor eigenvalues according to the OrientationJ module of the ImageJ software [11]. C – Fitting the raw data using one von Mises components only may be significantly improved by adding a second von Mises distribution, as shown in D (for dist0 (blue) $\mu 1 = 79.61$, $\kappa 1 = 1.05$, for dist1 (green) $\mu 2 = 95.77$, $\kappa 1 = 1.80$). E – Four micrographs per staining method were sampled from cross sections of each aortic segment. Scale bar 500 μm. E – The volume fraction of smooth muscle actin (stained dark) was quantified using stereological point counting technique. Scale bar 50 μm. Similarly, also desmin, vimentin, collagen and elastin were quantified.

Table 1. Pearson correlation coefficients (*p<0.05) between the orientation of vascular smooth muscle, area fractions of components of the aortic tunica media and thickness of intima and media (IMT). Remaining correlations have no statistical significance (-).

	Central angle of symmetry	Mean angle	μ1	μ2	κ
Actin	-	-0.24*	-	-	0.24*
Vimentin	-	-	-	-	0.22*
Desmin	-	-0.33*	-	-	0.42*
Elastin	-	0.37*	-	-	-0.42*
Collagen	-	-	-	-	-
IMT	-	-	-	-	-

Summary

We found statistical links between the variability of VSMC orientation and composition of tunica media along aortic segments in pig. In samples with more contractile VSMC and less elastin, the symmetrical helices of VSMC were arranged closely to each other and they were more concentrated than in samples with fewer actin- and desmin-positive VSMC and more elastin. The findings are suitable for microstructurally-motivated biomechanical modeling of porcine aorta [7,12] under normal conditions. However, the individual contribution of VSMC, elastin, and collagen on both passive and active mechanics [13] of arterial wall remains to be quantified experimentally in the future.

References

[1]   K. Houdek, J. Moláček, V. Třeška, V. Křížková, L. Eberlová, L. Boudová, L. Nedorost, P. Tolinger, J. Kočová, J. Kobr, J. Baxa, V. Liška, K. Witter and Z. Tonar. Int. Angiol. Vol. 32 (2013), p. 291-306.

[2]   R.E. Shadwick. J. Exp. Biol. Vol. 202 (1999), p. 3305–3313.

[3]   G.A. Holzapfel. J. Theor. Biol. Vol. 238 (2006), p. 290–302.

[4]   Z. Tonar, P. Kochova, R. Cimrman, J. Perktold, K. Witter. Biomech. Model. Mechanobiol. Vol. 14 (2015), p. 315-332.

[5]   Z. Tonar, T. Kubíková, C. Prior, E. Demjén, V. Liška, M. Králíčková and K. Witter. Ann. Anat. Vol. 201 (2015), p. 79-90.

[6]   D.P. Sokolis, H. Boudoulas, P.E. Karayannacos. Hellenic J. Cardiol. Vol. 49 (2008), p. 145–154.

[7]   L. Horný, M. Netušil and T. Voňavková. Biomech. Model. Mechanobiol. Vol. 13 (2014), p. 783–799.

[8]   Information on https://github.com/rc/dist_mixtures, last access April 28, 2016.

[9]   F. Gao, K.S. Chia, I. Krantz, P. Nordin and D. Machin. Statist. Med. Vol. 25 (2006), p. 1593-1618.

[10] T.C. Gasser, R.W. Ogden and G.A. Holzapfel. J. R. Soc. Interface. Vol. 22 (2006), p. 15-35.

[11] R. Rezakhaniha, A. Agianniotis, J.T. Schrauwen, A. Griffa, D. Sage, C.V. Bouten, F.N. van de Vosse FN, M. Unser and N. Stergiopulos. Biomech. Model. Mechanobiol. Vol. 11 (2012), p. 461–473.

[12] S. Polzer, T.C. Gasser, K. Novak, V. Man, M. Tichy, P. Skacel and J. Bursa. Acta Biomater. Vol. 14 (2015), p. 133-145.

[13] P. Kochová, J. Kuncová, J. Svíglerová, R. Cimrman, M. Miklíková, V. Liška and Z. Tonar. Physiol. Meas. Vol. 33 (2012), p. 335-351.

Příloha VI:

KUBIKOVA, T., KOCHOVA, P., HOLECEK, M., PLENCNER, M., PROSECKA, E., FILOVA, E., RAMPICHOVA, M., TONAR, Z. In vivo microscopic and mechanical characteristics of bioengineered and biodegradable tissue scaffolds and nanomaterials. In: Grumezescu A. M. (Ed): Nanobiomaterials in Soft Tissue Engineering Applications of Nanobiomaterials, Volume 5. Elsevier, Amsterdam, 2016; 457-490.

In vivo microscopic and mechanical characteristics of bioengineered and biodegradable tissue scaffolds and nanomaterials

15

Kubíková Tereza[1]**, Kochová Petra**[2]**, Holeček Miroslav**[3]**, Plencner Martin**[4]**,
Prosecká Eva**[4]**, Filová Eva**[4]**, Rampichová Michaela**[4]** and Tonar Zbyněk**[5]

*[1]Department of Histology and Embryology, Faculty of Medicine in Pilsen, Charles University,
Prague, Czech Republic [2]European Centre of Excellence NTIS, Faculty of Applied Sciences,
University of West Bohemia, Pilsen, Czech Re/public [3]New Technologies Research Centre,
University of West Bohemia, Pilsen, Czech Republic [4]Department of Tissue Engineering,
Institute of Experimental Medicine of the ASCR, v. v. i., Prague, Czech Republic
[5]Biomedical Centre, Faculty of Medicine in Pilsen, Charles University, Prague,
Czech Republic*

15.1 INTRODUCTION

The term "biomaterial" is used for a support tool designed for protection, strengthening, or replacement of tissues, organs, or bodily functions used in close contact with living tissue (Williams, 1987). Materials of animal or plant origin or inspired by nature are also sometimes referred as to biomaterials. The function of most biomaterials is to provide mechanical support of cells. They may be modified by using adhesion molecules to stimulate a cellular response. They may be designed to release growth factors during various phases of wound healing (Palsson and Bhatia, 2004). We expect biomaterials to be compatible with the recipient's tissues to induce an acceptable organ response. Histological examination is a suitable way to verify the effect of tissue scaffolds after *in vivo* application. The type of wound, as well as the healing phases, has to be considered when selecting a suitable biomaterial for a particular use.

457

15.2 WOUND HEALING

15.2.1 PHASES OF WOUND HEALING

Recovery of damaged homeostasis begins immediately after an injury. It is a continuous process; however, it can be categorized into three phases according to the prevailing type and activity of cells involved in the healing process. These phases are the inflammatory, the proliferative, and the remodeling phases.

The hallmark of the *inflammatory phase* is early invasion of granulocytes reaching its maximum 2−5 days after injury (Reinke and Sorg, 2012). Granulocytes are attracted to the wound by chemotactic stimuli (e.g., denatured proteins, lymphokines, thromboxanes) (Helpap, 1987). Fibronectin promotes adhesion and movement of fibroblasts, keratinocytes, and endothelial cells (EC) and is present in the wound 15 min after the injury (Kondo, 2007). Three days after injury (Reinke and Sorg, 2012) macrophages appear in the healing wound. Macrophages are significantly involved in the cellular histiocytic reaction by phagocytizing necrotic tissue (Leibovich and Wiseman, 1988). Fusion of macrophages that phagocytize the nondegradable remnants form multinucleated foreign bodies giant cells, called Langhans cells (Dettmeyer, 2011). In addition to phagocytosis of bacteria and necrotic tissue (debridement), white blood cells produce growth factors, thus preparing the wound for the proliferative phase.

In the *proliferative phase*, which takes place 3−10 days after injury (Reinke and Sorg, 2012), fibroblasts are prominent. Fibroblasts produce a provisional extracellular matrix (ECM), where newly formed blood vessels are abundant, forming a granulation tissue. the spatial structure of fibrin fibers, together with adhesive proteins, provides an environment suitable for cell adhesion and migration. The provisional matrix is a rich source of mitogens, chemoattractants, cytokines, and growth factors modulating cell division (Anderson, 2001). The ECM formed in the proliferation phase contains fibrin, fibronectin, first collagen fibers, and hyaluronic acid (HA). Type III collagen is formed within 2−3 days after injury. Type I collagen, which is significantly applied, e.g., during the healing in dermis, occurs in the matrix for 5 days (Kondo, 2007). Collagen type II is formed in healing hyaline and elastic cartilage; however, the regenerative potential of these tissues is strongly limited in adults. Type IV collagen and laminin are important parts of the basal lamina of epithelia; regeneration of the basal lamina is needed for re-epithelialization. The production of extremely hydrophilic glycosaminoglycans, such as HA, provides sufficient hydration. This facilitates cell migration and improves the local microcirculation of tissue fluid and substances. Moreover, HA itself induces the release of cytokines and chemokines and thus promotes cell proliferation and differentiation. Adhesive proteins also participate in organizing the ECM. Although representation of adhesive proteins in the matrix is minor, they regulate cellular interactions, and affect cell migration and shape (Masopust and Průša, 2003). Artificial modifications of biomaterials, such as using the CD44 adhesive protein, can mimic these effects on cell proliferation

and migration. the standard type of CD44 binds HA, optional variants of CD44 bind fibronectin, laminin, and collagen.

The *remodeling phase* starts approximately 21 days after injury (Reinke and Sorg, 2012) and is characterized by intensive production of collagen fibers by myofibroblasts. Thus the primary scar is formed. Heavily vascularized tissue bulges initially, but later it is subjected to retraction due to the contractile myofibroblasts. The collagen undergoes remodeling into a more organized matrix of final scar.

15.2.2 REMODELING OF SCAR

During wound healing there are cellular responses in terms of hypertrophy, hyperplasia, atrophy, or metaplasia (Mačák and Mačáková, 2004), which are accompanied by changes in the ECM. After completion of the tissue repair processes, proliferation of myofibroblasts ceases and the excess cells undergo apoptosis. Without reducing the number and activity of myofibroblasts, fibrosis (excessive formation of connective tissue) of the wound occurs. It may suppress the healing of the functional parenchyma, the organ, or may be the cause of adhesions (Darby and Hewitson, 2007).

Problematic scars are classified as atrophic, hypertrophic, and keloid types. Atrophic scars are sunken below the line of the original injury. They arise, for example, after acne or after spontaneously healing decubitus. Hypertrophic scars can be palpated, but fundamentally do not exceed the line of the original injury. Keloid scars are only known in human. They exceed the original range of the wound (Litvik and Vantuchová, 2011). In the skin they lack the typical skin surface patterns, dermatoglyphs, and skin appendages. Women, adolescents, and darker skin phototypes with hyperpigmentation are more prone to the formation of keloid scars. Keloid scars do not occur in albinos (Litvik and Vantuchová, 2011). Keloid scars often emerge on the face, ears, neck, shoulders, neck, upper chest, and back (Seo and Sung, 2012).

The later phases of wound healing are strongly dependent on adequate nutritional support provided by the newly formed blood vessels. The formation of new blood vessels is based either on proliferation, migration, and remodeling of resident EC (angiogenesis), or on differentiation of progenitor cells into a new vascular network (vasculogenesis).

15.3 ANGIOGENESIS

15.3.1 PHASES OF ANGIOGENESIS

There are two distinct forms of neovascularization: vasculogenesis, where vessels arise de novo, and angiogenesis, in which the EC sprout from preexisting vessels. Vasculogenesis occurs mostly during embryogenesis; however, it may take part

during wound healing as well (Velazquez, 2007). Angiogenesis is encountered under physiological conditions, such as growth, or under pathological conditions, such as wound healing or remodeling of tumors (Tichý et al., 2010). The blood vessels supply the provisional granulation tissue by providing trophic factors and oxygen and taking away various metabolites. Angiogenesis depends on signals from both the blood plasma and from the surrounding matrix (Risau, 1997). These signals are present already in the inflammatory phase of healing. Angiogenesis occurs only during the proliferation phase (Li et al., 2003).

Angiogenesis may be arbitrarily divided into several steps:

1. Expression of angiogenic factor receptors (fibroblast growth factor-receptor (FGF-R), vascular endothelial growth factor-receptor) on EC (Pepper, 2001).
2. Partial degradation of the basement membrane by EC followed by penetration of EC into the surrounding tissue matrix. This requires cooperation of plasminogen activator and matrix metalloproteinases (Mignatti and Rifkin, 1996).
3. Proliferation (budding, sprouting) and differentiation of EC. The vascular buds elongate and a new blood vessel lumen forms.

Establishing new capillary routes and reinforcement of the microvessels occurs with the basal membrane, pericytes, and smooth muscle cells (Yoo and Kwon, 2013) (Figure 15.1).

15.3.2 FACTORS AFFECTING WOUND HEALING AND ANGIOGENESIS

Angiogenesis as a part of wound healing is regulated by a number of growth and differentiation factors. These include the vascular endothelial growth factor (Keck et al., 1989), the fibroblast growth factor (Folkman and Klagsbrun, 1987), the angiopoietins (Suri et al., 1996), the platelet-derived growth factor, the epidermal growth factor, and the transforming growth factor beta (Yang and Moses, 1990). A selection of factors with most evidence and relevance to wound healing is given in Table 15.1.

15.3.3 PROMOTING ANGIOGENESIS IN BIOMATERIALS

Replacement and restoration of various parts of the body has been previously limited to either avascular tissues (such as cartilage) or thin-layered organs (epidermis, urinary bladder) (Atala et al., 2006; Jain, 2003; Oberpenning et al., 1999). Cell viability within these organs depends on oxygen and nutrient diffusion, the efficiency of which is limited to a few hundred microns. Cells more distant from the nearest capillaries suffer from hypoxia, which may result in their apoptosis.

Insufficient supply of oxygen and nutrients is a complication for wound healing. Diabetic ulcer is an example of chronic wounds. A reason for the formation of diabetic ulcers is inadequate blood supply with complicated healing leading to recurrent inflammation and infection (Steed, 2006). On the other side, uncontrolled
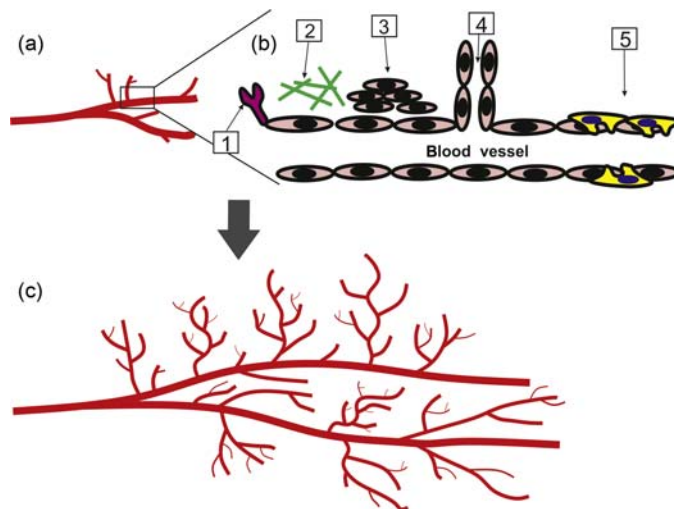
FIGURE 15.1

Angiogenesis. (a) Vascular network before wound healing; (b) phases of angiogenesis:
(1) growth factors binding on endothelial cell receptors; (2) matrix metalloproteinases
degrade the basal lamina; (3) EC proliferate and migrate; (4) vascular channels (tubes)
are formed and undergo remodeling; (5) blood vessels are stabilized with pericytes;
(c) vascular network after wound healing.

Redrawn and modified from Yoo and Kwon (2013).

angiogenesis also leads to severe pathological conditions, such as macular degeneration of the retina and tumor growth (Patel and Mikos, 2004). Controlled application of angiogenic or antiangiogenic factors delivered in scaffolds may support proper vascularization of healing wounds (Moon and West, 2008).

15.3.3.1 Modification of material to promote neovascularization

Scaffolds that underwent *ex vivo* prevascularization can be transplanted *in vivo* to integrate with the host microvasculature. This utilizes various biochemical signals embedded within scaffolds to simulation of the natural tissue microenvironment and to revitalize the angiogenic potential of seeded cells. These scaffolds are frequently modified with ECM proteins organized in micropatterns to provide a guiding network for angiogenesis. Into tissue may be delivered angiogenic factors, vascular cells, and other supporting cell types (Moon and West, 2008).

Modifications using ECM proteins or ECM-derived peptides—ECM proteins, such as collagen and fibronectin, often cover surfaces of biomaterials to augment their interaction with cells. An ECM coat on biomaterials can facilitate neovascularization *in vivo* (Moon and West, 2008).

Cellular interactions with ECM proteins are quite complex because these proteins present cells with multiple cell binding and growth factor binding domains.

Table 15.1 Growth and Differentiation Factors Involved in Wound Healing

Name of Factor	Origin	Function
PDGF (platelet-derived growth factor)	α Granules of platelets	The family of PDGF are mitogens and chemoattractants for fibroblasts (Ross et al., 1986; Seppä et al., 1982), smooth muscle cells (Grotendorst et al., 1982; Sjölund et al., 1988), and other cells of mesenchymal origin (Mutsaers et al., 1997)
		Chemotaxis of neutrophils and monocytes stimulates the activation of macrophages (Deuel et al., 1982; Tzeng et al., 1985)
		Regulates gene expression of fibronectin (Blatti et al., 1988), synthesis of protocollagen (Butt et al., 1995), and increases the activity of collagenase (Bauer et al., 1985)
TGF-β (transforming growth factor beta)	Fibroblasts, platelets, monocytes, chondrocytes, osteoblasts	TGF-β leads to the formation of fibronectin, type I and III collagen (Ferguson and O'Kane, 2004). Simultaneously it inhibits the formation of metalloproteainases in fibroblasts and thus prevents collagen degradation (a large quantity of TGF-β leads to creation of a hypertrophic scar) (Pakyari et al., 2013)
FGF (fibroblast growth factor)	Damage endothelial cells (EC) and macrophages	The family of FGF is mitogenic for EC, regulates migration and proliferation of EC (Folkman, 1987; Montesano, 1986)
		It is also mitogenic for keratinocytes (Ristow and Messmer, 1988)
EGF (epidermal growth factor)	Platelets and macrophages	The EGF family supports the mitoses of fibroblasts, keratinocytes, smooth muscle cells, and epithelial cells (Laato et al., 1987; Rheinwald and Green, 1977; Schreiber et al., 1986)

To overcome these issues, peptides, often only several amino acids long, have been derived from ECM proteins as the most basic subunits required for normal cell adhesion and proliferation (Moon and West, 2008).

Cellular interactions with ECM proteins are quite complex. For effective cell adhesion and proliferation to be sufficient often only several amino acids are derived from ECM proteins, such as Arg-Gly-Asp-Ser (RGDS) peptide derived from vitronectin and fibronectin and Tyr-Iso-Gly-Ser-Arg, YIGSR is a peptide sequence derived from laminin (Moon and West, 2008).

Micropatterning techniques to regulate angiogenesis—Micropatterning techniques such as photolithographic patterning, micromolding, microcontact printing, and laser photolithography can allow control over the presentation of angiogenic biomolecules at cellular-length scales (Moon and West, 2008). Photolithography provides a convenient method to micropattern molecules onto the surfaces of biomaterials. Microcontact printing commonly uses the strong interaction between thiol-containing moieties and a gold substrate to pattern different biomolecules. Micromolding processes have been applied to create complex tissue architectures in scaffold materials. Laser photolithography exploits selective photopolymerization of biomolecules with lasers to create internally complex 3D materials (Moon and West, 2008).

15.3.3.2 *Controlled drug delivery from natural ECM polymers*

Delivering angiogenic factors using a bolus injection is associated with negative side effects (hyperpermeable vessels, hypotension, uncontrolled angiogenesis, and stimulation of tumor growth) in surrounding nontarget tissues (Epstein et al., 2001). Therefore, the aim of tissue engineering is to provide a targeted and consistent delivery of angiogenic factors.

Simple loading—Interception of growth factors in scaffolds is an easy way to delivery drug (Moon and West, 2008). FGF-2 was added by Obara et al. (2003) during polymerization of chitosan hydrogels. Most of the added FGF-2 was released in a sustained fashion during *in vivo* degradation. Obara et al. (2003) observed increased capillary formation in healing-impaired diabetic mice model in a group with chitosan scaffold and addition of FGF-2 (Obara et al., 2003).

Ionic complexation—Using ionic complexation of growth factors with scaffolds is another way to deliver growth factors (Moon and West, 2008). Ionic interactions between positively charged growth factor and negatively charged polymers promote slow initial release of growth factors (Tabata and Ikada, 1999).

Heparin-mediated release—Modification of natural ECM proteins, such as heparin, conducts an increased angiogenic potential. Heparin binds to a number of growth factors and releases later on in response to cellular activities. Heparin also helps to protect growth factors from proteolytic degradation, thus increasing the presentation and availability of these factors (Sakiyama-Elbert and Hubbell, 2000).

15.4 BIOMATERIALS USED IN WOUND HEALING
15.4.1 ORIGIN OF BIOMATERIALS

Biomaterials are natural or synthetically produced. However, in both cases they are subjected to additional modifications of their composition, shape, texture, or surface using tissue engineering techniques. Natural biomaterials are usually glycoproteins, proteins, or polysaccharides. ECM is itself a very complex natural

biomaterial, which provides mechanical support and affects the function and fate of cells.

The origin of natural materials is (Palsson and Bhatia, 2004):

- autologous—coming from other parts of the body of the same individual;
- isogenic—derived from a genetically identical individual;
- allogenic—originating from another individual of the same species;
- xenogenic—originating from other animal species.

Xenogenic and allogenic antigens induce an unwanted inflammatory response in the recipient's tissues. To prevent this, the antigens are removed from the grafts using decellularization. This may be done using physical factors (freeze), chemical substances (Triton X-100, hypotonic or hypertonic sodium EDTA) (Hrebikova et al., 2013), enzymes (trypsin, exonuclease), protease inhibitors (aprotinin), and antibiotics (penicillin, streptomycin) (Gilbert et al., 2006).

15.4.2 **PROPERTIES OF BIOMATERIALS**

The biological response to the presence of the biomaterial in the tissue is influenced by a combination of physical and chemical properties (surface area, size, chemical composition) and biological properties (immunoreactivity, adhesion to cells and intercellular matrix, etc.). The interaction between cells and the material is a combination of nonspecific and specific interactions reflecting the surface topography. The nonspecific interactions are due to van der Waals forces, electrostatic repulsion, hydration, and solvation forces. The biological interactions are due to adhesion molecules on the cell surfaces. For example, fibronectin as protein of ECM (Lewandowska et al., 1992) is a very effective cell-adhesive substance. Similarly, laminin, being a key component of the basement membrane, is a powerful cell-binding agent (Christopherson et al., 2009). In contrast, albumin is an effective nonadhesive biological coating on hydrophobic surfaces due to its irreversible strong adsorption and conformational change (Dekker et al., 1991).

The topology of the surface, stiffness of scaffold, size of the pores, and thickness of the biomaterial influence not only the cell adhesion, but also cell proliferation, migration, and function (Palsson and Bhatia, 2004). Uygun (2010) observed the growth of rat mesenchymal stem cells (MSCs) on chitosan membranes of various thicknesses. He detected significantly improved cell adhesion, spreading, and proliferation that was accompanied by increased membrane thickness. Similarly to the MSCs, rat hepatocytes also exhibited increased growth on the substrate with a thickened basal membrane (Uygun et al., 2010).

Zeltinger et al. (2001) followed the influence of pore size on the attachment, growth, and ECM deposition in several cell types. Canine dermal fibroblasts showed no preference for the pore sizes tested (for pores ranging from 38 to 150 μm). However, the growth of vascular smooth muscle cells and microvascular EC favored the scaffolds with larger pore size (Zeltinger et al., 2001).

Fibroblasts, epithelial cells, and EC showed increased proliferation on stiffer substrates. In contrast, neurons showed greater proliferation on softer substrates, which correlated with their natural environment in the brain (Engler et al., 2004).

Modifying the physical properties (e.g., the surface charge) on the biomaterial can significantly affect and control the growth of various types of cells (Hejcl et al., 2009).

15.4.2.1 Mechanical properties of biomaterials

This section summarizes the mechanical properties of various biomaterials used in medicine.

15.4.2.1.1 Polymers

Polymers are flexible, resistant to biochemical attack, have good compatibility, light weight, and are available in a wide variety of compositions with adequate physical and mechanical properties (Hench and Jones, 2005; Ifkovits and Burdick, 2007; Patel and Gohil, 2012; Pruitt and Chakravartula, 2011; Ratner, 2012; Seal, 2001; Wong and Bronzino, 2007). They can be easily shaped. Whereas the first medically used polymers were industrial polymers, new polymers have been specially synthesized for medical use. They are broadly used in tissue engineering, implantation of medical devices and artificial organs, prostheses, dentistry, bone repair, drug delivery and targeting into sites of inflammation or tumors, plastic tubing for intravenous infusion, bags for the transport of blood plasma, and catheters (Langer and Vacanti, 1993; Patel and Gohil, 2012).

Polymers can be amorphous, having no crystallinity, and exhibit glass-like properties (below glass transition temperature) as well as elastomeric properties (above glass transition temperature). Other forms are semicrystalline polymers that contain amorphous as well as crystalline regions. The mechanical parameters are highly influenced by the degree of crystallinity. The Young's modulus and yield stress generally increase with the degree of crystallinity, the ultimate elongation is reduced. Ultimate strength and fracture toughness may increase or decrease with crystallinity.

The currently used biomedical polymers cover a broad spectrum of polymers with various mechanical properties (Seal, 2001). Bioinert polymers cover poly (tetrafluoroethylene) (PTFE), poly(methylmethacrylate) (PMMA), polyethylene (PE), silicones, polyamides, poly(ethyleneterephthalate), and polyurethanes. Bioresorbable polymers, which are designed to degrade within the body after performing its function, cover polylactide, polyglycolide, poly(-3-hydroxybutyrate), polyhyaluronic acid esters, polydioxanone, and copolymers. Natural polymers, or polymers derived from living creatures, such as collagen, chitosan, HA, fibrin, and alginate, are also of great interest in the biomaterials field.

PTFE, a fluorocarbon-based polymer known as Teflon, is chemically extremely stable. It can be produced in various forms, such as woven into porous meshes, tubes, sheets (Goretex^{TM}), or as coatings (Dacron^{TM}). This makes it ideal for sutures, catheters, artificial vascular grafts, and mechanical heart valves. The

limitations in use are due to relatively poor mechanical properties: low modulus of elasticity (0.5 MPa), low tensile strength (14−30 MPa), and low yield strength. The ultimate elongation is 120−350%.

PMMA is a hard, rigid, glassy but brittle polymer. PMMA has a modulus of elasticity of 2.2 GPa, tensile strength 30 MPa, and ultimate deformation 1.4%. Alone it is used in intraocular lenses and hard contact lenses, or it can be used as bone cementum in joint replacement surgery. The macromolecule composed of multiple PMMA molecules creates resins. Its physical properties are suitable for dental applications. The strength of an individual denture base resin is dependent on the composition of the resin, processing technique, conditions presented by the oral environment, and degree of polymerization. As the degree of polymerization increases, the strength of the resin increases.

PE is a polymer with low yield strength. It can be increased by crystallinity and by increasing molecular weight (Mw). It is stable and suitable for long-term implantation of joint (knee, ankle) replacements or as catheters. The ultra-high-molecular-weight PE has a modulus of elasticity of 4−12 GPa, tensile strength higher than 35 MPa, and ultimate deformation higher than 300%.

Collagen is a natural protein providing high strength to tissues. Collagen may also be processed into various forms, such as porous sponges, gels, and sheets. Chemical crosslinking of collagen increases its strength and stability. Collagen can have an effect causing alteration of cell behavior (e.g., changes in growth), it may have inopportune mechanical properties, or suffer shrinkage. Fortunately, it is possible to improve the mechanical properties of collagen by its combination with other biological or synthetic materials. Collagen combined with elastin and gelatin can be used to create scaffold for use in soft tissue engineering (Grover et al., 2012).

Chitosan is a natural polysaccharide that is derived from chitin present in hard exoskeletons of shellfish. It has controllable mechanical/biodegradation properties (such as porosity). Chitosan has broad possibilities for application, such as drug delivery, engineering of cartilage, nerve and liver tissue. Chitosan has low strength and inconsistent behavior with seeded cells, so alone chitosan cannot be used as a polymer scaffold in tissue engineering. However, chitosan may be easily combined with other materials to increase its strength and cell attachment potential (Nwe et al., 2009).

Alginate is a brown seaweed-derived polysaccharide. It has been tested for use in nerve, heart, liver, and cartilage tissue engineering. Alginate alone is mechanically weak and has poor cell adhesion. The strength of alginates has been increased by combining it with different polymer substances, such as agarose and chitosan (Kong et al., 2004; Sun and Tan, 2013).

15.4.2.1.2 Composites

Composite materials are a mixture of two or more phases (Burdick and Mauck, 2011; Hench and Jones, 2005; Ratner, 2012; Wang, 2003; Wong and Bronzino, 2007). The stress transfer occurs across the phase boundary. Composite

biomaterials offer a variety of advantages in comparison with homogeneous materials. The individual homogeneous materials could have good properties such as lightness, easy production, but they could be limited by some mechanical properties. The combination of two or more materials together leads to an improvement of mechanical properties to emulate the mechanical properties of biological tissues. In particular, the properties of a composite material depend upon the shape of the heterogeneities, upon the volume fraction occupied by them, and upon the interface among the constituents. This has promising potential for stiff, strong, light-weight materials as well as for highly resilient and compliant materials. The material, mostly a polymer, is stiffened or hardened by the integration of the second-phase particulate inclusions. The elastic modulus of composite is significantly affected by the ratio of the second-phase modulus to the matrix modulus and volume fraction of the second-phase particles. It was found that the shape of the inclusion affects the stiffness of the composite. Stiff spherical particles are recommended to reach a stiff composite. The mechanical properties of composites could be isotropic, i.e., the same in all directions, or anisotropic, i.e., different properties in different directions. Note that billions of years of evolution led to development of almost always anisotropic biological materials.

Most natural structural biological materials are composites (Hench and Jones, 2005). The soft tissues are composed mostly from collagen fibers, elastic fibers, and amorphous ground substance among the matrix fibers. Elastin has tension strength about 1 MPa and ultimate elongation 100%. Collagen has a higher tensile strength between 50 and 100 MPa and lower ultimate elongation about 10%. Their composite in tendons with a low elastin content has ultimate strength 53 MPa, ultimate elongation about 10%, while in skin with a high elastin content the ultimate strength is about 8 MPa and ultimate elongation about 80%.

15.5 ANIMAL MODELS

Although some of the interactions between the biomaterials and organisms may be inferred from *in vitro* testing, further testing of the most promising materials requires the next stage of tests, i.e., *in vivo* tests. Animal models are used for *in vivo* evaluation of the interactions between tissues and tissue scaffolds. Biomaterial is implanted into an organ artificially damaged during the experiment under controlled conditions. Samples for analysis are taken away after different time intervals. The healing of the defect is then evaluated by noninvasive imaging methods such as X-ray examination, computed tomography, ultrasound sonography, magnetic resonance imaging (MRI), or histology, revealing microscopic changes in the defect. Table 15.2 reviews the model animals used for *in vivo* assays of biomaterials intended for healing of skin, cartilage, abdominal closure, and implanted arterial banding.

Table 15.2 Animal Models for *In Vivo* Evaluation of Biomaterials Designated for Healing of Skin, Cartilage, and Abdominal Closure and for Implantation of Arterial Banding; Typical Localization of Defects and Time Interval of Sampling of Individual Organs and Species

Area of Interest	Animal Model	Localization of Defect	Samples were Taken After
Healing of skin wounds	Rat	Back (Krasnov et al., 2012; Meruane et al., 2012)	1, 2, and 3 weeks (Meruane et al., 2012)
			14 and 25 days (Krasnov et al., 2012)
	Rabbit	Back (Ananta et al., 2012; Ulubayram et al., 2001)	1, 3, and 5 weeks (Ananta et al., 2012.)
			1, 2, and 3 weeks (Ulubayram et al., 2001)
Healing of hyaline cartilage	Dog	Knee (Breinan et al., 2001; Igarashi et al., 2012).	1.5, 3, 6, 12, and 18 months (Breinan et al., 2001.)
			16 weeks (Igarashi et al., 2012)
	Pig	Knee (Cui et al., 2011; Filová et al., 2013)	12 months (Filová et al., 2013)
			6 months (Cui et al., 2011)
	Rabbit	Knee (Fan et al., 2010; Filová et al., 2008)	8 weeks (Fan et al., 2010)
			6 weeks (Filová et al., 2008)
Healing of abdominal closure	Rabbit	Fascia	6 weeks (Plencner et al., 2014)
	Chinchilla, rabbit	Abdominal wall	7, 21 days (Lambertz et al., 2014)
	Pig	Fascia	2, 4 weeks (Monteiro et al., 2013)
	Rat	Abdominal wall	5, 9 weeks (Song et al., 2013)
Implanted arterial banding	Pig	The pulmonary trunk about 1 cm above the valve; constrict to 70–80% of the original diameter	5 weeks (Nedorost et al., 2013)
	Mice	Aorta	14 days (Rockman et al., 1994)

15.6 *IN VIVO* MICROSCOPIC AND MECHANICAL CHARACTERIZATION OF BIOMATERIALS

To evaluate the suitability of the biomaterial we can combine mechanical tests with biochemical and histological analyses.

15.6.1 MECHANICAL CHARACTERIZATION OF BIOMATERIALS

The bioengineering and biodegradable tissue scaffolds and nanomaterials cover a broad spectrum of biomaterials (metals, ceramics, polymers, and composites) which replace a part or a function of various organs and tissues of the body (Hench and Jones, 2005; Jaffe et al., 2013; Pruitt and Chakravartula, 2011; Wong and Bronzino, 2007). These biomaterials and related devices have mechanical and performance requirements that originate from the usage in the body and the physical properties of the materials (Ratner, 2012; Ratner et al., 2012). A hip prosthesis has to be strong and rigid; a tendon material should be strong but flexible; an articular cartilage substitute should be soft and elastomeric; a heart valve leaflet should be flexible and tough; a dialysis membrane has to be strong and flexible.

Biomaterials have to have not only the special mechanical properties according to their usage but they also have to maintain them in *in vivo* conditions over a specific time (mechanical durability) (Parida, 2012; Ratner, 2012). A syringe needle is in contact with the body for only 1−2 s, and a tongue depressor 10 s, while contact lenses are in contact with the eye from 12 h up to 30 days; a bone plate or screw may fulfill its function for 6 months or longer, and a total hip replacement up to 20 years. The leaflets of heart valves must bend 60 times per minute without forming tears during the expected patient's lifetime (10 years at least). A hip joint must keep under heavy loads for more than 10 years. The intraocular lenses, which may fulfill their function for 30 and more years, are an extreme case. We have to take into account that the mechanical properties of the implanted biomaterials could differ before implantation, in *in vivo* conditions after implantation and could change in time through use. The biomaterials are therefore exposed to many mechanical and optical tests to assess their mechanical behavior (Jaffe et al., 2013; Pruitt and Chakravartula, 2011).

15.6.2 MECHANICAL TESTS

The biomaterials are in *in vivo* conditions exposed to mechanical loading (tension, pressure, shear, torsion; Figure 15.2) (Ratner, 2012). When a force is applied to a material, an opposite force causing a stress in the material exists within the material (Hench and Jones, 2005). The stress defined as the force per unit area (units Pa) causes the material to deform. The ratio between the actual deformation and original dimensions of material sample is called strain (dimensionless).

To find the mechanical behavior and the mechanical parameters (modulus of elasticity, yield strength, ultimate tensile strength, and deformation), the biomaterials are exposed to various loading tests (pulling, pushing, bending, or rotation; Figure 15.2) (Pruitt and Chakravartula, 2011; Ratner, 2012).

15.6.2.1 Tensile testing

The most frequent mechanical test is the uniaxial tensile test (Figure 15.2a). The material is loaded by a given force or elongation in one chosen direction. The loading leads to elongation or stress production in the direction of loading.
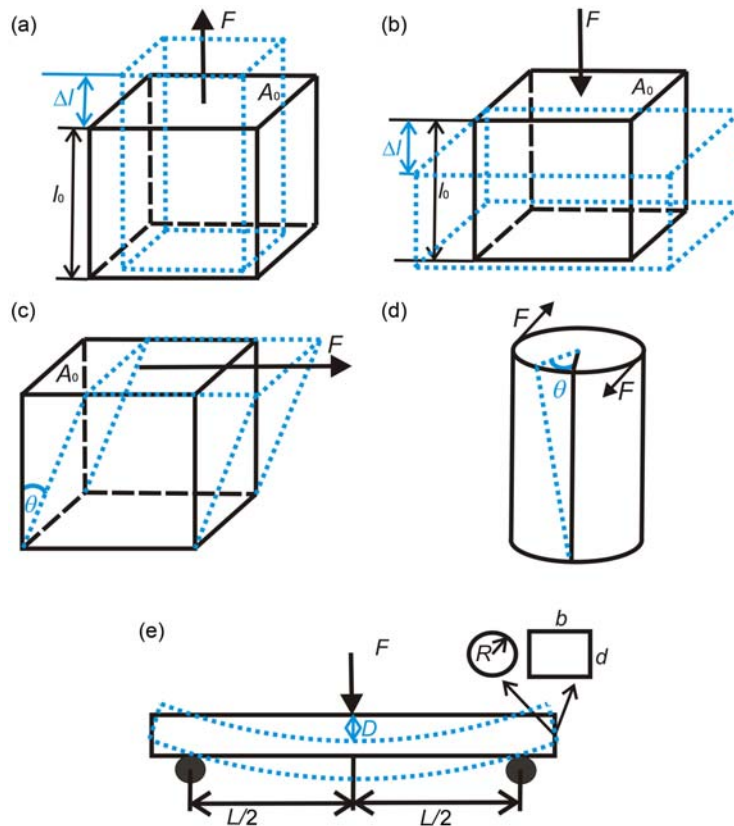
FIGURE 15.2

Types of loading: (a) tensile loading; (b) pressure loading; (c) shear loading; (d) torsion loading; (e) bending loading. F is the loading force, A_0 is the initial cross section area, l_0 is the initial dimension (length), Δl is the actual deformation, θ is the deformation angle, R is the cylinder radius, b, d are the width and thickness of the beam, respectively, L is the support span, and D is the deflection of the center of the beam.

The loading is applied perpendicularly to the cross section of the sample. The result of such a measurement is the *stress—strain curve* (Figure 15.3) plotted with strain on the *x*-axis and stress on the *y*-axis to show the relationship between the applied stress and strain. The stress—strain curve characterizes the mechanical performance of a material, such as yield strength, tensile strength, elastic modulus, elongation, and toughness.

The shape of the stress—strain curve differs between materials. Most materials initially have a linear proportion between stress and strain, whereas the slope (gradient) of this initial stress—strain curve is the *elastic modulus* or *Young's*
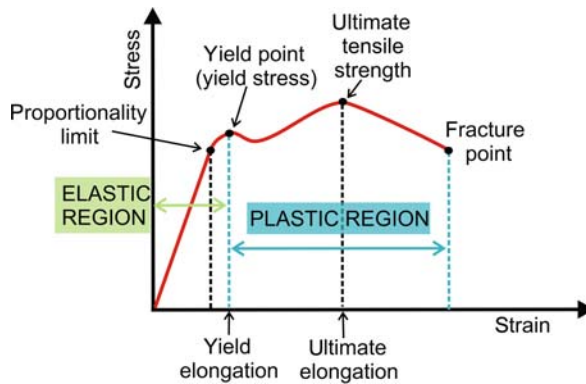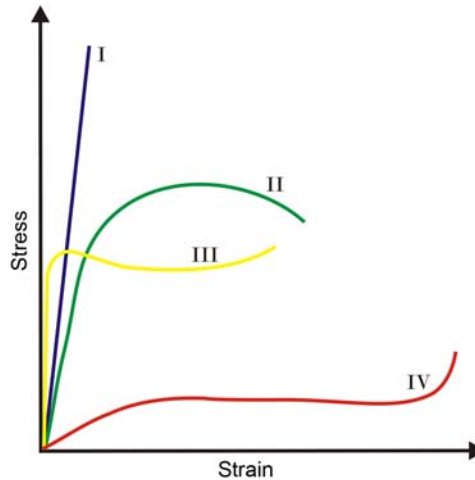
FIGURE 15.3

An example of a general stress−strain curve with typical features denoted.

modulus (*E*). A high elastic modulus corresponds with a greater rigidity of the material, that is, more stress is required to produce a given amount of strain. The linear relation is governed by Hooke's law = *E*. If the stress is removed during this stage of deformation, the material will return to its original dimensions. This process is repeatable, reversible, and is called *elastic deformation*. The *proportionality limit* on the stress−strain curve is the value of stress after which the material deformation no longer varies linearly with the applied stress.

Brittle materials, such as ceramics and glasses, break immediately after they undergo a critical (generally very small) amount of elastic deformation (Figure 15.4I). The plastic polymers and metals undergo, with increasing loading, the second stage of deformation called *plastic deformation* (Figure 15.3, Figure 15.4II—metals, Figure 15.4III—plastic polymers). The gradient of the stress−strain curve is changed in the plastic stage: a significant increase in strain is connected with little or no increase in stress. The point of change is called *yield point* (*yield strength*—σy, *yield point strain*—εyp). After the loading exceeds the yield point, when the material is unloaded, it does not return to its original dimensions, and a permanent plastic deformation remains. In metals, further increasing the strain loading after the yield point is characterized by the stress increasing very slowly and is followed by metal fracture. The stress−strain curve of plastic polymers differs from metals after the yield point. At high strain level, the stress is nearly independent of strain and shows a slight increase. For elastic polymers the stress increases very slowly with increasing strain even for small strains (Figure 15.4IV) and the fracture occurs at very high strain values.

The maximum tensile stress that can be applied to the material before rupture is called the *ultimate (maximum) tensile strength* (σUTS). The metals deform near this ultimate value usually so much that they have already failed to perform their function. The limitation factor for selecting metals for a given application is thus the yield strength and not the ultimate tensile strength.

FIGURE 15.4

Stress—strain curve of ceramics (I), metals (II), plastic polymers (III), and elastic polymers (IV).

The other mechanical parameter obtained from the stress—strain curve is the *ultimate elongation* or the *ductility* of the material. In other words, the amount of strain that the material can undergo before rupture. The plastic strain could be quoted or the percentage changes in length of the fractured material to its original length. Note that the ultimate elongation cannot be used to predict the behavior of materials subjected to sudden or repeated loading.

Another mechanical parameter is the *toughness*. This is a measure of the resistance of a material to failure. The toughness is the area under the stress—strain curve. It corresponds to the energy required to fracture the material. Tough materials have a high value of toughness and are difficult to break. In contrast, brittle materials such as ceramics and glasses have a low value of toughness and the material is quite easily broken, often with little or no warning. Tough materials such as metals are also more resistant to impact loading or sudden changes of loading.

In order to match the mechanical properties of the surrounding tissue, it is important to note that the stress—strain curves of biological tissues are highly *nonlinear*. Such nonlinearity is much harder to quantify.

15.6.2.2 Compression testing

During compression test, the material is loaded by pressure in one chosen direction (Figure 15.2b). It is performed on biomaterials exposed to pressure in the body (bone, ligaments, or cartilage implants) and on biomaterials subjected to compressive forces during operation (orthopedic implants). The material is

deformed according to a pressure loading and the relation between stress and deformation results in the stress—strain curve. The force is taken to be negative and the strain also reaches negative values. According to the tensile test the modulus of elasticity in pressure and the *compressive strength* are determined from the stress—strain curve. The *modulus of elasticity in pressure* is the slope of the linear part of the stress—strain curve. This is usually called the initial modulus of elasticity and is determined for strain between 2% and 10%. The compressive strength determines the capacity of material to withstand pressure loading until the rupture.

15.6.2.3 Shear and torsion testing

The shear (Figure 15.2c) and torsion (Figure 15.2d) test is applied to materials which undergo this kind of loading in the body (bone implants) and to brittle materials. In some cases, torsion forces may be applied to a sample instead of a pure shear.

During the shear test, the forces are parallel to the top and the bottom surfaces of the material sample. Shear stress (τ) is defined as the force divided by the original cross-sectional area of the sample. Shear strain (degree of rotation, γ, or angular displacement) is defined as the tangent of the deformation angle (θ). The relationship between shear stress and shear strain is plotted in the stress—strain curve. The slope of the linear part of the stress—strain under the proportionality limit is the *shear modulus* (G). The linear part is governed, analogically to the tensile test, by Hooke's law in the form $\tau = G\gamma$, where G is the shear modulus. The other mechanical parameters, elastic limit, yield strength, and ultimate strength can be obtained from the stress—strain curve analogically to the tensile test.

15.6.2.4 Bending testing

The three-point bending flexural test (Figure 15.2e) is mostly used to determine the modulus of elasticity in bending (flexural modulus, Ef), ultimate strength in bending, and toughness of the material. The tested specimen is a cylinder with radius (R), or a beam with rectangular cross section ($b \times d$, width $\times$ thickness). The parameters can again be obtained from the stress—strain curve. We denote by F the load at a given point on the load deflection curve, by L the support span, by D the deflection of the center of the beam, and by m the gradient (i.e., slope) of the initial straight-line portion of the load deflection curve. The flexural stress is defined as $\sigma f = 3FL/2bd^2$ (rectangular cross section) or $\sigma f = FL/\pi R^3$ (circular cross section), the flexural strain is defined as $\varepsilon f = 6Dd/L^2$. *Flexural modulus* is calculated as $Ef = L3m/4bd^3$. The *flexural strength* is the stress required to fracture the sample and is calculated as $\sigma mr = 3FL/2bd^2$, with F being here the smallest load that causes the fracture.

15.6.2.5 Fatigue testing

The biomaterials after implantation into the body very often undergo some type of cyclic loading (Pruitt and Chakravartula, 2011; Teoh, 2000). The progressive deterioration of the strength of a material or structural component during service means that a failure can occur at much lower stress levels than the ultimate stress of the material. This effect is called *fatigue*. Most alloys will fail at decreasing cycle stress amplitude as the number of stress cycles increases. The *fatigue limit* can be defined as the number of cycles that a material survives with a given stress amplitude. Alternatively, the *fatigue stress* can be defined as the stress that a material survives for some large number of cycles (10^7 or 10^8 cycles are typical). The fatigue stress is determined, i.e., for aluminum, magnesium, and most nonferrous metals. The aluminum has a fatigue stress typically one-third of the tensile strength of the alloy. Many steels and titanium alloys instead show a fatigue limit.

15.6.3 MICROSCOPIC CHARACTERIZATION OF BIOMATERIALS

15.6.3.1 Histological assessment

Histology provides information on the microscopic morphology, location, history, and current stage of healing, the formation of ECM, vascularization, tissue architectonics, inflammatory response to the presence of the biomaterial, and others. The most common processing of samples of soft tissue is by chemical fixation and paraffin embedding. The temperature during embedding samples to paraffin block (56 °C) leads to damage of thermo-labile materials. Alternatively, therefore, bypass the paraffin freezing process (ca. -25 °C) and take sections using a cryomicrotome.

One of the most challenging points in histological studies evaluating the impact of biomaterials *in vivo* is to choose appropriate technology and methods relevant to the original biological question of the experiment. It is possible to use scoring systems, in which the investigated parameters are classified using semiquantitative scoring scales. The scales might reflect the cellular morphology, positivity of the ECM ground substance to neutral or acidic glycosaminoglycans, surface regularity, structural integrity, thickness, degree of integration with the adjacent tissue, cellularity, clustering of chondrocytes, the presence of degenerative changes, or other morphological features (Filová et al., 2007; van Susante et al., 1999). A different strategy is to quantify the tissue composition using stereology and continuous variables that describe, e.g., cell number per unit volume, the length of the blood vessels or fibrous matrix structure, surface area, surface and volume fractions of the components of tissue, clustering and colocalization of microscopic objects. Many applications of quantitative microscopy are dominated by technique stereology. This way we can obtain information about the three-dimensional structure measurements made on the two-dimensional planar sections (Mouton, 2002).
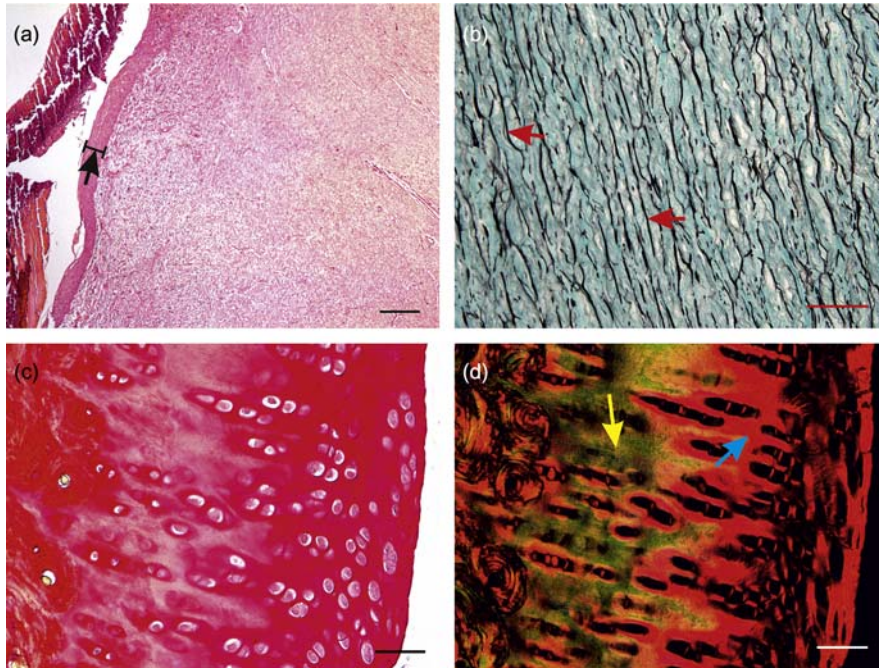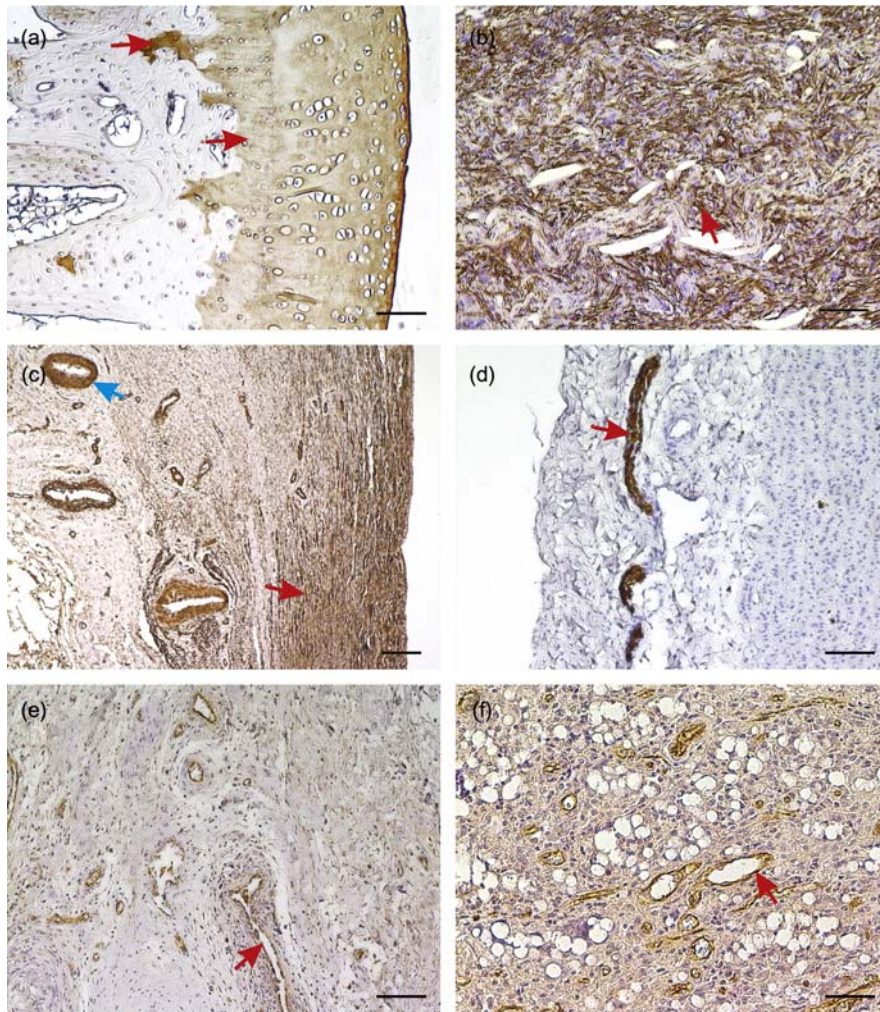
FIGURE 15.5

Microphotographs of stained tissue sections. (a) Epidermis (black arrow) newly formed during skin healing in rabbit, HE stain, scale bar 200 μm; (b) black elastic fibers and green collagen fibers within an elastic artery, Verhoeff's hematoxylin and green trichrome stain, scale bar 50 μm; (c) hyaline cartilage stained by picrosirius red and observed in a bright-field microscope, scale bar 50 μm; (d) hyaline cartilage stained by picrosirius red observed using polarized light, type I collagen appearing as red and yellow fibers (blue arrow), type III collagen appearing as green fibers (yellow arrow), scale bar 50 μm.

15.6.3.2 Biological importance of parameters from quantitative analysis

A high proportion of mature type I collagen fibers in a defect contributes to the mechanical resistance of the tissue (Fung, 1993; Screen, 2008). Increasing the ratio of collagen I/III means mechanically strong maturation of precursors of type III collagen into the type I collagen (Junge et al., 2004). A suitable method for differentiating the type I and type III collagen is the picrosirius red histological staining combined with circularly polarized light microscopy (Figure 15.5c and d) (Meruane et al., 2012). Type II collagen is present in ECM of hyaline and elastic cartilage. For detection of collagen II, immunohistochemistry applying an anticollagen II antibody may be used (Figure 15.6a; Rampichová et al., 2010).

FIGURE 15.6

Microphotographs of tissue sections stained using immunohistochemistry. (a) Detection of type II collagen type (brown area, red arrow) within the extracellular matrix of hyaline cartilage using anticollagen II antibody, scale bar 100 μm. (b) Immunohistochemical detection of α-smooth muscle actin showing positive myofibroblasts (brown cytoplasm, red arrow) in healing abdominal incision, scale bar 100 μm. (c) Immunohistochemical detection of α-smooth muscle actin showing positive smooth muscle cells in tunica media of pulmonary artery (brown area, red arrow) and positive smooth muscle cells in the vasa vasorum (blue arrow), scale bar 200 μm. (d) Immunohistochemical detection of the neurofilament protein showing peripheral nerves (the nervi vasorum) within the tunica

(*Continued*)

A high proportion of elastin fibers in a defect contributes to the elasticity of the tissue (Fung, 1993). Modified green trichrome with Verhoeff's hematoxylin can be used to detect elastin fibers (Figure 15.5b; Kocová, 1970).

A high proportion of contractile myofibroblasts in the healing lesion contributes to wound contraction (Nowak et al., 2009; Van Beurden et al., 2005). Antibody antismooth muscle actin detects myofibroblasts (Figure 15.6b) and smooth muscle cells in media of vessels in tissues (Figure 15.6c; Plencner et al., 2014).

A high density of microvessels in a wound contributes to the regeneration and growth of tissue. Numerical and length density of microvessels in three dimensions, or the density of microvessel profiles in two dimensions, may be quantified. EC may be visualized using anti-von Willebrand factor antibody (Figure 15.6e; Meruane et al., 2012) or anti-CD31 antibody (Figure 15.6f; Plencner et al., 2014).

High numbers of inflammatory cells (leukocytes, macrophages) in a wound are linked to the immune response to injury (Adamson, 2009). Neutrophilic granulocytes react with antimyeloperoxidase antibody (Andrade et al., 2011). Macrophages react with anticapprotectin antibodies (Brandtzaeg et al., 1992; Marin et al., 1995), with anti-CD14 and anti-CD163 (Evans et al., 2013), and with anti-CD36 antibodies (Ortiz-Masià et al., 2012). Unfortunately, there is currently no single commercially available antibody that would be entirely specific for macrophages in all model animal species.

The thickness of newly formed epidermis is important for the evaluation of skin healing. The thickness of the epithelium layer is well visible even in routine stains, such as hematoxylin and eosin (HE) (Figure 15.5a) (Truong et al., 2005).

Arterial banding using textile bands can damage the nervi vasorum within the tunica adventitia of an artery. For detection of nerve fibers it is possible to use antibody antineurofilament protein (Figure 15.6d) (Nedorost et al., 2013).

15.7 **TESTING AND ASSESSMENT OF DEGRADATION**

Scaffolds from biodegradable polymers usually change their physical and chemical properties substantially after *in vivo* implantation. During evaluation of these changes we must pay attention to healing time and phases of degradation. In the first phase, we find changes of polymer surface, such as an increase in surface

◀ adventitia of pulmonary artery of a pig (brown area, red arrow), scale bar 100 μm. (e) Immunohistochemical detection of endothelial cells (EC) (red arrow) in newly formed vessels, anti-von Willebrand factor antibody, scale bar 100 μm. (f) Detection of EC (red arrow) in newly formed vessels, anti-CD31, scale bar 50 μm. Visualization was done using horseradish peroxidase/diaminobenzidine in all slides, counterstaining was done with Gill's hematoxylin in all slides.

roughness. Decomposition of molecular chains comes up during the next phase. This leads to a decrease in the polymer Mw and diffusion of large-molecular-weight fragments into the surrounding tissue. This results in a decrease in the tensile strength. In the last stage, the polymer matrix collapses and decreases its mean Mw. Mechanical properties decline due to disappearing crystallinity (Azevedo and Reis, 2005). The mechanism of degradation for different polymers depends on their Mw, morphology of each type of polymer, and environmental factors such as osmotic pressure, pH, temperature, etc. Degradation occurs mainly by hydrolysis, oxidation, or enzymatic reactions (Marin et al., 2013). The efficiency of polymeric material is affected by its stability (Uhrich et al., 1999). Therefore, understanding the mechanisms of degradation of a specific polymer is crucial to determine its suitable applications, but also limitations of its use.

Characteristics evaluating the polymer degradation are as follows: weight loss, crystallinity, molecular weight, morphology and dimensional changes, surface chemistry, isolation, and identification of degradation products and mechanical properties.

15.7.1 WEIGHT LOSS

Comparing the mass before implantation and after the degradation period we get information about changes of polymer weight. The initial weight of the sample is measured after drying of material to a constant mass. The degree of degradation is calculated as a percentage of weight loss (Azevedo and Reis, 2005), using the formula:

$$\% \text{ Mass loss} = \frac{M_i - M_f}{M_i} \times 100$$

where M_f is the final mass and M_i is the initial mass (Lam et al., 2009).

15.7.2 MOLECULAR WEIGHT

The quantification of the polymer molecular weight (Mw) during the degradation is important for analyzing the degradation mechanisms of biomaterials. Mw influences many other properties, for example crystallinity, weight loss, mechanical properties, and morphology (Azevedo and Reis, 2005).

15.7.3 CRYSTALLINITY

The crystallinity of polymer affects its mechanical strength, opacity, and thermal properties. The changes in the crystallinity of polymer after degradation can be measured by using differential scanning calorimetry (Azevedo and Reis, 2005).

15.7.4 MORPHOLOGY AND DIMENSIONAL CHANGES OF BIOMATERIAL

Changes on the polymer surface are usually observed using light microscopy, scanning electron microscopy, and atomic force microscopy (Matheson et al., 2002). Scaffold porosity is measured as a ratio of the true volume to the apparent volume. The true volume or actual volume of material that makes up the scaffold was determined using a gas pycnometer. The apparent volume denotes the overall geometrical volume occupied by the whole sample. The porosity of the scaffolds (expressed as a percentage value) may be calculated according to the formula:

$$\% \text{ Porosity} = \frac{V_a - V_t}{V_a} \times 100$$

where V_a is the apparent volume and V_t the true volume (Lam et al., 2009).

15.7.5 ISOLATION AND IDENTIFICATION OF PRODUCTS OF DEGRADATION

The safety of a biomaterial and its degradation products is essential for its use in medicine. Products of degradation of polymers can leach into surrounding tissues and may enter the circulation. Some of the products may be easily metabolized and can cause toxic effects (Griffiths et al., 1996). Therefore it is important to identify the products released at different stages of degradation, their lifespan and the kinetics of their formation. For qualitative and quantitative analysis of the degradation products within the tissue fluid, synovial fluid, or other body fluids, the following methods may be used: high-performance liquid chromatography, nuclear magnetic resonance, and mass spectroscopy (Azevedo and Reis, 2005).

15.7.6 MECHANICAL TESTING OF DEGRADATION OF BIOMATERIALS

As mentioned in Section 15.4.2.1, the mechanical properties of individual biomaterials can differ between a pure form and a composite, and the mechanical properties can change after implantation in the body. The inert biomaterials are less influenced. In contrast, the biological materials such as collagen could be influenced by the surrounding environment. Moreover, it is very important to observe the *in vivo* behavior of the biomaterial implants, healing of the tissue, and degradation of biomaterials implanted into body.

The classical mechanical tests cannot be directly used in the *in vivo* environment to determine the healing of the tissue, changes in mechanical properties after implantation, or to assess and observe the degradation process. One possibility is the frequently used animal model, where the tissue is removed from the body after a given time necessary for healing after implantation operation or after another specific time. In this case the cells, tissue matrix, and biomaterials are destroyed because this is a one-way journey of monitoring mechanical properties.

The second possibility is the *in vitro* test done on biomaterials themselves or biomaterials planted with stem cells, currently very popular in tissue engineering scaffolds. The classical tests (Section 16.5.2) can then be applied to determine the mechanical parameters. In both cases the *in vitro* environment corresponds as much as possible to the body environment. It includes the physiological liquid buffer, pH, light, temperature, oxygen, and nutrition support, etc.

Noninvasive *in vivo* measurements can be done by the *elasticity imaging methods*. They combine the tissue excitation techniques with methods for detection of tissue response. They can be static or dynamic. In static methods, the tissue is compressed slowly and the distribution of its displacement is measured with magnetic resonance, ultrasound, or optically. The dynamic methods rely on the wave equation, which in its differential form is local in character. Therefore, the distribution of dynamic displacement, a three-dimensional vector, and its second-order partial derivatives in time and space within a small region of the tissue is enough to completely characterize the shear moduli of the tissue in that region. The excitation could be done by direct application of a compression force (stress) on the skin to deform the tissue at the bottom. This is often done by simply pressing and holding a plate on the skin (in static approach) or vibrating the skin using a vibratory device (in dynamic approach). The tissue could also be excited internally and directly in the region of interest within tissue, that is, using the radiation force of an ultrasound beam. By this method we can reach a concentrated stress (or a point-like force) to probe the tissue point-by-point, directly and remotely within the region of interest.

15.7.6.1 *Ultrasound elastography (elasticity imaging)*

The ultrasound elasticity imaging is popular in noninvasive monitoring of cell growth, scaffold degradation, and tissue development technique (Carlsen et al., 2013; Gennisson et al., 2013; Ophir et al., 2002; Svensson and Amiras, 2006). It enables continuous monitoring of the *in vivo* regeneration of tissue, progressive biomaterial degradation, and progression of various diseases. The method is based on phase-sensitive speckle displacement.

When a tissue is mechanically excited by a weak quasistatic compression, the internal stresses are defined by the boundary conditions as well as by the structure and properties of the tissue. The local elastic properties of material under compression should be measured in three orthogonal spatial orientations relative to the ultrasonic beam.

When using ultrasound elasticity imaging it is important to use a small compression strain (less than 2%, typically 1%) to minimize the distortion of the signal due to compression. The tissue is insonified before loading and after loading. The strain is estimated from displacement from the time shift measurement by assuming a constant speed of sound. The local longitudinal strain in combination with the local longitudinal stress in the tissue generates quantitative images (elastograms) of local estimation of the elastic modulus. Original elastograms are

gray-scaled, where black represents hard tissue, white represents soft tissue, and grays represent intermediate elasticity.

The ultrasound elasticity imaging requires a mechanical compression, which limits its application to areas where clear physical access can be achieved. The measured strain has to be normalized to overall strain applied to the body and this is the source of error.

An alternative to ultrasound elasticity is transient elastography (TE). In this method, a single transient shear wave is induced into tissue via a special transducer and the propagation of this wave is imaged using ultrasound. The propagation speed of the shear wave is related to the underlying tissue shear modulus. The results are used to calculate the absolute elastic modulus of the tissue. The TE can be combined with an optical method. For example, the photoaccoustic imaging combines optical excitation and ultrasound detection (Park et al., 2014) to also obtain the visualization of scaffold degradation.

### 15.7.6.2 Magnetic resonance elastography

Magnetic resonance elastography is a dynamic elasticity imaging-based noninvasive technique that is currently used to monitor *in vivo* regeneration of tissue, subsequent biomaterial degradation, and the progression of various diseases (Mariappan et al., 2010; Smith et al., 1997). It combines benefits of the acoustic shear waves and MRI. MRI has a high image resolution and is used to measure the displacement caused by shear waves. The measurable scale of displacement is 100 nm and greater.

The harmonic shear waves (vibrations) of acoustic-range frequencies (50−500 Hz) are induced using an external driver. The propagation of these vibrations in the tissue is captured using the MRI technique. The shear modulus of material (μ) is calculated using assumptions on tissue properties: to be linearly elastic, isotropic, and Hookean. Also, the quantitative images displaying the stiffness of material (tissue) can be generated.

15.7.6.3 Optical elastography

Optical coherence elastography (OCE) is a novel elastography technology used to determine tissue biomechanical properties *in vivo* using optical coherence tomography (Kennedy et al., 2014; Liang et al., 2010; Rogowska et al., 2004; Sun et al., 2011). The OCE is used for measuring and imaging biomechanical properties at the micron-scale tissue level, the cellular level, and even the molecular level. The tissue excitation can be static or dynamic (waves, pulse) and applied to the tissue either internally or externally: external compressive load, surface acoustic waves, shear waves, acoustic radiation force, magnetomotive, and swept-frequency loading. The tissue displacement and the resulting data are processed by a special algorithm to obtain the elastogram image reconstruction.

Tissue Doppler optical coherence elastography is another optical method to image tissue movements, strain rates, and strains of soft tissue *in vivo* in real time (Wang, 2006). The reaction on tissue excitation is measured with using Doppler
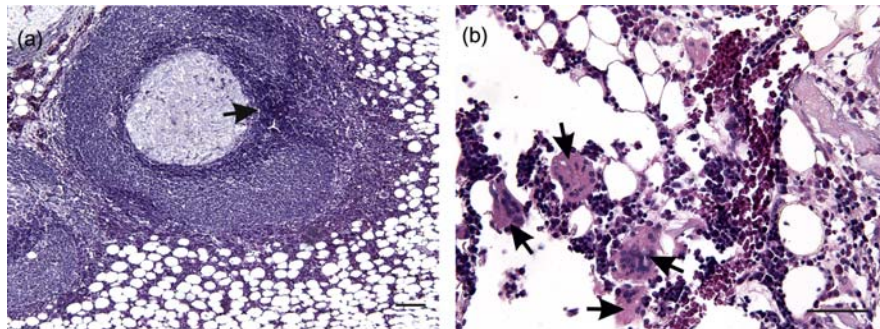
FIGURE 15.7

Microphotographs of tissue reaction to the presence of foreign materials (foreign bodies). (a) Recruitment of granulocytes within bone marrow as a reaction on implantation of calcium phosphate osteoinductive granules; hematoxylin—eosin (HE) stain, scale bar 100 μm. (b) Multinucleated giant cells from foreign bodies formed by fusion of a number of macrophages within the bone marrow close to a healing bone defect supported with a degradable tissue scaffold, HE stain, scale bar 50 μm.

effect in optical coherence interferograms induced by a tissue motion. The phase changes are measured between individual scans to resolve the instantaneous tissue displacement.

15.7.7 REACTION TO FOREIGN BODIES

Tissue reactions to the presence of foreign bodies comprise invasion of granulocytes (Figure 15.7a), recruitment of macrophages, and formation of multinucleated giant cells from foreign bodies (Figure 15.7b), which originated fusion of macrophages. A connective capsule may be formed around biomaterials as a result of synthesis of tissue matrix by fibroblasts. These findings may be evaluated after *in vivo* implantation of biomaterials using histological processing.

15.8 CONCLUSIONS

Histological methods are an irreplaceable part of the *in vivo* evaluation of the effect of biomaterials implanted into damage tissue. Application of quantitative histology provides us with information on distribution and spatial relationships among the scaffold, cells, ECM, and the process of angiogenesis and inflammation. Measuring of the biomechanical properties of biomaterials provides important results supplementary to those from morphological analysis. We use animal models for *in vivo* evaluation of biomaterials. Continuous morphometric variables are preferably used for microscopic quantification of tissue healing, so that biological hypotheses of the experiments in animal models may be tested using standard statistical tests.

ACKNOWLEDGMENTS

REFERENCES

Adamson, R., 2009. Role of macrophages in normal wound healing: an overview. J. Wound Care 18, 349−351.

Ananta, M., Brown, R.A., Mudera, V., 2012. A rapid fabricated living dermal equivalent for skin tissue engineering: an in vivo evaluation in an acute wound model. Tissue Eng. A 18, 353−361.

Anderson, J.M., 2001. Biological responses to materials. Annu. Rev. Mater. Res. 31, 81−110.

Andrade, T.A.M., Iyer, A., Das, P.K., Foss, N.T., Garcia, S.B., Coutinho-Netto, J., et al., 2011. The inflammatory stimulus of a natural latex biomembrane improves healing in mice. Braz. J. Med. Biol. Res. Rev. Bras. Pesqui. Médicas E Biológicas Soc. Bras. Biofísica Al 44, 1036−1047.

Atala, A., Bauer, S.B., Soker, S., Yoo, J.J., Retik, A.B., 2006. Tissue-engineered autologous bladders for patients needing cystoplasty. Lancet 367, 1241−1246.

Azevedo, H., Reis, R., 2005. Understanding the enzymatic degradation of biodegradable polymers and strategies to control their degradation rate. In: Reis, R.L., Román, J.S. (Eds.), Biodegradable Systems in Tissue Engineering and Regenerative Medicine. CRC Press, Boca Raton, FL, pp. 177−202.

Bauer, E.A., Cooper, T.W., Huang, J.S., Altman, J., Deuel, T.F., 1985. Stimulation of in vitro human skin collagenase expression by platelet-derived growth factor. Proc. Natl. Acad. Sci. U.S.A. 82, 4132−4136.

Blatti, S.P., Foster, D.N., Ranganathan, G., Moses, H.L., Getz, M.J., 1988. Induction of fibronectin gene transcription and mRNA is a primary response to growth-factor stimulation of AKR-2B cells. Proc. Natl. Acad. Sci. U.S.A. 85, 1119−1123.

Brandtzaeg, P., Dale, I., Gabrielsen, T.O., 1992. The leucocyte protein L1 (calprotectin): usefulness as an immunohistochemical marker antigen and putative biological function. Histopathology 21, 191−196.

Breinan, H.A., Minas, T., Hsu, H.P., Nehrer, S., Shortkroff, S., Spector, M., 2001. Autologous chondrocyte implantation in a canine model: change in composition of reparative tissue with time. J. Orthop. Res. Off. Publ. Orthop. Res. Soc 19, 482−492. Available from: http://dx.doi.org/10.1016/S0736-0266(00)90015-9.

Burdick, J.A., Mauck, R.L., 2011. Biomaterials for Tissue Engineering Applications: A Review of the Past and Future Trends. Springer, Wien.

Butt, R.P., Laurent, G.J., Bishop, J.E., 1995. Collagen production and replication by cardiac fibroblasts is enhanced in response to diverse classes of growth factors. Eur. J. Cell Biol. 68, 330−335.

Carlsen, J., Ewertsen, C., Lönn, L., Nielsen, M., 2013. Strain elastography ultrasound: an overview with emphasis on breast cancer diagnosis. Diagnostics 3, 117−125.

Christopherson, G.T., Song, H., Mao, H.-Q., 2009. The influence of fiber diameter of electrospun substrates on neural stem cell differentiation and proliferation. Biomaterials 30, 556−564. Available from: http://dx.doi.org/10.1016/j.biomaterials.2008.10.004.

Cui, W., Wang, Q., Chen, G., Zhou, S., Chang, Q., Zuo, Q., et al., 2011. Repair of articular cartilage defects with tissue-engineered osteochondral composites in pigs. J. Biosci. Bioeng. 111, 493−500. Available from: http://dx.doi.org/10.1016/j.jbiosc.2010.11.023.

Darby, I.A., Hewitson, T.D., 2007. Fibroblast differentiation in wound healing and fibrosis. In: Jeon, K.W. (Ed.), International Review of Cytology. Academic Press, University of Tennesse, Knoxville, TN, USA, pp. 143−179.

Dekker, A., Beugeling, T., Wind, H., Poot, A., Bantjes, A., Feijen, J., et al., 1991. Deposition of cellular fibronectin and desorption of human serum albumin during adhesion and spreading of human endothelial cells on polymers. J. Mater. Sci. Mater. Med. 2, 227−233.

Dettmeyer, R.B., 2011. Forensic Histopathology: Fundamentals and Pespectives. Springer-Verlag, Berlin.

Deuel, T.F., Senior, R.M., Huang, J.S., Griffin, G.L., 1982. Chemotaxis of monocytes and neutrophils to platelet-derived growth factor. J. Clin. Invest. 69, 1046−1049.

Engler, A.J., Griffin, M.A., Sen, S., Bönnemann, C.G., Sweeney, H.L., Discher, D.E., 2004. Myotubes differentiate optimally on substrates with tissue-like stiffness: pathological implications for soft or stiff microenvironments. J. Cell Biol. 166, 877−887.

Epstein, S.E., Kornowski, R., Fuchs, S., Dvorak, H.F., 2001. Angiogenesis therapy: amidst the hype, the neglected potential for serious side effects. Circulation 104, 115−119.

Evans, B.J., Haskard, D.O., Sempowksi, G., Landis, R.C., 2013. Evolution of the macrophage CD163 phenotype and cytokine profiles in a human model of resolving inflammation. Int. J. Inflamm. 2013, 780502.

Fan, H., Tao, H., Wu, Y., Hu, Y., Yan, Y., Luo, Z., 2010. TGF-β3 immobilized PLGA-gelatin/chondroitin sulfate/hyaluronic acid hybrid scaffold for cartilage regeneration. J. Biomed. Mater. Res. A 95, 982−992. Available from: http://dx.doi.org/10.1002/jbm.a.32899.

Ferguson, M.W.J., O'Kane, S., 2004. Scar-free healing: from embryonic mechanisms to adult therapeutic intervention. Philos. Trans. R. Soc. Lond. B. Biol. Sci. 359, 839−850. Available from: http://dx.doi.org/10.1098/rstb.2004.1475.

Filová, E., Jelínek, F., Handl, M., Lytvynets, A., Rampichová, M., Varga, F., et al., 2008. Novel composite hyaluronan/type I collagen/fibrin scaffold enhances repair of osteochondral defect in rabbit knee. J. Biomed. Mater. Res. B. Appl. Biomater. 87, 415−424. Available from: http://dx.doi.org/10.1002/jbm.b.31119.

Filová, E., Rampichová, M., Handl, M., Lytvynets, A., Halouzka, R., Usvald, D., et al., 2007. Composite hyaluronate-type I collagen-fibrin scaffold in the therapy of osteochondral defects in miniature pigs. Physiol. Res. Acad. Sci. Bohemoslov. 56 (Suppl. 1), S5−S16.

Filová, E., Rampichová, M., Litvinec, A., Držík, M., Míčková, A., Buzgo, M., et al., 2013. A cell-free nanofiber composite scaffold regenerated osteochondral defects in miniature pigs. Int. J. Pharm. 447, 139−149. Available from: http://dx.doi.org/10.1016/j.ijpharm.2013.02.056.

Folkman, J., Klagsbrun, M., 1987. Angiogenic factors. Science 235, 442−447.

Fung, Y.C., 1993. Biomechanics: Mechanical Properties of Living Tissues, second ed. Springer-Verlag, New York, NY.

Gennisson, J.-L., Deffieux, T., Fink, M., Tanter, M., 2013. Ultrasound elastography: principles and techniques. Diagn. Interv. Imaging 94, 487−495.

Gilbert, T.W., Sellaro, T.L., Badylak, S.F., 2006. Decellularization of tissues and organs. Biomaterials 27, 3675−3683.

Griffiths, M.M., Langone, J.J., Lightfoote, M.M., 1996. Biomaterials and granulomas. Methods San Diego Calif. 9, 295−304.

Grotendorst, G.R., Chang, T., Seppä, H.E., Kleinman, H.K., Martin, G.R., 1982. Platelet-derived growth factor is a chemoattractant for vascular smooth muscle cells. J. Cell Physiol. 113, 261−266. Available from: http://dx.doi.org/10.1002/jcp.1041130213.

Grover, C.N., Cameron, R.E., Best, S.M., 2012. Investigating the morphological, mechanical and degradation properties of scaffolds comprising collagen, gelatin and elastin for use in soft tissue engineering. J. Mech. Behav. Biomed. Mater. 10, 62−74.

Hejcl, A., Lesný, P., Prádný, M., Sedý, J., Zámecník, J., Jendelová, P., et al., 2009. Macroporous hydrogels based on 2-hydroxyethyl methacrylate. Part 6: 3D hydrogels with positive and negative surface charges and polyelectrolyte complexes in spinal cord injury repair. J. Mater. Sci. Mater. Med. 20, 1571−1577.

Helpap, B., 1987. Leitfaden der Allgemeinen Entzündungslehre. Springer, Berlin.

Hench, L.L., Jones, J.R., 2005. Biomaterials, Artificial Organs and Tissue Engineering. Woodhead Publishing in Materials. CRC Press, Boca Raton, FL.

Hrebikova, H., Diaz, D., Mokry, J., 2013. Chemical decellularization: a promising approach for preparation of extracellular matrix. Biomed. Pap. 157, 12−17.

Ifkovits, J.L., Burdick, J.A., 2007. Review: photopolymerizable and degradable biomaterials for tissue engineering applications. Tissue Eng. 13, 2369−2385.

Igarashi, T., Iwasaki, N., Kawamura, D., Kasahara, Y., Tsukuda, Y., Ohzawa, N., et al., 2012. Repair of articular cartilage defects with a novel injectable in situ forming material in a canine model. J. Biomed. Mater. Res. A 100, 180−187. Available from: http://dx.doi.org/10.1002/jbm.a.33248.

Jaffe, M., Hammond, W., Tolias, P., Arinzeh, T., 2013. Characterization of Biomaterials. Woodhead Publishing, Oxford.

Jain, R.K., 2003. Molecular regulation of vessel maturation. Nat. Med. 9, 685−693.

Junge, K., Klinge, U., Rosch, R., Mertens, P.R., Kirch, J., Klosterhalfen, B., et al., 2004. Decreased collagen type I/III ratio in patients with recurring hernia after implantation of alloplastic prostheses. Langenbecks Arch. Surg. Dtsch. Ges. Für Chir. 389, 17−22.

Keck, P.J., Hauser, S.D., Krivi, G., Sanzo, K., Warren, T., Feder, J., et al., 1989. Vascular permeability factor, an endothelial cell mitogen related to PDGF. Science 246, 1309−1312.

Kennedy, B.F., McLaughlin, R.A., Kennedy, K.M., Chin, L., Curatolo, A., Tien, A., et al., 2014. Optical coherence micro-elastography: mechanical-contrast imaging of tissue microstructure. Biomed. Opt. Express 5, 2113−2124.

Kocová, J., 1970. Overall staining of connective tissue and the muscular layer of vessels. Folia Morphol. 18, 293−295.

Kondo, T., 2007. Timing of skin wounds. Leg. Med. Tokyo Jpn. 9, 109−114.

Kong, H.J., Kaigler, D., Kim, K., Mooney, D.J., 2004. Controlling rigidity and degradation of alginate hydrogels via molecular weight distribution. Biomacromolecules 5, 1720−1727.

Krasnov, M.S., Rybakova, E.Y., Tikhonov, V.E., Stretskii, G.M., Avdeenko, O.E., Shaikhaliev, A.I., et al., 2012. Burn-healing effects of a composition containing chitosan gel and a blood serum bioregulator. Bull. Exp. Biol. Med. 153, 550−553.

Laato, M., Kahari, V.M., Niinikoski, J., Vuorio, E., 1987. Epidermal growth factor increases collagen production in granulation tissue by stimulation of fibroblast proliferation and not by activation of procollagen genes. Biochem. J. 247, 385−388.

Lam, C.X.F., Hutmacher, D.W., Schantz, J.-T., Woodruff, M.A., Teoh, S.H., 2009. Evaluation of polycaprolactone scaffold degradation for 6 months *in vitro* and *in vivo*. J. Biomed. Mater. Res. A 90, 906−919.

Lambertz, A., Vogels, R.R.M., Busch, D., Schuster, P., Jockenhövel, S., Neumann, U.P., et al., 2015. Laparotomy closure using an elastic suture: a promising approach: laparotomy closure using an elastic suture. J. Biomed. Mater. Res. B. Appl. Biomater. 103, 417−423. Available from: http://dx.doi.org/10.1002/jbm.b.33222.

Langer, R., Vacanti, J.P., 1993. Tissue engineering. Science 260, 920−926.

Leibovich, S.J., Wiseman, D.M., 1988. Macrophages, wound repair and angiogenesis. Prog. Clin. Biol. Res. 266, 131−145.

Lewandowska, K., Pergament, E., Sukenik, C.N., Culp, L.A., 1992. Cell-type-specific adhesion mechanisms mediated by fibronectin adsorbed to chemically derivatized substrata. J. Biomed. Mater. Res. 26, 1343−1363. Available from: http://dx.doi.org/10.1002/jbm.820261007.

Li, J., Zhang, Y.-P., Kirsner, R.S., 2003. Angiogenesis in wound repair: angiogenic growth factors and the extracellular matrix. Microsc. Res. Tech. 60, 107−114.

Liang, X., Crecea, V., Boppart, S.A., 2010. Dynamic optical coherence elastography: a review. J. Innov. Opt. Health Sci. 3, 221−233.

Litvik, R., Vantuchová, Y., 2011. Hypertrofické a keloidní jizvy pohledem dermatologa. New EU Mag. Med. 2011, 15−17.

Mačák, J., Mačáková, J., 2004. Patologie. Grada, Praha.

Mariappan, Y.K., Glaser, K.J., Ehman, R.L., 2010. Magnetic resonance elastography: a review. Clin. Anat. 23, 497−511.

Marin, M.L., Veith, F.J., Cynamon, J., Sanchez, L.A., Bakal, C.W., Suggs, W.D., et al., 1995. Human transluminally placed endovascular stented grafts: preliminary histopathologic analysis of healing grafts in aortoiliac and femoral artery occlusive disease. J. Vasc. Surg. 21, 595−603, discussion 603−604.

Marin, E., Briceño, M.I., Caballero-George, C., 2013. Critical evaluation of biodegradable polymers used in nanodrugs. Int. J. Nanomed. 8, 3071−3090.

Masopust, J., Průša, R., 2003. Patobiochemie Buňky. ČSKB, 2.LF UK, Praha.

Matheson, L.A., Labow, R.S., Santerre, J.P., 2002. Biodegradation of polycarbonate-based polyurethanes by the human monocytes-derived macrophage and U937 cell systems. J. Biomed. Mater. Res. 61, 505−513.

Meruane, M.A., Rojas, M., Marcelain, K., 2012. The use of adipose tissue-derived stem cells within a dermal substitute improves skin regeneration by increasing neoangiogenesis and collagen synthesis. Plast. Reconstr. Surg. 130, 53−63.

Mignatti, P., Rifkin, D.B., 1996. Plasminogen activators and matrix metalloproteinases in angiogenesis. Enzyme Protein 49, 117−137.

Monteiro, G.A., Delossantos, A.I., Rodriguez, N.L., Patel, P., Franz, M.G., Wagner, C.T., 2013. Porcine incisional hernia model: evaluation of biologically derived intact extra-cellular matrix repairs. J. Tissue Eng, 4. Available from: http://dx.doi.org/10.1177/2041731413508771.

Montesano, R., Vassalli, J.D., Baird, A., Guillemin, R., Orci, L., 1986. Basic fibroblast growth factor induces angiogenesis in vitro. Proc. Natl. Acad. Sci. U.S.A. 83, 7297−7301.

Moon, J.J., West, J.L., 2008. Vascularization of engineered tissues: approaches to promote angio-genesis in biomaterials. Curr. Top. Med. Chem. 8, 300−310.

Mouton, P.R., 2002. Principles and Practices of Unbiased Stereology: An Introduction for Bioscientists. Johns Hopkins University Press, Baltimore, MD.

Mutsaers, S.E., McAnulty, R.J., Laurent, G.J., Versnel, M.A., Whitaker, D., Papadimitriou, J.M., 1997. Cytokine regulation of mesothelial cell proliferation in vitro and in vivo. Eur. J. Cell Biol. 72, 24−29.

Nedorost, L., Uemura, H., Furck, A., Saeed, I., Slavik, Z., Kobr, J., et al., 2013. Vascular histopathologic reaction to pulmonary artery banding in an *in vivo* growing porcine model. Pediatr. Cardiol. 34, 1652−1660.

Nowak, D., Popow-Woźniak, A., Raźnikiewicz, L., Malicka-Błaszkiewicz, M., 2009. Actin in the wound healing process. Postepy Biochem. 55, 138−144.

Nwe, N., Furuike, T., Tamura, H., 2009. The mechanical and biological properties of chito-san scaffolds for tissue regeneration templates are significantly enhanced by chitosan from gongronella butleri. Materials 2, 374−398.

Obara, K., Ishihara, M., Ishizuka, T., Fujita, M., Ozeki, Y., Maehara, T., et al., 2003. Photocrosslinkable chitosan hydrogel containing fibroblast growth factor-2 stimulates wound healing in healing-impaired db/db mice. Biomaterials 24, 3437−3444.

Oberpenning, F., Meng, J., Yoo, J.J., Atala, A., 1999. De novo reconstitution of a functional mammalian urinary bladder by tissue engineering. Nat. Biotechnol. 17, 149−155.

Ophir, J., Alam, S.K., Garra, B.S., Kallel, F., Konofagou, E.E., Krouskop, T., et al., 2002. Elastography: imaging the elastic properties of soft tissues with ultrasound. J. Med. Ultrason. 29, 155−171.

Ortiz-Masià, D., Díez, I., Calatayud, S., Hernández, C., Cosín-Roger, J., Hinojosa, J., et al., 2012. Induction of CD36 and thrombospondin-1 in macrophages by hypoxia-inducible factor 1 and its relevance in the inflammatory process. PLoS One 7, e48535.

Pakyari, M., Farrokhi, A., Maharlooei, M.K., Ghahary, A., 2013. Critical role of transform-ing growth factor beta in different phases of wound healing. Adv. Wound Care 2, 215−224. Available from: http://dx.doi.org/10.1089/wound.2012.0406.

Palsson, B., Bhatia, S., 2004. Tissue Engineering. Pearson Prentice Hall, Upper Saddle River, NJ.

Parida, P., 2012. Classification of biomaterials used in medicine. Int. J. Adv. Appl. Sci. IJAAS 3, 125−129.

Park, S., Lee, C., Kim, J., Kim, C., 2014. Acoustic resolution photoacoustic microscopy. Biomed. Eng. Lett. 4, 213−222.

Patel, N.R., Gohil, P.P., 2012. A review on biomaterials: scope, applications & human anatomy significance. Int. J. Emerg. Technol. Adv. Eng. 2 (4), 91−101.

Patel, Z.S., Mikos, A.G., 2004. Angiogenesis with biomaterial-based drug- and cell-delivery systems. J. Biomater. Sci. Polym. Ed. 15, 701−726.

Pepper, M.S., 2001. Role of the matrix metalloproteinase and plasminogen activator-plasmin systems in angiogenesis. Arterioscler. Thromb. Vasc. Biol. 21, 1104−1117.

Plencner, M., East, B., Tonar, Z., Otáhal, M., Prosecká, E., Rampichová, M., et al., 2014. Abdominal closure reinforcement by using polypropylene mesh functionalized with poly-ε-caprolactone nanofibers and growth factors for prevention of incisional hernia formation. Int. J. Nanomed. 9, 3263−3277.

Pruitt, L.A., Chakravartula, A.M., 2011. Mechanics of Biomaterials Fundamental Principles for Implant Design. Cambridge University Press, Cambridge, MA.

Rampichová, M., Filová, E., Varga, F., Lytvynets, A., Prosecká, E., Koláčná, L., et al., 2010. Fibrin/hyaluronic acid composite hydrogels as appropriate scaffolds for *in vivo* artificial cartilage implantation. ASAIO J. 56, 563−568.

Ratner, B.D., 2012. Biomaterials Science: An Introduction to Materials in Medicine, second ed. Academic Press, New York, NY.

Reinke, J.M., Sorg, H., 2012. Wound repair and regeneration. Eur. Surg. Res. 49, 35−43.

Rheinwald, J.G., Green, H., 1977. Epidermal growth factor and the multiplication of cultured human epidermal keratinocytes. Nature 265, 421−424.

Risau, W., 1997. Mechanisms of angiogenesis. Nature 386, 671−674.

Ristow, H.J., Messmer, T.O., 1988. Basic fibroblast growth factor and insulin-like growth factor I are strong mitogens for cultured mouse keratinocytes. J. Cell Physiol. 137, 277−284. Available from: http://dx.doi.org/10.1002/jcp.1041370210.

Rockman, H.A., Ono, S., Ross, R.S., Jones, L.R., Karimi, M., Bhargava, V., et al., 1994. Molecular and physiological alterations in murine ventricular dysfunction. Proc. Natl. Acad. Sci. U. S. A. 91, 2694−2698.

Rogowska, J., Patel, N.A., Fujimoto, J.G., Brezinski, M.E., 2004. Optical coherence tomographic elastography technique for measuring deformation and strain of atherosclerotic tissues. Heart Br. Card. Soc. 90, 556−562.

Ross, R., Raines, E.W., Bowen-Pope, D.F., 1986. The biology of platelet-derived growth factor. Cell 46, 155−169.

Sakiyama-Elbert, S.E., Hubbell, J.A., 2000. Development of fibrin derivatives for controlled release of heparin-binding growth factors. J. Control. Release Off. J. Control. Release Soc. 65, 389−402.

Schreiber, A.B., Winkler, M.E., Derynck, R., 1986. Transforming growth factor-alpha: a more potent angiogenic mediator than epidermal growth factor. Science 232, 1250−1253.

Screen, H.R.C., 2008. Investigating load relaxation mechanics in tendon. J. Mech. Behav. Biomed. Mater. 1, 51−58.

Seal, B., 2001. Polymeric biomaterials for tissue and organ regeneration. Mater. Sci. Eng. R Rep. 34, 147−230.

Seo, S.-H., Sung, H.-W., 2012. Treatment of keloids and hypertrophic scars using topical and intralesional mitomycin C. J. Eur. Acad. Dermatol. Venereol. JEADV 26, 634−638.

Seppä, H., Grotendorst, G., Seppä, S., Schiffmann, E., Martin, G.R., 1982. Platelet-derived growth factor in chemotactic for fibroblasts. J. Cell Biol. 92, 584−588.

Sjölund, M., Hedin, U., Sejersen, T., Heldin, C.H., Thyberg, J., 1988. Arterial smooth muscle cells express platelet-derived growth factor (PDGF) A chain mRNA, secrete a

PDGF-like mitogen, and bind exogenous PDGF in a phenotype- and growth state-dependent manner. J. Cell Biol. 106, 403−413.

Smith, J.A., Muthupillai, R., Rossman, P.J., Hulshizer, T.C., Greenleaf, J.F., Ehman, R.L., 1997. Characterization of biomaterials using magnetic resonance elastography. In: Thompson, D.O., Chimenti, D.E. (Eds.), Review of Progress in Quantitative Nondestructive Evaluation, Review of Progress in Quantitative Nondestructive Evaluation. Springer, Springer Science, New York, US, pp. 1323−1330.

Song, Z., Peng, Z., Liu, Z., Yang, J., Tang, R., Gu, Y., 2013. Reconstruction of abdominal wall musculofascial defects with small intestinal submucosa scaffolds seeded with tenocytes in rats. Tissue Eng. A 19, 1543−1553. Available from: http://dx.doi.org/10.1089/ten.tea.2011.0748.

Steed, D.L., 2006. Clinical evaluation of recombinant human platelet-derived growth factor for the treatment of lower extremity ulcers. Plast. Reconstr. Surg. 117, 143S−151S.

Sun, J., Tan, H., 2013. Alginate-based biomaterials for regenerative medicine applications. Materials 6, 1285−1309.

Sun, C., Standish, B., Yang, V.X.D., 2011. Optical coherence elastography: current status and future applications. J. Biomed. Opt. 16, 043001−043001−12.

Suri, C., Jones, P.F., Patan, S., Bartunkova, S., Maisonpierre, P.C., Davis, S., et al., 1996. Requisite role of angiopoietin-1, a ligand for the TIE2 receptor, during embryonic angiogenesis. Cell 87, 1171−1180.

Svensson, W.E., Amiras, D., 2006. Ultrasound elasticity imaging. Breast Cancer Online 9, 1−7.

Tabata, Y., Ikada, Y., 1999. Vascularization effect of basic fibroblast growth factor released from gelatin hydrogels with different biodegradabilities. Biomaterials 20, 2169−2175.

Teoh, S.H., 2000. Fatigue of biomaterials: a review. Int. J. Fatigue 22, 825−837.

Tichý, M., Tichá, V., Sčudla, V., Šváchová, M., Zapletalová, J., 2010. Analýza angiogeneze v kostní dřeni u plazmocytárního myelomu. Čes.-Slov. Patol. 2010, 15−19.

Truong, A.-T.N., Kowal-Vern, A., Latenser, B.A., Wiley, D.E., Walter, R.J., 2005. Comparison of dermal substitutes in wound healing utilizing a nude mouse model. J. Burns Wounds 4, e4.

Tzeng, D.Y., Deuel, T.F., Huang, J.S., Baehner, R.L., 1985. Platelet-derived growth factor promotes human peripheral monocyte activation. Blood 66, 179−183.

Uhrich, K.E., Cannizzaro, S.M., Langer, R.S., Shakesheff, K.M., 1999. Polymeric systems for controlled drug release. Chem. Rev. 99, 3181−3198.

Ulubayram, K., Nur Cakar, A., Korkusuz, P., Ertan, C., Hasirci, N., 2001. EGF containing gelatin-based wound dressings. Biomaterials 22, 1345−1356.

Uygun, B.E., Soto-Gutierrez, A., Yagi, H., Izamis, M.-L., Guzzardi, M.A., Shulman, C., et al., 2010. Organ reengineering through development of a transplantable recellularized liver graft using decellularized liver matrix. Nat. Med. 16, 814−820. Available from: http://dx.doi.org/10.1038/nm.2170.

Van Beurden, H.E., Von den Hoff, J.W., Torensma, R., Maltha, J.C., Kuijpers-Jagtman, A.M., 2005. Myofibroblasts in palatal wound healing: prospects for the reduction of wound contraction after cleft palate repair. J. Dent. Res. 84, 871−880.

Van Susante, J.L., Buma, P., Schuman, L., Homminga, G.N., van den Berg, W.B., Veth, R.P., 1999. Resurfacing potential of heterologous chondrocytes suspended in fibrin glue in large

full-thickness defects of femoral articular cartilage: an experimental study in the goat. Biomaterials 20, 1167−1175.

Velazquez, O.C., 2007. Angiogenesis & vasculogenesis: inducing the growth of new blood vessels and wound healing by stimulation of bone marrow derived progenitor cell mobilization and homing. J. Vasc. Surg. 45, A39−A47.

Wang, M., 2003. Developing bioactive composite materials for tissue replacement. Biomaterials 24, 2133−2151.

Wang, R.K., 2006. Tissue doppler optical coherence elastography for real time strain rate and strain mapping of soft tissue. Appl. Phys. Lett. 13, 144103−144103-3.

Williams, D.F., 1987. Definitions in Biomaterials. Elsevier Science Ltd., Amsterdam.

Wong, J.Y., Bronzino, J.D., 2007. Biomaterials. CRC Press, Boca Raton, FL.

Yang, E.Y., Moses, H.L., 1990. Transforming growth factor beta 1-induced changes in cell migration, proliferation, and angiogenesis in the chicken chorioallantoic membrane. J. Cell Biol. 111, 731−741.

Yoo, S.Y., Kwon, S.M., 2013. Angiogenesis and its therapeutic opportunities. Mediators Inflamm. 2013, 127170.

Zeltinger, J., Sherwood, J.K., Graham, D.A., Müeller, R., Griffith, L.G., 2001. Effect of pore size and void fraction on cellular adhesion, proliferation, and matrix deposition. Tissue Eng. 7, 557−572.